PREPARATION AND CHARACTERIZATION OF SPUTTERED $SmCo_5$ THIN FILMS FOR MAGNETIC RECORDING MEDIA

LINA ZHANG

NATIONAL UNIVERSITY OF SINGAPORE

2010

PREPARATION AND CHARACTERIZATION OF SPUTTERED $SmCo_5$ THIN FILMS FOR MAGNETIC RECORDING MEDIA

LINA ZHANG
(B.E., BEIJING UNIVERSITY OF ASTRONAUTICS AND AERONAUTICS, CHINA)

A THESIS SUBMITTED
FOR THE DEGREE OF DOCTOR OF PHILOSOPHY

DEPARTMENT OF MATERIALS SCIENCE
NATIONAL UNIVERSITY OF SINGAPORE

2010

Acknowledgements

I would like to thank all the people without whom this thesis would not have been possible.

First of all, I would like to express my sincere thanks to my supervisors Dr. Ding Jun and Dr. Chen Jingsheng for their guidance and encouragements throughout the course of my Ph. D. program. Thanks to Dr. Ding Jun, I learned how to conduct research and gained confidence in my research abilities.

I greatly appreciated the kind help from Mr. Phyoe Wai Lwin and Mr. Cher Kiat Min for operating the sputtering machine and preparing TEM samples as well as the helping hand from Dr. Yi Jiaobao and Dr. Zhang Jixuan for SQUID measurements and TEM imaging, respectively.

I am also grateful to all the people from my department who assisted me during my stay in NUS including all my labmates and all staff.

A special mention for the professors Dr. Li Yi, Dr. Ding Jun, Dr. Adams Stefan and Dr. Chiu Cheng-Hsin from whom I learned core knowledge in materials science.

My final words go to my close friends Omar for proof-reading and Antoine for proof-reading as well as for his consistently reliable support.

Lina Zhang

Summary

The progress in the magnetic storage technology largely depends on the development of magnetic storage media (magnetic films that store information). For ultra-high density recording media, a large anisotropy is necessary in order to scale down the grain size because of the required thermal stability.

$SmCo_5$ is the ultimate candidate because of its uniaxial magnetocrystalline anisotropy (K_u=1.1~2.0×10^8 erg/cm^3) which is the highest among all the hard magnetic materials. $SmCo_5$ based thin films allow significant reduction in the grain size from currently about 7-9 nm in Co-alloys to about 2-3 nm based on the superparamagnetic limitation. Therefore, $SmCo_5$ thin films with fine grains, specific texture and high coercivity are of a high interest for achieving an ultra-high areal density and good recording performances.

This thesis focused on the fabrication of magnetron-sputtering derived $SmCo_5$ thin films for magnetic recording using a layer engineering approach. The study has shown that the structure and the magnetic properties of $SmCo_5$ thin films can be greatly influenced by the texture and the surface morphology of the underlayer and deposition condition. The study has resulted in suitable multilayer designs and deposition control methods in order to obtain $SmCo_5$ films with the desired structure and magnetic properties.

Three layer configurations were studied:

($11\bar{2}0$) textured $SmCo_5$ / (002) textured Cr / glass;

(0001) textured $SmCo_5$ / (111) textured Cu / amorphous-like Ta / glass;

(0001) textured $SmCo_5$ / (211) textured Ni_4W / amorphous-like W / glass.

With the first configuration, a nanocrystalline $SmCo_5$ film was obtained with a high in-plane intrinsic coercivity up to 26.5 kOe and a large in-plane magnetic

anisotropy. The film was deposited on an economical glass substrate at a relatively low temperature of 400 ^{o}C. With the second configuration, a Ta seed layer was found effective in improving the crystallinity, texture and surface morphology of the Cu underlayer. The optimal Ta seed layer was a thin, continuous and amorphous-like layer with a thickness of 4 nm. A highly (000l) textured $SmCo_5$ thin film (with a small $\Delta\theta_{50}$ value of 3.2 ^{o}) exhibiting large perpendicular anisotropy and high out-of-plane intrinsic coercivity around 20 kOe was obtained on the Cu / Ta dual underlayer. The deposition temperature for $SmCo_5$ to having the (0001) texture was as low as 325 ^{o}C. In the last configuration, a nanocrystallined and (211)-textured Ni_4W / W dual underlayer was found to be able to induce $SmCo_5$ thin films with perpendicular anisotropy. This is due to the Ni_4W-(211) plane having a hexagonal structure which is similar to that of the $SmCo_5$-(0001) plane. The Ni_4W underlayer can be as thin as 13 nm. A maximum out-of-plane intrinsic coercivity of 15.5 kOe was achieved in $SmCo_5$ thin films grown on $Ni_{68}W_{32}$ underlayer with Ni_4W clusters. The use of the Ni_4W underlayer has not been reported by other research groups so far. Based on the obtained magnetic properties, $SmCo_5$ / Ni / Ni_4W / W film was found to be a promising hard/soft double-layered design for perpendicular recording applications.

Table of Contents

Acknowledgements……..…….…..……..I

Summary……..……..…….……..……..….II

Table of Contents.....IV

List of Figures VII

List of Tables XIII

List of Publications XIV

1 Chapter I Introduction 1

1.1 Magnetic recording and magnetic recording media.....2

1.1.1 A brief review of magnetic recording.....2

1.1.2 Development of magnetic recording media.....4

1.1.2.1 Longitudinal magnetic recording media.....5

1.1.2.2 Perpendicular magnetic recording media 7

1.1.2.3 Future magnetic recording media.....10

1.1.3 Challenges of magnetic recording media.....11

1.2 Physical properties of $SmCo_5$ 14

1.2.1 Phase diagram and crystal structure of $SmCo_5$.....14

1.2.2 Ferromagnetism, magnetic anisotropy and coercivity mechanism of $SmCo_5$.....15

1.3 Review of studies on $SmCo_5$ thin films.....16

1.4 Motivations and objectives 19

1.5 References.....22

2 Chapter II Experimental techniques.....28

2.1 Sputtering techniques.....29

2.2 Structure and microstructure characterization 32

2.2.1 Rutherford Backscattering Spectroscopy (RBS) 32

2.2.2 X-ray diffraction (XRD).....33

2.2.3 Transmission electron microscopy (TEM) 35

2.2.4 Atomic force microscopy (AFM) 39

2.2.5 Profilometer.....41

2.3 Magnetic properties characterization.....41

2.3.1 Vibrating sample magnetometer (VSM) 41

2.3.2 Superconducting Quantum Interference Device (SQUID) 43
2.3.3 Magnetic characterization 44
2.4 References 50
3 Chapter III $SmCo_5$ thin films with longitudinal anisotropy grown on Cr underlayer 52
3.1 Experimental methods 54
3.2 Growth of Cr underlayer on glass substrate 56
3.2.1 Effect of deposition temperature 56
3.2.2 Effect of thickness 58
3.3 Evaluation of Sm / Co atomic composition 60
3.4 Fabrication of $SmCo_5$ films with Cr underlayer on glass substrate and study of their structure and magnetic properties 62
3.4.1 Effect of deposition temperature of Cr underlayer 62
3.4.2 Effect of thickness of Cr underlayer 66
3.4.3 Effect of thickness of $SmCo_5$ layer 68
3.4.4 Effect of Sm / Co composition 69
3.5 Comparison study of $SmCo_5$ thin film grown on MgO (100) and glass substrates with Cr underlayer 70
3.5.1 Crystallographic structure and microstructure 71
3.5.2 Magnetic properties 75
3.6 Summary 82
3.7 References 83
4 Chapter IV $SmCo_5$ thin films with perpendicular anisotropy grown on Cu underlayers 85
4.1 Experimental methods 88
4.2 Growth of Cu underlayer on Ta seed layer on glass substrate 90
4.2.1 Growth of Ta seed layer 90
4.2.2 Growth of Cu on Ta seed layer 93
4.3 Fabrication of $SmCo_5$ films with Cu / Ta dual underlayer on glass substrate and study of their structure and magnetic properties 97
4.3.1 Effect of thickness of Ta 97
4.3.2 Study of Cu diffusion 100
4.3.3 Effect of deposition temperature of $SmCo_5$ layer 103
4.3.4 Effect of thickness of Cu underlayer 106

4.3.5 Effect of thickness of $SmCo_5$ layer 108
4.3.6 Effect of Sm / Co composition 110
4.4 Fabrication of $SmCo_5$ films with Cu / Ti and Cu / W dual underlayers on glass substrates and study of their structure and magnetic properties 114
4.4.1 Deposition of $SmCo_5$ thin film on Cu / Ti underlayer 114
4.4.2 Deposition of $SmCo_5$ thin film on Cu / W underlayer 116
4.4.3 Magnetic reversal mechanism of $SmCo_5$ thin films 117
4.5 Summary 118
4.6 References 119
5 Chapter V $SmCo_5$ thin films with perpendicular anisotropy grown on Ni-alloy underlayers 121
5.1 Experimental methods 128
5.2 Study of Ni-W alloy underlayers 129
5.2.1 Crystallographic structure 129
5.2.2 Microstructure 132
5.2.3 Magnetic properties 134
5.3 Fabrication of $SmCo_5$ films on Ni-W alloy underlayers and study of their structure and magnetic properties 135
5.3.1 Deposition of $SmCo_5$ films on $Ni_{100-x}W_x$ underlayers 135
5.3.2 Deposition of $SmCo_5$ films on Ni_4W underlayers 138
5.3.2.1 Effect of deposition temperature of $SmCo_5$ 138
5.3.2.2 Effect of thickness of Ni_4W underlayer 142
5.3.2.3 Effect of thickness and composition of $SmCo_5$ layer 144
5.3.3 Deposition of $SmCo_5$ film on Ni / Ni_4W underlayer 145
5.4 Summary 146
5.5 References 148
6 Chapter VI Conclusion and future work 149
6.1 Conclusion 150
6.2 Future work 152

List of Figures

Fig. 1.1. Areal density trends of hard disk drives [1]. 4

Fig. 1.2. Different types of magnetic recording media....5

Fig. 1.3. Schematic diagram of longitudinal recording system [3]. 6

Fig. 1.4. Schematic diagram of an AFC medium [3]. 6

Fig. 1.5. Schematic diagram of perpendicular recording system [3]....8

Fig. 1.6. Phase diagram of Sm-Co binary alloys [58]. 14

Fig. 1.7. Illustration of crystal structure of $SmCo_5$....15

Fig. 2.1. Schematic diagram of DC sputtering system. 30

Fig. 2.2. Schematic illustration of X-ray diffraction. 34

Fig. 2.3. Schematic diagram for TEM bright field imaging. 37

Fig. 2.4. Schematic diagram for TEM dark field imaging. 37

Fig. 2.5. Schematic diagram of an AFM system [12]. 40

Fig. 2.6. Schematic diagram of a VSM system. 42

Fig. 2.7. Typical hysteresisi loop....45

Fig. 2.8. Angular dependence of coercivity based on S-W model and domain wall motion model....47

Fig. 2.9. Schematic explanation to measure the field dependant magnetisation remanence (M_r) and demagnetization remanence. 48

Fig. 2.10. Illustration of typical DCD and IRM curves. Hollow circle represents IRM curve and solid square represents DCD curve. 48

Fig. 2.11. Schematic δM curves illustrating different coupling regimes [22]. 49

Fig. 3.1. Illustration of the epitaxial relationship: $SmCo_5$ $(11\bar{2}0)$ <0001> // Cr (200) <011> // MgO (200) <010>. 53

Fig. 3.2. Schematic diagram of the multilayer film structure. 54

Fig. 3.3. XRD spectra of 60 nm Cr thin films deposited at different temperatures: from room temperature to 500 ^oC. 56

Fig. 3.4. AFM images of the surface of the Cr underlayer deposited (a) at 400 °C, (b) at 500 °C and (c) dependence of R_q of Cr films on the deposition temperature. 57

Fig. 3.5. XRD spectra of Cr thin films with different thicknesses deposited at 400 °C: from 30 nm to 95 nm....58

Fig. 3.6. Dependence of R_q of Cr films with different thickness. 59
Fig. 3.7. Relation between deposition rate of Sm and deposition power. 60
Fig. 3.8. RBS spectra of SmCo thin films deposited on Si substrate: (a) Sm at 14 W and Co at 50 W and (b) Sm at 20 W and Co at 50 W. The open circles represent the experimental data, whereas the solid curves represent the simulated data. 61
Fig. 3.9. XRD spectra of Cr/Sm-Co/Cr thin films with the Cr underlayers deposited at different temperatures: (a) room temperature, (b) 200 °C, (c) 300 °C, (d) 400 °C, (e) 500 °C. 63
Fig. 3.10. M-H loops of $SmCo_5$ thin film with Cr underlayers deposited at different temperatures. 65
Fig. 3.11. Dependence of in-plane and out-of-plane ${}_iH_c$ of $SmCo_5$ films on the Cr underlayer deposition temperature. 65
Fig. 3.12. XRD spectra of Cr / Sm-Co / Cr thin films with (a) 30 nm Cr underlayer and (b) 60 nm Cr underlayer and (c) 95 nm Cr underlayer. The inset is the XRD spectra of $SmCo_5$ $(11\bar{2}0)$ peaks of these three samples with a long time scan. 66
Fig. 3.13. Dependence of in-plane and out-of-plane ${}_iH_c$ in $SmCo_5$ films on the thickness of Cr underlayer. 67
Fig. 3.14. XRD spectra of Cr(40 nm) / Sm-Co(*t* nm) / Cr(60 nm) thin films: (a) *t*=10 nm, (b) *t*=30 nm, (c) *t*=45 nm and (d) *t*=90 nm. 68
Fig. 3.15 Dependence of in-plane intrinsic coercivity in $SmCo_5$ films on the thickness of $SmCo_5$ layer. 69
Fig. 3.16. Dependence of in-plane intrinsic coercivity of $SmCo_5$ thin films on Sm content. 70
Fig. 3.17. XRD spectra of (a) Sample A and (b) Sample B. The inset in (b) shows the selected area electron diffraction (SAED) pattern of Sample B. 72
Fig. 3.18. TEM bright field image and dark field image of Sample B. 73
Fig. 3.19. XRD rocking curves of (a) Cr (200) and (b) $SmCo_5$ (110) peaks of Sample A. 74
Fig. 3.20. XRD off-spectra phi scan of MgO (111), Cr (101) peaks and $SmCo_5$ (111) of Sample A. 74
Fig. 3.21. The illustration of grains distribution in (a) Sample A and (b) Sample B. The arrows indicate the easy axis directions. The solid arrows represent

the easy axes which lie in the film plane and the dash arrows represent those are not in the film plane. 75
Fig. 3.22. M-H loops of (a) Sample A, measured along the MgO [011], MgO [011], and MgO [100] directions; (b) Sample B, measured along 0° in-plane, 45° in-plane and out-of-plane directions. 76
Fig. 3.23. (a) The demagnetization curve and recoil curves for Sample B. (b) The normalized deviation of demagnetization remanence $\Delta M_d(H)$ versus the applied field for Sample A and B. 80
Fig. 3.24. Angular dependence of normalized coercivity of Sample A and Sample B. Zero field refers to in plane direction. 81
Fig. 4.1. Illustration of lattice matching between Cu (111) and $SmCo_5$ (0001). ...86
Fig. 4.2. Schematic diagram of multilayer structure. 88
Fig. 4.3. θ-2θ XRD spectra of Ta films with different thicknesses (0-50 nm). 90
Fig. 4.4. (a) Glancing angle XRD spectra of 4 nm and 10 nm Ta films measured at a fixed 0.5° incidence angle. (b) The electron diffraction pattern of the 4 nm Ta film. 91
Fig. 4.5. (a) AFM images of Ta films with different thicknesses (4 nm, 20 nm and 50 nm). (b) The changes of roughness as a function of film thickness. ..92
Fig. 4.6. (a) θ-2θ XRD spectra of Cu films grown on Ta seed layer of different thicknesses (0-50 nm). (Inset is XRD spectrum of Cu film without Ta seed layer). (b) Rocking curves (ω scan) of 50 nm Cu films grown on Ta seed layer of different thicknesses (0-50 nm).....93
Fig. 4.7. AFM images of 50 nm Cu films grown on (a) glass and (b) 4 nm Ta coated glass substrates. 94
Fig. 4.8. Dependence of $\Delta\theta_{50}$ and R_q of 50 nm Cu films on the thicknesses of Ta seed layer. 95
Fig. 4.9. XRD spectra of 65 nm $SmCo_5$ films grown on (a) glass and (b) a 4 nm Ta coated glass substrates. 97
Fig. 4.10. M-H loops of the samples (a) without seed layer and (b) with a 4 nmTa seed layer. 98
Fig. 4.11. Dependence of out-of-plane $_iH_c$ of $SmCo_5$ on the thickness of Ta seed layer. 99
Fig. 4.12. EDX spectrum of the $SmCo_5$ layer. 101

Fig. 4.13. (a) TEM bright field image, (b) dark field image and (c) high resolution image of cross sectional sample of Ta (20 nm) / $SmCo_5$ (65 nm) / Cu (50 nm) / Ta (4 nm).....102
Fig. 4.14. XRD spectra of the samples with $SmCo_5$ layer deposited at different temperatures of (a) 300 ^oC; (b) 325 ^oC; (c) 350 ^oC; (d) 400 ^oC and (e) 450 ^oC. 103
Fig. 4.15. M-H loops of the samples with $SmCo_5$ layers deposited at different temperatures of (a) 300 ^oC; (b) 325 ^oC; (c) 400 ^oC and (d) 450 ^oC. 105
Fig. 4.16. XRD spectra of Ta / $SmCo_5$ / Cu / Ta thin films with (a) a 15 nm Cu underlayer, (b) a 25 nm Cu underlayer, (c) a 50 nm Cu underlayer and (d) a 100 nm Cu underlayer. 106
Fig. 4.17. Dependence of in-plane and out-of-plane $_iH_c$ in $SmCo_5$ films on the thickness of Cu underlayer. 108
Fig. 4.18. XRD spectra of Ta (20 nm) / $SmCo_5$ (t nm) / Cu (50 nm) / Ta (4 nm) thin films: (a) t=23 nm, (b) t=35 nm, (c) t=45 nm, (d) t=65 nm and (e) t=90 nm. 109
Fig. 4.19. Dependence of in-plane and out-of-plane intrinsic coercivity in $SmCo_5$ films on the thickness of $SmCo_5$ layer. 110
Fig. 4.20. XRD spectra of 65 nm Sm-Co films with different Sm contents grown on Ta (4 nm) / Cu (50 nm) underlayers. 111
Fig. 4.21. Dependence of full width at half maximum of the rocking curves ($\Delta\theta_{50}$) and integral intensity of (0002) peaks of $SmCo_5$ according to the Sm-Co composition. 112
Fig. 4.22. Dependence of in-plane and out-of-plane $_iH_c$ of Sm-Co films on the Sm-Co composition.....113
Fig. 4.23. (a)XRD spectrum and (b) M-H loops of the $SmCo_5$ film grown on Cu / Ti dual underlayer. 115
Fig. 4.24. (a)XRD spectrum and (b) M-H loops of the $SmCo_5$ film on Cu / W dual underlayer. 116
Fig. 4.25. Angular dependence of normalized coercivity of the $SmCo_5$ films grown on Cu / Ta, Cu / Ti and Cu / W underlayers. Zero field refers to out-of-plane direction. 117
Fig. 5.1. Illustration of lattice matching between Ni (111) and $SmCo_5$ (0001)...124
Fig. 5.2. Phase diagram of Ni-W binary alloys [6].....125

Fig. 5.3. (a) Tetragonal unit cell of Ni_4W. (b) The relationship between the Ni_4W (211) plane and the $SmCo_5$ (0001) plane. 127
Fig. 5.4. Schematic diagram of the multilayer structure. 128
Fig. 5.5. XRD spectra of 40 nm Ni films (a) with a 4 nm W seed layer and (b) without seed layer. 129
Fig. 5.6. (a) XRD spectra of 40 nm Ni-W layers with a varying W atomic percentage (0 at.% ~ 100 at.%) grown on 4 nm W coated glass substrates. (b) The inter-planar spacing and peak integral intensity of Ni (111) and Ni_4W (211) as a function of W content. 131
Fig. 5.7. XRD spectrum of the obtained $Ni_{80}W_{20}$ sample within a range from 20º to 120º. 132
Fig. 5.8. (a) TEM images and diffraction patterns of 40 nm Ni, $Ni_{80}W_{20}$ (Ni_4W), $Ni_{68}W_{32}$ and $Ni_{50}W_{50}$ films grown on 4 nm W coated glass substrates. (b) AFM images of 40 nm Ni, $Ni_{80}W_{20}$, and $Ni_{68}W_{32}$ films grown on 4 nm W coated glass substrates. 133
Fig. 5.9. M-H loops of Ni-W alloys with from 0 at.% to 20 at.% of W measured in the direction of perpendicular to the film plane at room temperature by VSM. 134
Fig. 5.10. Relation between the W content and the saturation magnetization of Ni-W thin films. 134
Fig. 5.11. XRD spectra of 65 nm $SmCo_5$ films grown at 530 °C on 40 nm $Ni_{100-x}W_x$ (x = 0 ~100) underlayers. 135
Fig. 5.12. (a) Summary of in-plane and out-of-plane coercivities of 65 nm $SmCo_5$ films grown at 530 °C on 40 nm $Ni_{100-x}W_x$ (x = 0 ~100) underlayers. (b) M-H loops of 65 nm $SmCo_5$ films grown on 40 nm $Ni_{68}W_{32}$ layers on 4 nm W coated glass substrates. 137
Fig. 5.13. XRD spectra of W 4 nm / Ni_4W 50 nm / SmCo 65 nm (410~550 °C) / W 20 nm (410~550 °C) thin films. 139
Fig. 5.14. (a) Relation between the deposition temperature and the in-plane and out-of-plane intrinsic coercivities of SmCo in W 4 nm / Ni_4W 40 nm / SmCo 65 nm (410~550 °C) / W 20 nm (410~550 °C) thin films. (b) M-H loops of $SmCo_5$ deposited at 500 °C in perpendicular and longitudinal directions. 140

Fig. 5.15 (a) TEM bright field image and (b) dark field image of a cross sectional sample of W 4 nm / Ni_4W 40 nm / $SmCo_5$ 65 nm (500 °C) / W 20 nm (500 °C) thin films.....141

Fig. 5.16. Angular dependence of the normalized coercivity of the $SmCo_5$ film grown on Ni_4W / W underlayer. Zero field refers to out-of-plane direction.....142

Fig. 5.17. Dependence of the out-of-plane coercivity on the thickness of Ni_4W underlayer for a film structure of W (20 nm) / Sm-Co (65 nm) / Ni_4W (0-80 nm) / W (4 nm). 143

Fig. 5.18. (a) Dependence of the out-of-plane and in-plane coercivity on the thickness of $SmCo_5$ magnetic layer for a film structure of W (20 nm)/ Sm-Co (20-100 nm)/Ni_4W (40 nm)/W (4 nm). (b) Dependence of the out-of-plane and in-plane coercivity on the Sm content for a film structure of W (20 nm)/ Sm-Co (65 nm)/Ni_4W (40 nm)/W (4 nm). 144

Fig. 5.19. (a) XRD spectrum, (b) illustration of layer structure and (c) M-H loops of 65 nm $SmCo_5$ films grown at 530 °C on Ni (20 nm) / Ni_4W (20 nm) / W (4 nm) layers on glass substrate.....146

List of Tables

Table 1.1. Magnetic properties and theoretical minimal grain diatemeters of various media candidates of high magnetic crystal anisotropy constant, K_u. (Courtesy of D. Weller and R. Skomski [57])....13

Table 3.1. Calibration of the atomic compositions of Sm-Co films deposited at different powers....61

Table 3.2. Film structure and magnetic properties of Sample A and Sample B. 71

Table 4.1. Melting temperatures (T_m) and calculated values of surface free energies (γ_i^o) at room temperature of different materials [16]. 87

Table 4.2. The positions of SmCo(Cu) (0002) peak in θ - 2 θ XRD spectra and the lattice constants a and c. The values for $SmCo_5$, $SmCo_{3.3}Cu_{1.7}$, $SmCu_5$ are based on PDF File No. 35-1400, No. 23-934 and No. 65-933, respectively....101

Table 4.3. $\Delta\theta_{50}$ of Cu (111) peak and $SmCo_5$ (0002) peak of Ta/Sm-Co/Cu/Ta thin films with different Cu thicknesses. 107

Table 4.4. $\Delta\theta_{50}$ of $SmCo_5$ (0001) peak and $SmCo_5$ (0002) peak in $SmCo_5$ films with different thicknesses. 109

Table 4.5. $\Delta\theta_{50}$ of the Cu (111), $SmCo_5$ (0001) and $SmCo_5$ (0002) peaks and R_q of Cu underlayers for film samples with different seed layers. 116

Table 5.1. Metals with a melting temperature (T_m) higher than 1200 ^oC and with a fcc or a hcp structure and the lattice misfits between these metals and $SmCo_5$. "+" represents a bigger lattice constant of listed metal compared with that of $SmCo_5$, whereas "-" represents a smaller lattice constant of listed metal compared with that of $SmCo_5$……...123

List of Publications

1. **L. N. Zhang**, J. F. Hu, J. S. Chen and J. Ding, "$SmCo_5$ with perpendicular anisotropy induced by Ni $_4$W underlayer", IEEE transactions on magnetics (In press).

2. **L. N. Zhang**, J. F. Hu, J. S. Chen and J. Ding, "Nanostructured $SmCo_5$ thin films with perpendicular anisotropy formed in a wide range of Sm-Co compositions", J. Nanosci. Nanotechnol (In press).

3. **L. N. Zhang**, J. F. Hu, J. S. Chen and J. Ding, "Microstructure and magnetic properties tudies of $SmCo_5$ thin films grown on MgO and glass substrates", J. Magn. Magn. Mater. 321, 2643 (2009).

4. **L. N. Zhang**, J. F. Hu, J. S. Chen and J. Ding, "Seed layer effect on texture and magnetic properties of $SmCo_5$ thin films", J. Appl. Phys. 105, 07A743 (2009).

5. J. S. Chen, **L. N. Zhang**, J. F. Hu and J. Ding, "Highly textured $SmCo_5$ (001) thin film with high coercivity", J. Appl. Phys. 104, 093905 (2008).

6. **L. N. Zhang**, J. S. Chen, J. Ding, and J. F. Hu, "High-coercivity $SmCo_5$ thin films deposited on glass substrates", J. Appl. Phys. 103, 113908 (2008).

1 Chapter I Introduction

1.1 Magnetic recording and magnetic recording media

1.1.1 A brief review of magnetic recording

The idea of magnetic recording was first proposed by Oberlin Smith in 1878 in the form of audio recording on a wire. In 1898, a young Danish engineer, Valdemar Poulsen, invented and patented the first successful magnetic recording device which was named as "Telegraphone". The idea is to record sound by varying the magnetization of a steel wire wrapped around a copper drum. In 1928, Fritz Pfleumer developed the "Magnetophone" -- the first magnetic tape recorder, using powdered magnetic materials coating on thin plastic tapes and ring-type magnetic head. This recorder enormously improved the quality of audio magnetic recording. After that, the technique of magnetic recording has received significant attention because of its great potential for commercial applications.

Digital magnetic storage was introduced in 1947. The fundamental principle of magnetic storage is the conversion between magnetic field and electrical current. Any type of information to be recorded including audio, video, and numerical data can be expressed as a time-varying electrical current. During the writing process, when the current passes the recording head, it establishes a magnetic field in the head accordingly. Then the head field magnetizes the recording medium. As a result, the time-varying electric signal is transformed into a spatially magnetic pattern along tracks on the recording medium surface. On the other hand, during the read process, when the recorded medium is moved across the gap of a magnetic circuit, the field above the written bits induces a flux change in the head. Then the flux change induces a corresponding voltage in the coil of the read head. This voltage is amplified and read with an electronic signal processor to recognise the information.

The first model of hard disk drive – "RAMAC" (Random Access Method of Accounting and Control) was invented by IBM in 1956. It had a recording density of 2,000 bits/inch^2 and a total capacity of 5 megabytes. Nowadays in the digital era, hard disk drive has become one of the most popular data storage devices because of its high capacity, short access time and low price per recording unit. With the fast growing popularity of giant audio and video files, more and more research has been devoted to developing hard disk drives with higher recording density to meet the fast growing demand of high capacity storage. The major parameter for the recording quality is the areal density. The areal recording density of hard disk drives had increased at a sustained annual rate of 30% from 1960s to 1991. Since 1991, new technologies such as advanced thin-film media and anisotropic magnetoresistance heads (MR heads) had brought this rate to an amazing 60% per year. After 1997, the rate further increased to 100%. The enormous improvements come from the development of high-coercivity media and giant magnetoresistance heads (GMR heads). Since 2005, the rapid growth rate has been maintained thanks to the application of perpendicular magnetic recording (PMR) and tunneling magnetoresistance heads (TMR heads) technologies. In 2008, the Japanese company TDK announced the current world's highest recording density of 803 Gbits/inch^2 by using PMR and TMR heads technologies. This value is 10^8 times the recording density of the first IBM device. The history of areal density increase is summarized in Fig. 1.1 [1].

Although a part of the market of information storage (for example mp3 players) has been taken over by the flash memory drives, the use of hard disk devices will continue to dominate the information storage market because of their much larger storage capacity and the huge demand in information storage that will continue to grow in the future [2].

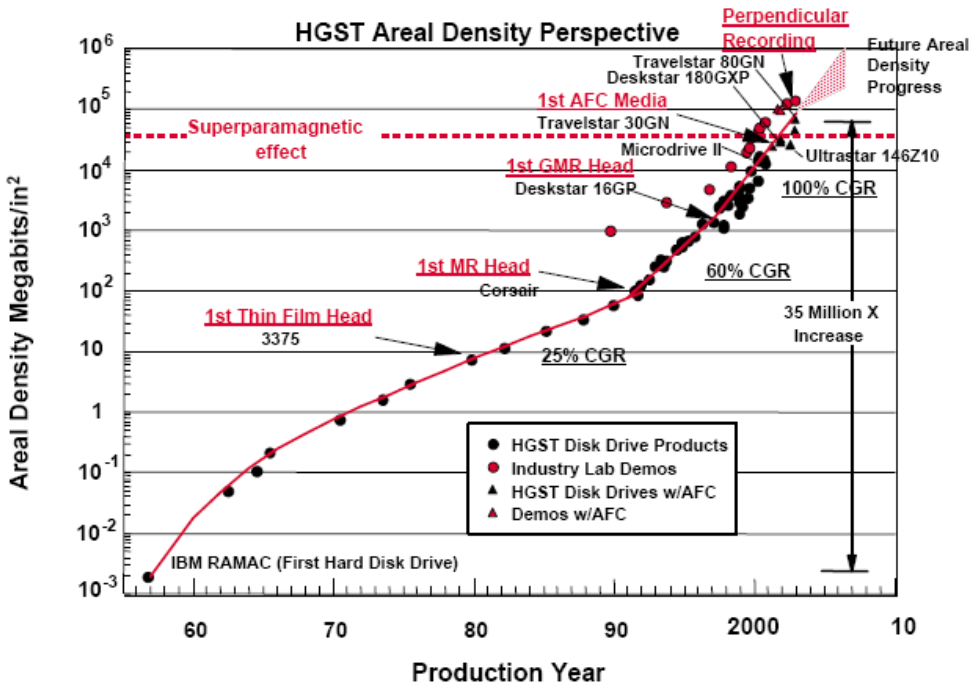

Fig. 1.1. Areal density trends of hard disk drives [1].

1.1.2 Development of magnetic recording media

A variety of magnetic recording media have been used in the past 100 years. As discussed above, ferrous wires were used in very early recorders. Magnetic layers with magnetic particles (such as gamma ferric oxide) formed in a polymer matrix are used in tapes for audio and video recording. Thin magnetic films deposited in a vacuum are used for the most modern digital data storage (flexible or rigid disks). Various types of magnetic recording media are shown in Fig. 1.2.

In digital recording, several methods are developed in order to record the bits. The choice of the recording method determines the requirements of structure and properties of recording media. The details of different recording methods and recording media are described in the following sections.

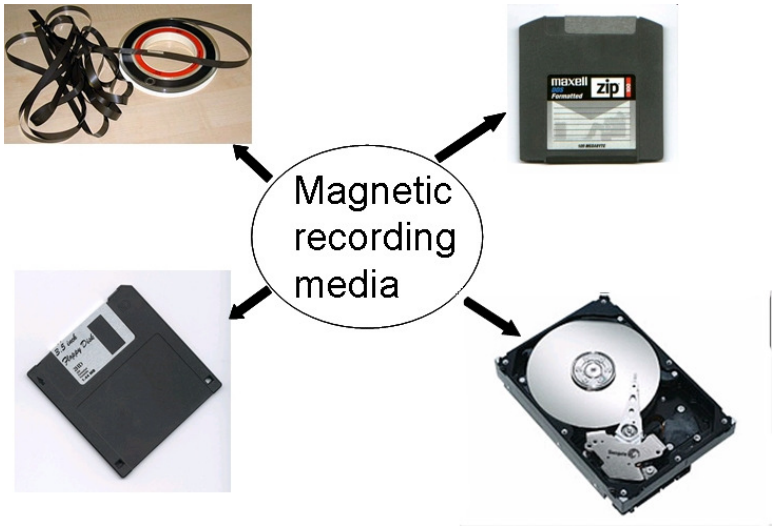

Fig. 1.2. Different types of magnetic recording media.

1.1.2.1 Longitudinal magnetic recording media

Longitudinal magnetic recording (LMR) is a conventional recording method. Most of commercial hard disk drives are based on this technology. The system contains a ring writing head and a magnetoresistive (MR) reading head as shown in Fig. 1.3 [3]. It prefers media with crystallites oriented longitudinally where the easy axis of magnetization lies in the film plane. In a longitudinal recording medium, the remanent magnetization (M_r) in the longitudinal direction is much higher than the other directions. The demagnetization factor is proportional to $M_r t/\lambda$ where M_r is the remanent magnetization of recording medium; t is the thickness of the film and λ is the bit length. As the recording density is increasing, λ becomes smaller, the demagnetization factor becomes less favourable unless the depth of film is reduced. However, reducing the thickness of the film would lower the read signal strength, which is proportional to $M_r t$. In order to overcome the contradiction of this structure, antiferromagnetically coupled (AFC) media was developed as an improved

longitudinal recording medium.

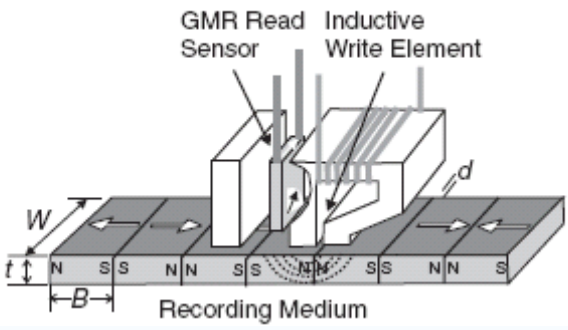

Fig. 1.3. Schematic diagram of longitudinal recording system [3].

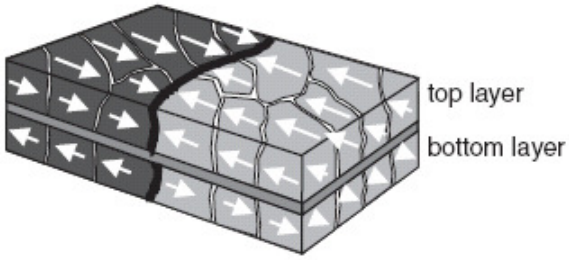

Fig. 1.4. Schematic diagram of an AFC medium [3].

AFC media were introduced by IBM [4] and Fujitsu [5] independently in 2000. It is a great improvement in longitudinal recording technology. This kind of recording media consists of two magnetic antiferromagnetically coupled layers connected by a non-magnetic Ru layer as shown in Fig. 1.4 [3]. Because the two magnetic layers are magnetized in antiparallel directions, the effective thickness $M_r t_{eff}$ (also referred to as the remanence-thickness product) is reduced to the difference in $M_r t$ values for each of the two magnetic layers. This leads to smaller transition parameter and enhanced thermal stability. Thus, it promotes higher recording density.

The first longitudinal recording media introduced in 1952 were hexagonal close

packed (hcp)-cobalt (Co) thin films made by electrochemically deposition. They had a coercivity of less than 300 Oe. Since then, the hcp-Co alloys with the c-axis lying in the film plane have been employed for decades as the primary longitudinal recording layer materials. The Co-alloys with in-plane anisotropy are usually induced by a chromium (Cr) underlayer. The growth orientations of the Co-alloy layer on the Cr underlayer have been identified as Co $(11\bar{2}0)$ // Cr (100), Co $(10\bar{1}0)$ // Cr (112) and Co $(10\bar{1}1)$ // Cr (110) [6-10]. Since the anisotropy of pure Co is not very large, platinum (Pt) is usually added to increase the magnetocrystalline anisotropy field. This is because Pt is polarized when incorporated in a magnetic structure [11]. High anisotropic Co rich Co-Pt alloys such as $Co_{80}Pt_{20}$ are used [12]. In order to de-couple the magnetic grains, Cr is added in the Co-alloy matrix. The non-magnetic Cr precipitant at the grain boundaries enables the segregation. Boron (B) addition has been found to enhance the segregation. However, with increasing B concentration, stacking faults would appear [13]. The essential problem for metallurgical segregation is the inevitable fluctuations of Cr distribution from grain to grain [14]. Moreover, Cr is also known to reduce the magnetization and anisotropy field of Co-alloys [15].

1.1.2.2 Perpendicular magnetic recording media

From the end of the 1990s, perpendicular recording has been promoted as the approach to achieve higher areal densities because of the thermal stability limitation in longitudinal recording media (see discussion in section 1.1.3). The configuration of perpendicular recording is shown in Fig. 1.5 [3]. It consists of a single pole writing head instead of a ring head in longitudinal recording and a double-layered media composed of a recording layer and a soft magnetic underlayer (SUL). The writing

process occurs in the write pole and the flux path is closed through the SUL and the collector pole. This configuration almost doubles the write field compared to longitudinal recording method [16].

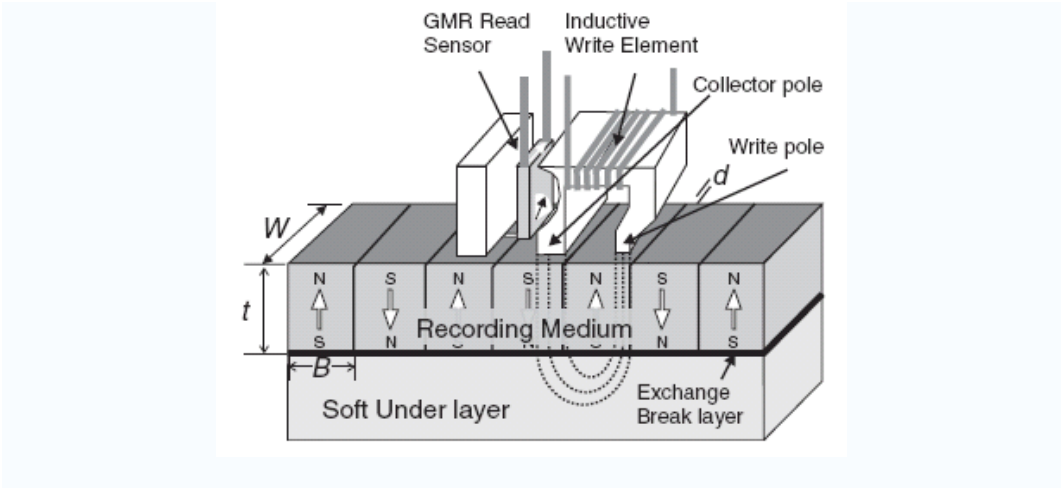

Fig. 1.5. Schematic diagram of perpendicular recording system [3].

The perpendicular recording requires media with crystallites oriented perpendicularly to the film plane where the easy axis of magnetization lies normal to the film. Such media have a much higher remanent magnetization in the perpendicular direction, and favor perpendicular recording. The grains in perpendicular recording media have a strong uniaxial orientation whereas the longitudinal media tent to have a random orientation in the film plane. Thus, the perpendicular media have narrower switching field distribution and sharper written transition [16]. Actually, this method has been advocated for the past 30 years. It was first proven advantageous by Professor Shun-ichi Iwasaki from the Tohoku Institute of Technology in Japan in 1976. However, the practical implementation of perpendicular recording failed because of "engineering problems" rather than fundamental ones [17]. This technology has undergone fast and substantial development in the past 10 years. In June 2005, the first

HDD employing the perpendicular magnetic recording system was commercialized. It achieves an areal recording density of 133 Gbit/inch^2.

hcp-Co alloys are also used in industry for perpendicular recording media. The (0001) textured Co-alloys are generally induced by (0002) textured ruthenium (Ru)-alloy underlayers [18-20]. In the perpendicular Co-alloys recording media, the metallurgic segregation is replaced by non-magnetic oxides such as SiO_2, Ta_2O_5 and TiO_2 [21-24]. Because these oxides do not incorporate into the growing Co-alloy crystals, uniform two-phase microstructure with de-coupled grains forms through the whole thickness of the film. Therefore, the compositional variation occurring in metallurgic segregated Co-alloys is avoided. However, the upper density limit of current CoPt media is anticipated as 600 Gbit/in^2 because of their relatively low magnetic anisotropy. Therefore, $L1_0$ ordered FePt and hcp-$SmCo_5$ with very high magnetic anisotropy are investigated for next generation media as discussed in section 1.1.3.

Another approach to achieve high perpendicular anisotropy exploits the interface anisotropy in very thin films. Co / Pd and Co / Pt multilayered films exhibiting strong perpendicular magnetic anisotropy [25-29]. However, there is a serious problem that these recording media suffer from high media noise, resulting from large magnetic clusters produced by strong intergranular exchange coupling [30].

With the increasing coercivity of recording media, the write-ability is meeting an obstacle. Since so far the maximum obtainable saturation magnetization of a single pole is 2.4 T (CoFe), it is not high enough to switch the recording media with high anisotropy and coercivity. Recently, the exchange coupled composite (ECC) media have attracted great interest theoretically and experimentally [31-42]. This design can help to solve the write-ability problem. The basic idea of ECC is to use a soft layer as a

switching assistant for the hard layer without compromising thermal stability in zero applied field. Victora et al. [31, 32] theoretically predicted that ECC media consisting of magnetically hard and soft regions within each grain will reduce the switching field. This proposal was subsequently demonstrated by Wang et al. [34]. Okamoto et al. observed a decrease of coercivity of epitaxial FePt $L1_0$ nanoparticles covered with different thicknesses of Pt over-layers, while the energy barrier remains unaltered [38]. Dobin et al. demonstrated that the ultimate potential of the composite media is realized if the interfacial domain wall fits inside the layers. The switching occurs via domain wall nucleation, compression in the applied field, depinning, and propagation through the hard/soft interface [42]. The ECC media may allow high anisotropy materials such as $L1_0$ ordered FePt and hcp-$SmCo_5$ into application.

1.1.2.3 Future magnetic recording media

Heat assisted magnetic recording (HAMR) and bit-pattern media have been identified as future technologies to extend magnetic recording. HAMR bases on the temperature dependence of the anisotropy of recording media [43]. The idea is to temporally heat the recording medium close to its Curie temperature, which reduces the magnetic anisotropy and allows writing using currently available writing fields. Then the medium is quickly cooled back to ambient temperature to store the data. Thus it is possible to write information on a medium with high areal density. This new technology has attracted more and more attention. It has been experimentally demonstrated that a laser spot could be used to heat the recording medium from the opposite side of the recording head [44]. HAMR is another technology that allows high anisotropy materials such as $L1_0$ ordered FePt and hcp-$SmCo_5$ to be used.

On the other hand, bit-pattern media rely on a completely different strategy to

achieve high recording density. In this kind of media, one grain or magnetic island represents one bit instead of recording one bit on a large number of grains (50~100) in conventional media [45, 46]. Thus the larger volume grain or island in bit-pattern media stores larger magnetic energy so that stable media can be achieved with lower anisotropy. This technique has been studied for years [47-50]. The critical challenges are the lithographic requirements, because the independent bits need to grow on lithographically predefined substrate. Though pattern media is able to achieve areal density beyond 1 Tbit/inch^2, it is based on the feasibility of lithography for successful patterning of size down to ~10-12 nm at low cost and in a reasonably short time. Different lithography techniques such as deep UV lithography, extreme UV lithography, x-ray lithography, electron beam lithography, nano-imprint lithography and lithography assisted self assembly have been attempted to pattern the size down to 10 nm.

The ultimate density can be achieved by a combination of HAMR and bit-patterned media with high anisotropy materials such as $L1_0$ ordered FePt and hcp-$SmCo_5$.

1.1.3 Challenges of magnetic recording media

From a material scientist's point of view, higher recording density means smaller bit (recording unit) size. For the current magnetic media constructions, each bit is composed of *N* random grains, $V_{bit} = N \bullet V_{grain}$. *N* needs to be large enough (50~100) to hold property variance below some threshold through averaging. In such a situation, signal-to-noise ratio (SNR) is determined by *N*, where SNR ~ 10Log*N*. The need to maintain high *N* for a high SNR forced V_{grain} to be smaller and smaller. However, when the grain size is reduced to a certain level, the magnetic energy stored in each

grain ($K_u \bullet V_{grain}$) becomes as low as the thermal energy existing in each grain ($k_B \bullet T$), where K_u is the magnetic anisotropy density, k_B is the Boltzmann constant and T is the absolute temperature. This will cause instability of the recorded data due to thermal perturbation, a phenomenon called superparamagnetism. Thermally activated switching is characterized by a time constant τ following the Arrhenius Néel law [51]:

$$\tau = \frac{1}{f_0} \exp\left(\frac{K_u V_{grain}}{k_B T}\right) \qquad \text{Eq. 1.1}$$

where τ is the relaxation time, f_0 is the relaxation frequency on the order of 10^9-10^{12} Hz [52]. Based on the above equation, a thermally stable magnetic recording medium for more than 10 years requires a parameter of $K_u V_{grain} / k_B T$ larger than 60 to overcome the superparamagnetic limit [53, 54]. Fortunately, the onset of superparamagnetic limit can be delayed by using ferromagnetic materials with large anisotropy energy. In other words, materials with large anisotropy can maintain thermal stability with smaller grain sizes [53-55].

Table 1.1 summarizes a variety of intrinsic and derived properties for candidate materials. It can be seen that hcp $SmCo_5$ possess the highest magnetic anisotropy density ($1.1\sim2.0\times10^8$ erg/cm^3) among all hard magnetic materials, which allows the thermally stable grain to decrease to 2.4 nm. Therefore, $SmCo_5$ is a potential candidate of the future magnetic recording media. However, its poor corrosion resistance has prevented practical applications. Recent study indicated that its corrosion resistance can be significantly improved by additional Cu which makes it comparable with previously used CoCr media [56]. Therefore, the development of $SmCo_5$ thin film with high magnetic anisotropy either in longitudinal direction or in perpendicular direction has received considerable attention for applications of ultra-high density magnetic recording.

Besides continued reduction in grain size, reduction in grain size distribution and magnetic dispersion, well oriented nanocrystalline structures and control of magnetic grain isolation are also required for high performance recording media.

Table 1.1. Magnetic properties and theoretical minimal grain diatemeters of various media candidates of high magnetic crystal anisotropy constant, K_u. (Courtesy of D. Weller and R. Skomski [57])

Alloy System	Material	K_1 10^7 erg/cm^3	M_s (emu/cm^3)	H_k (kOe)	T_c (K)	$D_p = \sqrt[3]{V_{grain}}$ (nm)
Co-alloys	$CoCr_{20}Pt_{15}$	0.25	330	15.2		12.4
	Co_3Pt	2	1100	36.4	1200	6.9
	$(CoCr)_3Pt$	0.39	410	19		10.6
	$CoPt_3$	0.5	300	33.3	600	8.6
Co/Pt (Pd) multilayer	Co/Pt	1	360	55.6	500	6.7
	Co/Pd	0.6	360	33.3	500	8.2
$L1_0$ phase	FePd	1.7	1100	32.7	760	7.5
	FePt	7	1140	122.8	750	3.6
	CoPt	4.9	800	122.5	840	3.9
	MnAl	1.7	560	60.7	650	5.7
Rare-earth alloy	$Fe_{14}Nd_2B$	4.6	1270	72.4	585	4.5
	$SmCo_5$	20	910	439.6	1000	2.4

where M_s is the saturation magnetization of the materials, H_K is the anisotropy field ($H_K = 2K_1/M_s$), T_c is the Curie temperature, D_p is grain size for cubic grains.

1.2 Physical properties of $SmCo_5$

1.2.1 Phase diagram and crystal structure of $SmCo_5$

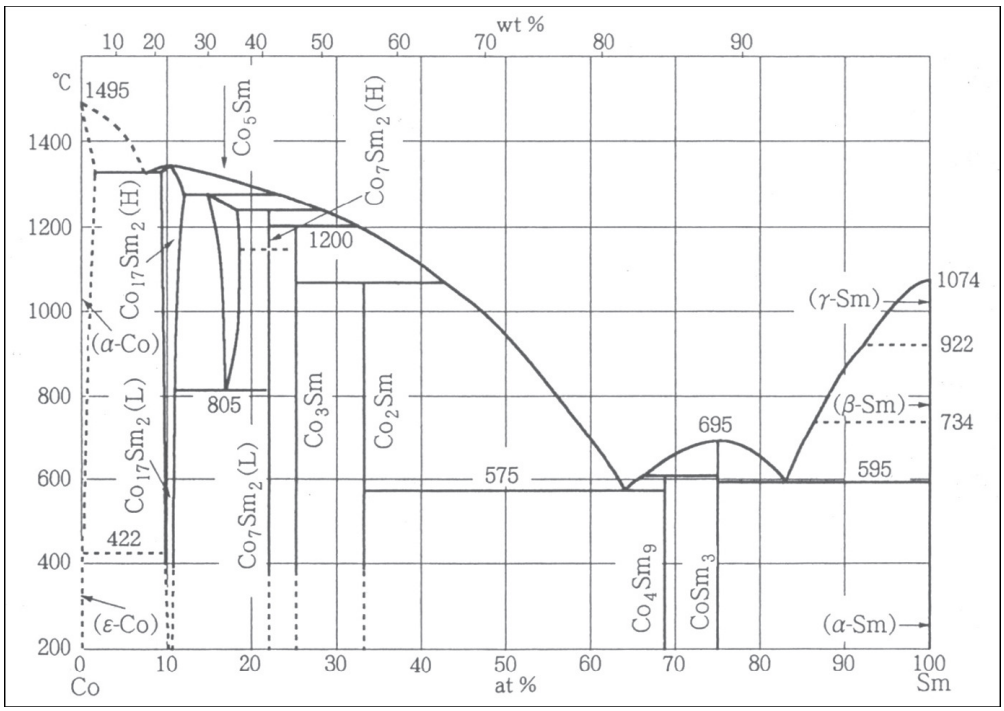

Fig. 1.6. Phase diagram of Sm-Co binary alloys [58].

A typical Sm-Co binary alloys phase diagram is shown in Fig. 1.6 [58]. This phase diagram is based on bulk Sm-Co materials where $SmCo_5$ phase is stable only above 805 ^oC. For thin film materials, the temperature for the formation of $SmCo_5$ phase is much lower around 300~500 ^oC as shown later in Chapters 3 to 5. The hexagonal $CaCu_5$ structure of $SmCo_5$ is illustrated in Fig. 1.7. It is a layer-by-layer configuration along to c-axis, consisting of a stack of hexagonal Co layers and hexagonal layers containing both Co and Sm atoms (rotated by $\pm 30^o$).

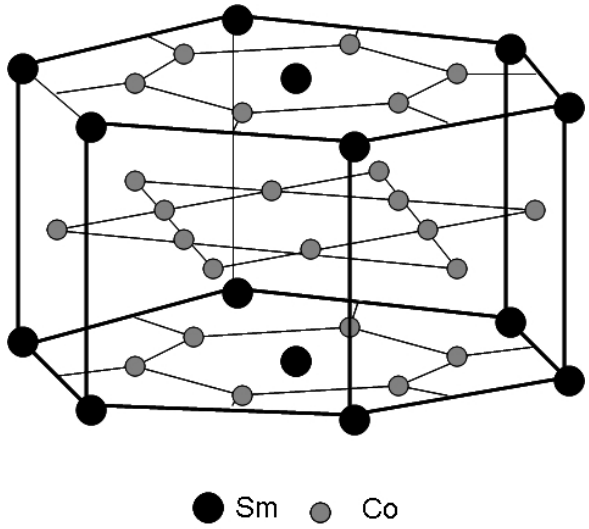

Fig. 1.7. Illustration of crystal structure of $SmCo_5$.

1.2.2 Ferromagnetism, magnetic anisotropy and coercivity mechanism of $SmCo_5$

Ferromagnetism describes the magnetization mechanism of ferromagnetic materials in which the spins are spontaneously arranged parallel to each other, resulting in a net moment. With increasing temperature, the arrangement of the spins is disturbed by thermal agitation which is accompanied by a decrease of spontaneous magnetization. At a certain temperature, called the Curie point (T_c), the thermal agitation leads to a random arrangement of the spins and the spontaneous magnetization vanishes. Above the Curie point, the substance exhibits paramagnetism. Magnetic anisotropy describes the magnetization preference along certain crystallographic directions. The excess energy required to magnetize a unit volume of a crystal in a particular direction with respect to the energy needed in the easy axis direction is called magnetocrystalline anisotropy energy. K_u is used to represent the magnetocrystalline anisotropy energy density.

The ferromagnetism and high anisotropy of Sm are related to its incompletely filled 4f-shell. Electrons in such orbital are strongly localized and therefore easily retain their magnetic moments and function as paramagnetic centers [59]. Magnetic moments in other orbitals are often lost (quenched) due to strong overlap with the neighbors. The magnetic structure of $SmCo_5$ is usually described as consisting of Sm sublattice and Co sublattice, respectively, each being ferromagnetic with itself. The Co magnetic moments couple ferromagnetically with Sm moments. The net magnetic moments of $SmCo_5$ are the sum of these two sublattices. The net anisotropy of $SmCo_5$ is determined by the individual sublattice ainisotropies and the inter-sublattice exchange interaction [60]. Sm favors the c-axis alignment of Co, thus the Co anisotropy is strengthened ($SmCo_5$).

Possible coercivity mechanisms of Sm-Co compounds have been investigated. Livingston interpreted that the coercivity of single-phase bulk $SmCo_5$ was dominated by the nucleation of reverse domains [61]. Givord and Rossignol studied from an energetic approach and pointed out that a nucleus of $SmCo_5$ expends by a thermally excited process [62]. Singh et al. investigated the coercivity mechanism of epitaxial $SmCo_5$ thin films recently [63]. They found that the high coercivity in $SmCo_5$ film is attributed to the pinning of domain walls at inhomogeneities.

1.3 Review of studies on $SmCo_5$ thin films

Since the 1970s, $SmCo_5$ thin films have been investigated by many research groups worldwide for their potentially large magnetic anisotropy and high coercivity. These studies found that the control of the crystallographic texture of thin films is the key factor to obtain the desired magnetic properties. The particular crystallographic texture of $SmCo_5$ can be induced by single crystal substrates since the substrates

themselves process particular texture. If the lattice mismatch between $SmCo_5$ and the single crystal substrate is small enough (<10%), the desired $SmCo_5$ texture can be obtained by epitaxial growth.

Epitaxial growth of $SmCo_5$ films with either a $(11\bar{2}0)$ texture or $(10\bar{1}0)$ texture have been obtained when $SmCo_5$/Cr layers were deposited on MgO (100), MgO (110) and Si (100) single crystal substrates. Instead of depositing $SmCo_5$ thin films directly to substrates, it has been reported that growth onto an epitaxial buffer layer allows the phase and orientation of $SmCo_5$ films to be easily controlled. Cr has been widely used as a buffer layer on MgO substrates, because the lattice misfit between Cr and MgO is less than 4% which is smaller than that between $SmCo_5$ and MgO (7%). Therefore, Cr can follow a good heteroepitaxial growth on MgO and pass the epitaxial growth to $SmCo_5$. Moreover, Cr can decrease the elastic distortion between $SmCo_5$ films and substrates. In addition, Cr underlayer has been found helpful for producing dense films with smaller grain size and smoother surface. Fullerton et al. [64] and Singh et al. [65, 66] have intensively studied $SmCo_5$ grown on MgO single crystal substrates. The epitaxial relationships have been identified as $SmCo_5$ $(11\bar{2}0)$ <0001> // Cr (200) <110> // MgO (200) <010> and $SmCo_5$ $(10\bar{1}0)$ <0001> // Cr (112) <$1\bar{1}$0> // MgO (110) <001>. They further reported that $SmCo_5$ films with a $(11\bar{2}0)$ texture exhibit higher coercivity than that of $SmCo_5$ films with $(10\bar{1}0)$ texture. Benaissa and Speliotis reported the results of epitaxial $SmCo_5$/Cr growth on Si (100) substrate [67]. All of these $SmCo_5$ films grown on single crystal substrates with Cr buffer layer exhibited high coercivity (>10 kOe) and large longitudinal magnetic anisotropy. Epitaxial growth indeed provides a good approach to control the crystal orientation and structure

and to study their influence on the magnetic properties of the $SmCo_5$ thin films. However, the single crystal substrates are quite expensive which limit the practical application.

On the other hand, amorphous glass substrate is a prefered substrate for magnetic recording, because it is **cheap, strong, hard, stiff and light**. It is suitable for lowering access time and increasing data rates. The growth of $SmCo_5$ with longitudinal anisotropy on glass substrate has been studied in the early 1980s [68, 69]. However, amorphous Sm-Co films with small in-plane intrinsic coercivity (<3 kOe) was obtained. In 1985, Aly et al. synthesized $SmCo_5$ on glass substrate with high coercivity by applying a external magnetic field in the substrate plane during rf sputtering. However, only a small amount of in-plane anisotropy has been achieved [70]. From 1990s, the Cr underlayer has been applied to glass substrate to induce in-plane coercivity in Sm-Co films [71-78]. High coercovity and large anisotropy Sm-Co films with hundreds of nanometers thickness were obtained on glass substrates after high temperature annealing (>700^o C) [76-78]. In 2007, Zhang et al. reported a very high in-plane coercivity of 56 kOe of $SmCo_5$ / Cr after a rapid postannealing at 750^o C [79]. However, the high annealing temperature would demage the glass substrates and is not favourable for industrial application. Therefore, it is still necessary to develop the technology for obtaining $SmCo_5$ thin films with large longitudinal magnetic anisotropy and high in-plane coercivity grown on glass substrate at a relatively low temperature.

Recently, $SmCo_5$ thin films with perpendicular anisotropy have attracted great attention for perpendicular recording. The possibility of growing (0001) textured $SmCo_5$ crystallites with perpendicular anisotropy on Cu (111) underlayer has been demonstrated [80-86]. However, the thickness of Cu needs to be larger than 100 nm to obtain the desired texture and good crystallinity. The texture of $SmCo_5$ thin films

deposited on the thick Cu underlayer is poor. Hence, the thickness of the Cu underlayer needs to be reduced and the texture of $SmCo_5$ film needs to be improved as well. In addition, there is non-controlled diffusion of Cu from Cu underlayer into $SmCo_5$ layer which make it difficult to optimize the microstructure and the magnetic properties of $SmCo_5$ thin films. Therefore, it is necessary to find a suitable underlayer with higher melting point than Cu and small lattice misfit between itself and $SmCo_5$. An effort has been made by X. Liu et al. recently. They used polycrystalline Ru(Cr) underlayer to achieve relatively small grain size and good perpendicular anisotropy of $Sm(CoCu)_5$ [87].

1.4 Motivations and objectives

As reviewed in section 1.1.3, a major characteristic of the $SmCo_5$ alloy is its extremely strong uniaxial magnetocrystalline anisotropy with a K_u of more than 1.1×10^8 erg/cm^3. The strong magnetic anisotropy brings large coercivity. In addition, the $SmCo_5$ alloy has a high Curie temperature. These unique properties give $SmCo_5$ thin films a very interesting potential for various magnetic applications including magnetic recording. $SmCo_5$ thin film is a promising candidate for magnetic recording devices to achieve an areal density in excess of 10 Tbit/in^2. However, only a few research groups have obtained satisfactory results so far because Sm oxidizes easily. Furthermore, it is difficult to obtain the $SmCo_5$ phase and to control particular textures. Hence, the broad objective of this research project is to carry out a systematic study on $SmCo_5$ thin films for use in magnetic recording. The main approach used in this work is layer engineering. The structure and magnetic properties of $SmCo_5$ thin films are greatly influenced by the texture and the surface morphology of the underlayer. In this study, I worked on the deposition method in order to control the structure and the

surface morphology of the different layers. Several deposition parameters have been specifically considered. Temperature is the main factor that controls the phase formation, crystallization and microstructure whereas the thickness of the different layers affects the texture and the surface morphology and the composition of the alloy significantly influences the formation of the alloy phase.

The specific objectives of this study are the following:

1. To explore the feasibility of depositing $SmCo_5$ thin films with longitudinal magnetic anisotropy and high in-plane coercivity on glass substrates with Cr underlayers (Chapter 3). In particular:
   - To explore the method of controlling the texture and surface morphology of the Cr underlayer;
   - To investigate the influence of the Cr underlayer on the structure and magnetic properties of $SmCo_5$ films;
   - Under the optimal conditions, to study the influence of MgO single crystal substrates and glass substrates on the structure and magnetic properties of $SmCo_5$ films.
2. To explore the feasibility of the deposition of $SmCo_5$ thin films with perpendicular magnetic anisotropy and high out-of-plane coercivity on glass substrate with Cu underlayers (Chapter 4). In particular:
   - To find a seed layer able to improve the structure, surface morphology and thickness (thinner is better) of Cu underlayers;
   - To study the influence of the seed layer and the Cu underlayer on the structure and magnetic properties of $SmCo_5$ thin films.
3. To explore the feasibility of $SmCo_5$ thin films with perpendicular magnetic anisotropy and high out-of-plane coercivity on glass substrate with a Ni and/or

Ni-alloy underlayers (Chapter 5). In particular:

- To study the effects of the seed layer on the Ni underlayer;
- To study the influence of Ni and/or Ni-alloy underlayers on the structure and magnetic properties of $SmCo_5$ thin films
- To explore hard/soft double-layered films for perpendicular recording applications.

1.5 References

[1]. Hitachi Global Storage Technologies (http://www.hitachigst.com/hdd/hddpdf/tech/hdd_technology2003.pdf).

[2]. S. N. Piramanayagam and K. Srinivasan, J. Magn. Magn. Mater. **321**, 485 (2009).

[3]. A. Moser, K. Takano, D. T. Margulies, M. Albrecht, Y. Sonobe,Y. Ikeda, S. Sun and E. E. Fullerton, J. Phys. D: Appl. Phys. **35**, R157 (2002).

[4]. E. E. Fullerton, D. T. Margulies, M. E. Schabes, M. Carey, B. Gurney, A. Moser, M. Best, G. Zeltzer, K. Rubin, and H. Rosen, Appl. Phys. Lett. **77**, 3806 (2000).

[5]. E. N. Abarra, A. Inamota, H. Sato, I. Okamoto, and Y. Mizoshita, Appl. Phys. Lett. **77**, 2581 (2000).

[6]. K. Hono, B. Wong and D. E. Laughlin, J. Appl. Phys. **68**, 4734 (1990).

[7]. Y. C. Feng, D. E. Laughlin and D. N. Lambeth, J. Appl. Phys. **76**, 7311 (1994).

[8]. L. L. Lee, D. E. Laughlin and D. N. Lambeth, IEEE Trans. Magn. **34**, 1561 (1998).

[9]. S. Yoshimura, D. D. Djayaprawira, M. Mikami, Y. Takakuwa and M. Takahashi, IEEE Trans. Magn. **38**, 1958 (2002).

[10]. Y. Xu, J. P. Wang, Z. S. Shan, H. Jiang and C. T. Chong, J. Appl. Phys**. 88**, 7234 (2000).

[11]. F. Menzinger and A. Paoletti, Phys. Rev. **143**, 365 (1966).

[12]. G. Pattanaik, G. Zangari, and J. Weston, Appl. Phys. Lett. **89**, 112506 (2006).

[13]. B. Lu, T. Klemmer, G. Ju, K. Wierman, D. Weller, A. Roy, D. E. Laughlin, C. Chang and R. Ranjan, J. Appl. Phys. **91**, 8025 (2002).

[14]. T. P. Nolan, R. Sinclair, R. Ranjan, T. Yamashita, G. Tarnopolsky and W. Bennett, Mater. Res. Soc. Symp. Proc. **343**, 297 (1994).

[15]. "Landoldt–Börnstein" (New Series III/19a), Berlin: Springer (1970).

[16]. R. Wood, Y. Sonobe, J. Zhen and B. Wilson, J. Magn. Magn. Mater. **235**, 1 (2001).

[17]. H. J. Richter, J. Phys. D: Appl. Phys. **40**, R149 (2007).

[18]. R. Mukai, T. Uzumaki and A. Tanaka, J. Appl. Phys. **97**, 10N119 (2005).

[19]. H. Sato, T. Shimatsu, Y. Okazaki, O. Kitakami, S. Okamoto, H. Aoi, H. Uraoka and Y. Nakamura, IEEE Trans. Magn. **43**, 2106 (2007).

[20]. S. N. Piramanayagam, H. B. Zhao, J. H. Shi and C. H. Mah, Appl. Phys. Lett. **88**, 92506 (2006).

[21]. K. Hayashi, M. Hayakawa, H. Ohmori, A. Okabe and K. Aso, J. Appl. Phys. **67**, 5175 (1990).

[22]. J. Ariake, T. Chiba and N. Honda, IEEE Trans. Magn. **41**, 3142 (2005).

[23]. T. P. Nolan, J. D. Risner, S. D. Harkness IV, E. Girt, S. Z. Wu and R. Sinclair IEEE Trans. Magn. Mag. **43**, 639 (2007).

[24]. E. M. T. Velu, S. Malhotra, G. Bertero and D. Wachenschwanz, IEEE Trans. Magn. **39**, 668 (2003).

[25]. P. F. Carcia, A. D. Meinhaldt and A. Suna, Appl. Phys. Lett. **47**, 178 (1985).

[26]. B. M. Lairson, J. Perez and C. Baldwin, Appl. Phys. Lett., **64**, 2891 (1994).

[27]. W. B. Zeper, F. J. A. M. Greidanus and P.F. Carcia, IEEE Trans. Magn. **25**, 3764 (1989).

[28]. F. J. den Broeder, H. C. Donkersloot, H. J. G. Draaisma, and W. J. M. de Jonge, J. Appl. Phys. **61**, 4317 (1987).

[29]. W. Peng, R. H. Victora and J. H. Judy, IEEE Trans. Magn. **37**, 1577 (2001).

[30]. R. Yoshino, T. Nagaoka, R. Terasaki and C. Baldwin, J. Magn. Soc. Jpn. **18-S1**, 103 (1994).

[31]. R. H. Victora and X. Shen, IEEE Trans. Magn. **41**, 537 (2005).

[32]. R. H. Victora and X. Shen, IEEE Trans. Magn. **41**, 2828 (2005).

[33]. J. P. Wang, W. K. Shen, J. M. Bai, R. H. Victora, J. H. Judy and W. L. Song, Appl. Phys. Lett. **86**, 142504 (2005).

[34]. D. Suess, T. Schrefl, S. Fahler, M. Kirschner, G. Hrcac, F. Dorfbauer and J. Fidler, Appl. Phys. Lett. **87**, 012504 (2005).

[35]. D. Suess, T. Schrefl, R. Dittrich, M. Kirschner, F. Dorfbauer, G. Hrkac and J. Fidler, J. Magn. Magn. Mater. **290–291**, 551 (2005).

[36]. D. Suess, T. Schrefl, M. Kirschner, G. Hrkac, F. Dorfbauer, O. Ertl and J. Fidler, IEEE Trans. Magn. **41**, 3166 (2005).

[37]. D. Suess, Appl. Phys. Lett. **89**, 113105 (2006).

[38]. S. Okamoto, O. Kitakami, N. Kikuchi, T. Miyazaki, Y. Shimada, and T. Chiang., J. Phys.: Condens. Matter **16**, 2109 (2004).

[39]. H. J. Richter and A. Dobin, J. Appl. Phys. **99**, 08Q905 (2006).

[40]. K. Yu. Guslienko, O. Chubykalo-Fesenko, O, Mryasov, R. W. Chantrell and D. Weller, Phys. Rev. B. **70**, 104405 (2004).

[41]. F. Garcia-Sanchez, O. Chubykalo-Fesenko, O. Mryasov, R. W. Chantrell and K. Yu. Guslienko, Appl. Phys. Lett. **87**, 122501 (2005).

[42]. A. Yu. Dobin and H. J. Richter, Appl. Phys. Lett. **89**, 062512 (2006).

[43]. J. U Theile, S. Maat, J. L. Robertson and E. E. Fullerton, IEEE Trans. Magn. **40**, 2537 (2004).

[44]. J. J. M. Ruigrok, R. Coehoorn, S. R. Cumpson and H. W. Kesteren, J. Appl. Phys. **87**, 5398 (2000).

[45]. H. J. Richer and S. D. Harkness IV, MRS Bulletin **31**, 384 (2006).

[46]. B. D. Terris and T. Thomson, J. Phys. D: Appl. Phys. **38**, R199 (2005).

[47]. C. A. Ross, Annu. Rev. Mater. Res. **31**, 203 (2001).

[48]. R. M. H. New, R. F. W. Pease and R. L. White, J. Magn. Magn. Mater. **155**, 140 (1996).

[49]. M. Todorovic, S. Schultz, J. Wong and A. Scherrer, Appl. Phys. Lett. **74**, 2516 (1999).

[50]. G. F. Hughes, IEEE Trans. Magn. **36**, 521 (2000).

[51]. L. Néel, Ann. Geophys. **5**, 99 (1949).

[52]. W. F. Jr. Brown, IEEE Trans. Magn. **15**, 1196 (1979).

[53]. S. H. Charap, P. L. Lu and Y. He, IEEE Trans. Magn. **33**, 978 (1997).

[54]. D. Weller and A. Moster, IEEE Trans. Magn. **35**, 4423 (1999).

[55]. D. Weller, A. Moser, L. Folks, M. E. Best, W. Lee, M. F. Toney, M. Schwickert, J. U. Thiele and M. F. Doerner, IEEE Trans. Magn. **36**, 10 (2000).

[56]. J. Sayama, K. Mizutani, T. Asahi, J. Ariake, K. Ouchi, S. Matsunuma, T. Osaka, J. Magn. Magn. Mater. **287**, 239 (2005).

[57]. "Advanced Magnetic Nanostructure", edited by D. Sellmyer and R. Skomski, Springer NY (2006).

[58]. S. Nagasaki, M. Hirabayashi and Nigen Gokin Jotaizushu, AGNE Gijutsu Center, Tokyo, (2001).

[59]. S. Chikazumi, "Physics of Ferromagnetism", Oxford University Press, New York (1997).

[60]. K. J. Strnat, "Ferromagnetic Materials", edited by E. P. Wohlfarth and K. H. J. Buschow (North-Holland, Amsterdam), Vol. **4**, Chap. 2, (1988).

[61]. J. D. Livingston, AIP Conf. Proc. **10**, 643 (1973).

[62]. D. Givord, P. Tenaud and T. Viadieu, J. Magn. Magn. Mater. **72**, 247 (1988).

[63]. A. Singh, V. Neu, S. Fähler, K. Nenkov, L. Schultz and B. Holzapfel, Phys. Rev. B. **77**, 104443 (2008).

[64]. E. E. Fullerton, J. S. Jiang, C. Rehm, C. H. Sowers, S. D. Bader, J. B. Patel and X. Z. Wu, Appl. Phys. Lett. **71**, 1579 (1997).

[65]. A. Singh, V. Neu, R. Tamm, K. Subba Rao, S. Fähler, W. Skrotzki, L. Schultz and B. Holzapfel, Appl. Phys. Lett. **87**, 072505 (2005).

[66]. A. Singh, R. Tamm, V. Neu, S. Fähler, W. Skrozki, L. Schultz and B. Holzapfel, J. Appl. Phys. **99**, 08E917 (2006).

[67]. M. Benaissa, K. M. Krishnan, E. E. Fullerton and J. S. Jiang, IEEE Trans. Magn. **34**, 1204 (1998).

[68]. V. Geiss, E. Kneller and A. Nest, Appl. Phys. **A-27**, 79 (1982).

[69]. U. Kullmann, E. Koester and C. Dorsch, IEEE Trans. Magn. **20**, 420 (1984).

[70]. S. H. Aly, T. D. Cheung, L. Wickramasekara and F. J. Cadieu, J. Appl. Phys. **57**, 2147 (1985).

[71]. E. M. T. Velu and D.N. Lambeth, J. Appl. Phys. **69**, 5175 (1991).

[72]. E. M. T. Velu and D.N. Lambeth, IEEE Trans. Magn. **28**, 3249 (1992).

[73]. Y. Liu, B.W. Robertson, Z. S. Shan, S. Malhotra, M. J. Yu, S. K. Renukunta, S. H. Liou and D. J. Sellmyer, IEEE Trans. Magn. **30**, 4035 (1994).

[74]. Y. Liu, D. J. Sellmyer, B. W. Robertson, Z. S. Shan and S. H. Liou, IEEE Trans. Magn. **31**, 2740 (1995).

[75]. Y. Liu, D. J. Sellmyer and B. W. Robertson, J. Appl. Phys. **79**, 5333 (1996).

[76]. S. S. Malhotra, Y. Liu, Z. S. Shan, S. H. Liou, D. C. Stafford and D. J. Sellmyer, J. Appl. Phys. **79**, 5958 (1996).

[77]. S. Takei, Y. Otagiri, A. Morisako and M. Matsumoto, J. Appl. Phys. **85**, 6145

(1999).

[78]. S. Takei, A. Morisako and M. Matsumoto, J. Appl. Phys. **87**, 6968 (2000).

[79]. J. Zhang, Y. K. Takahashi, R. Gopalan and K. Hono, J. Magn. Magn. Mater. **310**, 1 (2007).

[80]. J. Sayama, T. Asahi, K. Mizutani, and T. Osaka, J. Phys. D: Appl. Phys. **37**, L1–L4 (2004).

[81]. S. Takei, A. Morisako and M. Matsumoto, J. Magn. Magn. Mater. **272–276**, 1703 (2004).

[82]. J. Sayama, K. Mizutani, T. Asahi and T. Osaka, Appl. Phys. Lett. **85**, 5640 (2004).

[83]. I. Kato, S. Takei, X. X. Liu and A. Morisako, IEEE Trans. Magn. **42**, 2366 (2006).

[84]. Y. K. Takahashi, T. Ohkubo and K. Hono, J. Appl. Phys. **100**, 053913 (2006).

[85]. J. Sayama, K. Mizutani, T. Asahi, J. Ariake, K. Ouchi, T. Osaka, J. Magn. Magn. Mater. **301**, 271 (2006)

[86]. A. Morisako and X. Liu, J. Magn. Magn. Mater. **304**, 46 (2006).

[87]. X. Liu, H. Zhao, Y. Kubota and J. P. Wang, J. Phys. D: Appl. Phys. **41**, 232002 (2008).

2 Chapter II Experimental techniques

In this project, I used the sputtering technique for the sample fabrication, Rutherford Backscattering Spectroscopy (RBS) for the examination of composition, X-ray diffraction (XRD) for the study of crystallographic structure, transmission electron microscopy (TEM) for the analysis of microstructure, atomic force microscopy (AFM) for the study of the surface topography, as well as vibrating sample magnetometer (VSM) and superconducting Quantum Interference Device (SQUID) for the measurement of magnetic properties. The experimental details are described in this chapter.

2.1 Sputtering techniques

In recent years, sputtering technique is widely used to fabricate thin films in many industries, such as semiconductor, optics and rigid disk magnetic recording, because it possesses unique advantages. If a material can be volatilized by sputtering, a uniform film can be made over a large area and compounds can be relatively stoichiometrical [1]. Independent controlling parameters such as deposition power, deposition temperature and working gas pressure makes this technique very versatile. The crystallographic structure and microstructure of thin films can be well controlled by adjusting the above parameters. Hence the desired properties of thin films can be effectively obtained.

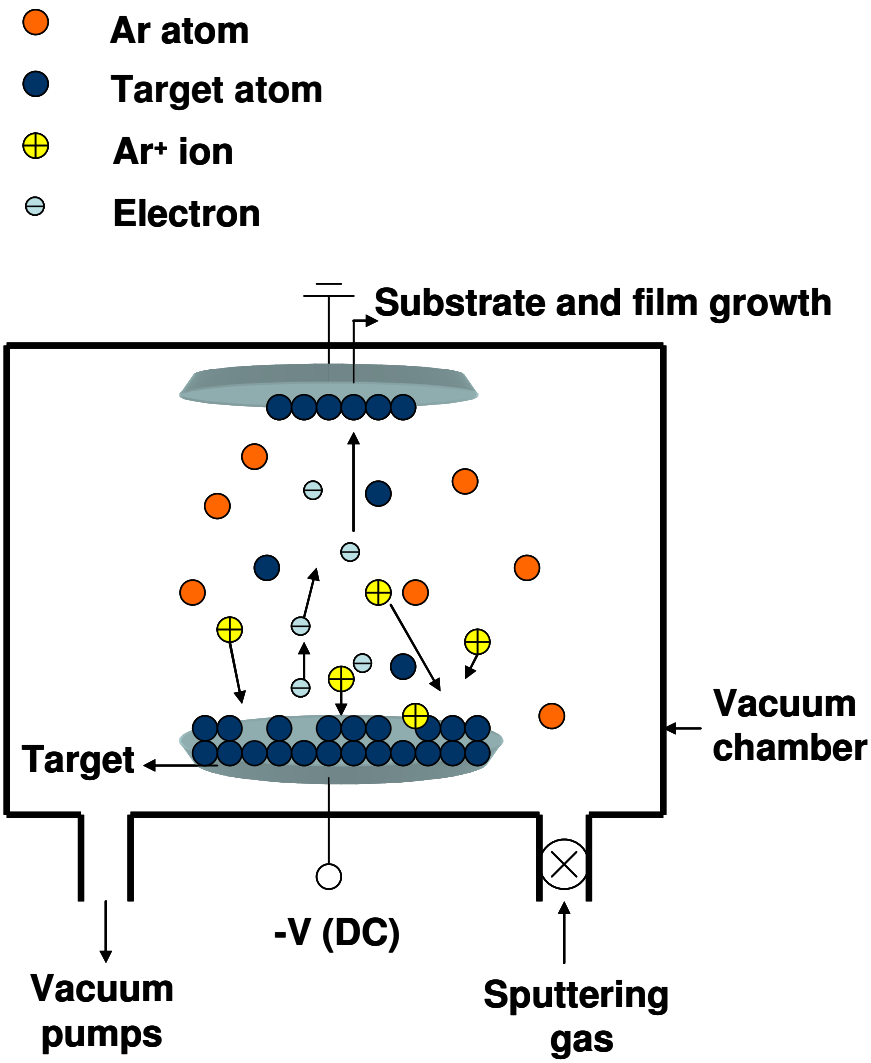

Fig. 2.1. Schematic diagram of DC sputtering system.

Sputtering is a physical vapour process whereby atoms in a solid target are ejected out due to bombardment by energetic ions. As illustrated in Fig. 2.1, a sputtering system consists of targets, a substrate and a vacuum system. The target is usually bonded to a water-cooled Cu backing plate to dissipate the heat generated by bombardment. The target is connected to a negative terminal of a direct current (DC) (for conductive materials) or an alternating current (AC) (for insulative materials) power supply as a cathode. The substrate is placed opposite to the target and is

grounded as an anode. The chamber is filled with inert gas to a pressure of few mTorr. With adequate voltage across the electrodes, the inert gas will break down into a plasma discharge. The positive inert gas ions, typically Ar^+, are accelerated towards the target and collide with the atoms in the target to sputter the neutral target atoms through momentum transfer. These atoms go through the plasma and deposit on the substrate. In addition, as part of this collision, secondary electrons are emitted from the target surface. These electrons are accelerated back to collide with inert gas atoms to cause a further ionization of inert gas to sustain the discharge.

Magnetron sputtering is a kind of sputtering techniques. A ring magnet is placed under the target so that the secondary electrons are trapped in cycloids and circulate over the target surface. More secondary electrons over the target surface result in higher ionization possibility of inert gas and higher deposition rate. Nowadays, more than 90% of sputtering systems use magnetron sputtering in the market. It offers thin, uniform and cost-effective films.

In the present study, all films are prepared by a home-designed DC magnetron sputtering system located in Data Storage Institute (DSI), Singapore. There is a total of four target positions (cathodes) and one substrate holder (anode) which is situated above the targets housed in a vacuum chamber. The target used in this system is a plate of raw material with a diameter of 3 inch and a thickness of 3 cm. The substrate holder is rotating at 50 revolutions per minute (rpm) during the sputtering process to ensure the uniformity of deposited films. The base pressure of the vacuum chamber is 2×10^{-7} Torr or below. The pumping system consists of a mechanical pump and a cryopump. The chamber is filled with 99.999% pure Ar gas at a pressure of 3 mTorr as the sputtering gas. The sputtering rate is adjusted through the sputtering power. The composition of composite film is controlled by adjusting sputtering rates of

respective elemental targets (co-sputtering). The film thickness is controlled by sputtering time. An *in situ* heating system can heat substrate up to 700ºC. The substrates are loaded in a load lock system which is adapted to transfer the substrate to the main chamber without opening the main chamber. When targets are installed, before film deposition, a pre-sputtering is normally carried out for about 15 minutes to remove impurities from the target surface. The aim of this project is to deposit *in situ* crystallized $SmCo_5$ thin films with desired magnetic properties for magnetic recording media in this system.

2.2 Structure and microstructure characterization

2.2.1 Rutherford Backscattering Spectroscopy (RBS)

In this project, the composition of the deposited films is estimated by RBS. RBS is a highly quantitative elemental-analysis technique [1]. In RBS, a beam of He^{++} (alpha particles) impinges on a sample with energy high enough to scatter particles from the sample's atomic nuclei in binary Coulomb collisions unscreened by the surrounding electron clouds. During the bombardment, the alpha particles transfer a part of their kinetic energy to the target particles. According to the kinetic energy remaining in the backscattered beam and the scattering angle, the target atomic mass can be easily calculated.

The energy remaining in the alpha particle (E_r) is given by:

$$E_r = k \bullet E_0 \qquad \text{Eq. 2.1}$$

where, E_0 is the energy of incident particle and k is the kinetic factor, which is given by:

$$k = \left(\frac{m_1 \cos\theta_1 \pm \sqrt{m_2^2 - m_1^2 (\sin\theta_1)^2}}{m_1 + m_2}\right)^2 \qquad \text{Eq. 2.2}$$

where, m_1 and m_2 are the masses of the incident alpha particle and the target atom, respectively, and θ is the scattering angle of the projectile.

Heavier elements withdraw less energy, thus the backscattering beam possesses higher energy. The substrate elements generate a background signal in the energy spectrum. Because of the stopping effect, the signal from substrates extends all the way from its energy to zero [2]. Therefore, a major element in the substrate should be lighter than one in the film to obtain good signal-to-noise ratio. In the present study, RBS was used to calibrate the compositions of Sm-Co magnetic layers and Ni-W underlayers. The calibration samples are prepared on Si or SiO_2 substrates.

2.2.2 X-ray diffraction (XRD)

XRD is a major tool for the study of crystallographic structure. XRD is used in this study to identify the crystallographic phases of thin films, to calculate the lattice constants, to investigate the epitaxial relationship of multilayer films and to check the preferred orientation of polycrystalline films. XRD has the merits of being nondestructive and structural study from a relatively large area. The physical principle of XRD is based on the Brag's law [3]:

$$2d\sin\theta = n\lambda \qquad \text{Eq. 2.3}$$

as shown in Fig. 2.2, where n is the integer number corresponding to the order of diffraction, λ is the wavelength of the incident x-ray, d is the inter-planar spacing of the reflecting (or diffracting) plane, and θ is the angle of the incidence relative to the reflecting plane.

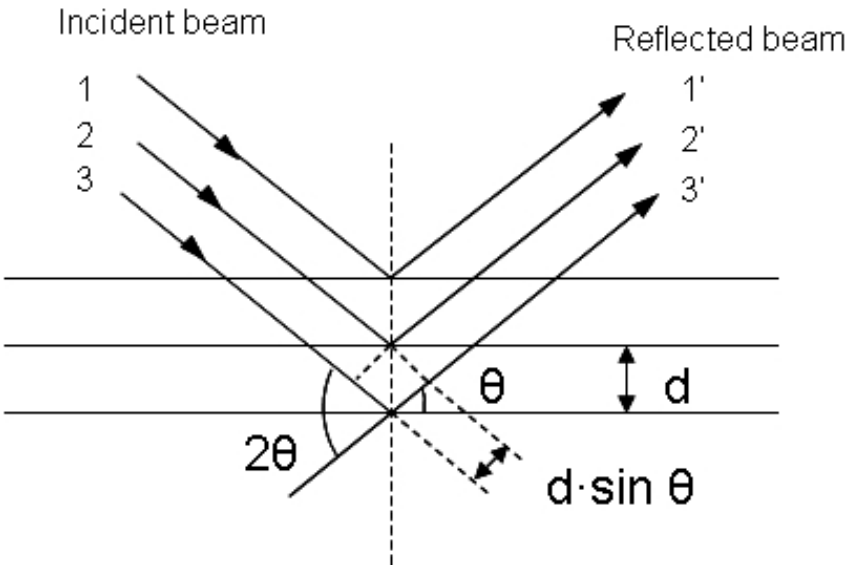

Fig. 2.2. Schematic illustration of X-ray diffraction.

For a polycrystalline powder material, if the individual crystal is less than 100 nm in size, the crystallite size along the film normal direction can be estimated using the Scherer equation [4]:

$$L = \frac{\kappa\lambda}{B\cos\theta} \qquad \text{Eq. 2.4}$$

where, κ is particle shape factor (for spherical particles, κ =0.9), B is full width half maximum (radians) and L is diameter of the crystallites (Å). In order to remove the instrument broadening influence to more accurately determine crystal size, Warren's method [5, 6] is used:

$$B^2 = B_M^2 - B_S^2 \qquad \text{Eq. 2.5}$$

where, B is the true line broadening, B_M is the measured breadth at half-maximum intensity, and B_S is the peak width of a standard material, usually silicon.

In the present study, a Philips X'pert X-ray diffractometer is employed. The instrument broadening (B_s) is 0.06º. X-rays are generated by a Cu cathode (K_α radiation with λ = 1.54056 Å). The **θ - 2θ scan** is the most common way to collect

the crystallographic information. In this method, the X-ray tube is stationary, the sample turns by the angle of θ and the detector turns by the angle of 2θ simultaneously. It detects the lattice planes of the crystal parallel to the film plane. According to the θ positions of the diffraction peak, crystal phases can be identified according to the standard database from the Joint Committee on Powdered Diffraction Standard (JCPDS). Moreover, by comparing the relative peak intensities from various planes with those from a randomly oriented reference sample consisting of the powdered bulk material, a qualitative evaluation of preferred crystal plane orientations (texture) can be made. The quality of texture parallel to the film plane can be further examined by the full-width at half-maximum ($\Delta\theta_{50}$) of the **rocking curve (ω scan)**. In this method, the film is tilted within a certain scan range (usually 10º) while the diffractometer is fixed on a particular Bragg peak in 2θ. When the thickness of the film is very small (e.g. <10nm), the θ - 2θ scan can be noisy. **Glancing angle scan** is useful in this case. When the glancing angle is small enough, only the few tens of nm beneath the film surface are probed, thus signal from substrate can be avoided. This method detects the atomic planes of the crystal unparallel to the film plane.

2.2.3 Transmission electron microscopy (TEM)

TEM is another major tool for microstructural analysis in this thesis. The TEM observation is performed using either JOEL 3010 or JOEL 2010 with an operating voltage of 300 kV and 200 kV, respectively. Both TEMs have an energy dispersive analysis by X-ray (EDAX) attachment, which can analyze the composition of film. A parallel beam of electrons passes through the sample, where part of the beam is scattered by atoms to different directions. The diffracted electron beam is

brought into focus in the back focal plane of objective lens, forming a two dimensional array of spots corresponding to a particular set of plane for a single crystal. For polycrystalline samples, ring patterns are observed. From diffraction pattern, the inter-planer spacing can be derived using the relation:

$$d_{hkl}R=L\lambda \qquad \text{Eq. 2.6}$$

where, d_{hkl} is the inter-planer spacing for a particular set of reflecting planes {hkl}, R is the radius of a particular diffraction ring, λ is the wavelength of the electron beam and L is the distance between the sample and the back focal plane. The product λL is known as the camera constant.

Three kinds of images can be obtained in TEM with different mechanisms of image formation: bright-field, dark-field and high-resolution image. These three kinds of images are formed by selecting electron beams using suitable objective apertures for image information [7].

In bright-field (BF) imaging, an aperture is placed in the back focal plane of the objective lens that allows only the electrons in the transmitted beam to pass and contribute to the resulting bright field image as shown in Fig. 2.3.

In dark field (DF) imaging, the image occurs when the objective aperture is positioned off-axis from the transmitted beam in order to allow only a diffracted beam to pass as shown in Fig. 2.4. If a sample is crystalline, many electrons will undergo elastic scattering from the various (hkl) planes. This scattering produces many diffracted beams. If any one of these diffracted beams is allowed to pass through the objective aperture, an image can be obtained. This image is known as a dark-field image. Dark-field images are particularly useful in examining grain size in a crystalline phase.

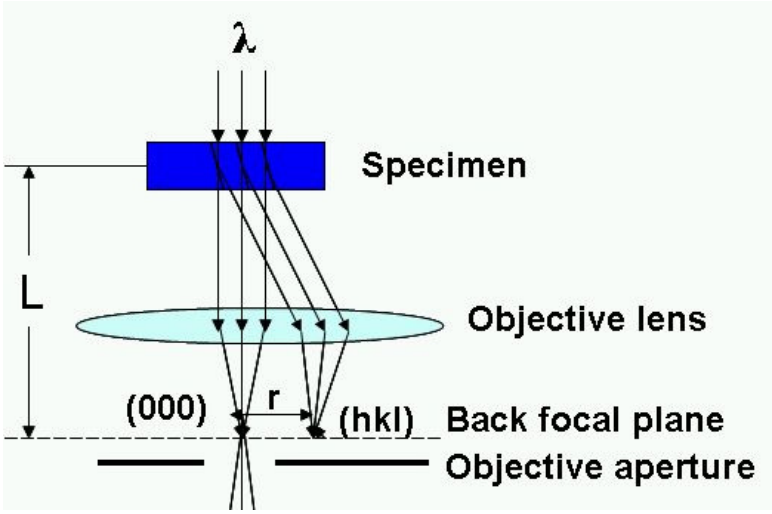

Fig. 2.3. Schematic diagram for TEM bright field imaging.

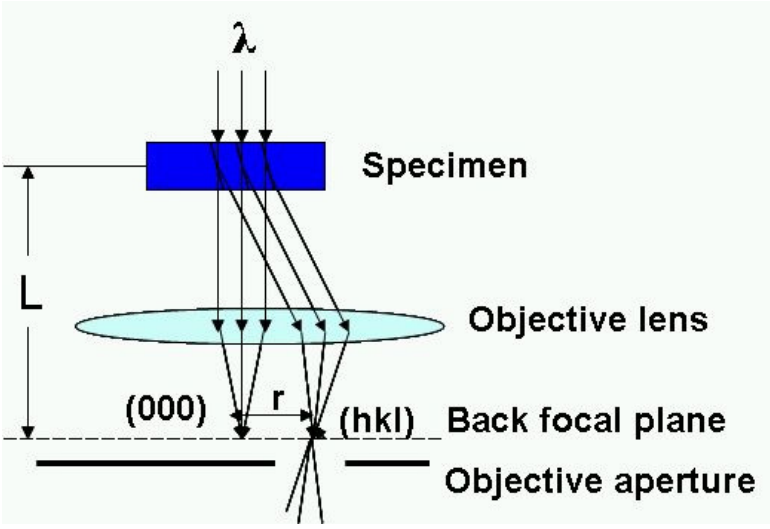

Fig. 2.4. Schematic diagram for TEM dark field imaging.

In high-resolution imaging (HRTEM), a large objective aperture is used which allows both diffracted and directly transmitted beams to pass. The image is formed by the interference of the diffracted beams with the directly transmitted beam. In the HRTEM image, bright and dark lines correspond to columns or planes of atoms, with

spacings that correspond to the crystal structures of the materials. Generally, it is more difficult to obtain a clear HRTEM image compared with BF and DF images. The samples for HRTEM imaging must be very thin (<10 nm) in order to permit more electrons to go through, typically 500 to 2000 electrons per square Ångstrom [8]. Correct lens defocus, no image astigmatism and precise incident beam alignment are required.

Good TEM images depend on well prepared samples. The thin films are prepared in both plan-view and cross-sectional geometries in the present study. Image of plan-view geometry straightforwardly shows the microstructure of the top film. On the other hand, image of cross-sectional geometry is necessary when the features of interest distributed throughout the depth of the sample because of its multi-layered structure.

For preparation of plan-view specimens, the material of interest is first cut into a small piece of around 3 mm×3 mm. This small piece is stuck to the sample holder with wax for mechanical polishing with the film side facing down. After the film is polished to be thin enough, a copper ring is glued to the specimen. The glue is cured at a temperature of about 140ºC for about 20 minutes. Meanwhile the wax between sample and sample holder is melt. The specimen is taken off the holder and is mounted onto an ion milling stage. Then the specimen is ion-beam milled at low beam energies. After the ion-milling process, a hole is formed in the middle of the specimen. The film around the hole is thin enough to permit the transmission of electrons.

The Bravman-Sinclair method [9] is used to prepare cross-sectional specimens. First, the specimen of interest is cut into a small piece of around 2 mm×4 mm. Then the sample is glued with the film side face-to-face onto additional silicon wafers. The

glue is cured at a temperature of about 140ºC for about 30 minutes. This stack is stuck on one side to the sample holder with wax. The stack is polished on one side to a thickness of about 500μm thick and to a mirror shining extent. Then the sample is heated until the wax melt. The stack is turned and the other side of the stack is stuck to sample holder. After the other side is polished until it is about 10μm thick, a copper ring is glued to the slice of the stack, and ion milling is used to further thin the film until a tiny hole is formed. The area close to the edge of the hole is thin enough for electrons to be transmitted.

2.2.4 Atomic force microscopy (AFM)

AFM is one of the most powerful tools for determining the surface topography of specimens at sub-nanometer resolution [10]. It is developed from the scanning tunneling microscope (STMS) which uses tunneling current to monitor the separation between a probe bearing a conductive tip and the specimen. The tunneling current varies exponentially with the tip-sample spacing. A feedback loop adjusts the height of the probe in order to maintain the same current allowing the tip to image the topology of the sample. AFM overcomes the biggest shortcoming of STM which requires electrically conductive samples. Instead of measuring a current, AFM is based on atomic forces such as Van der Waals forces. A sharp tip mounted at the end of a soft cantilever spring interacts with the surface of the sample [11]. The Wan der Waals interaction between the tip and the surface deflects the cantilever. This is sensed by a laser beam reflected from the top surface of the cantilever into a photodiode array. The generated electric signal is sent to a feedback loop which monitors and controls the cantilever force. Finally the force-position information can be converted into an image.

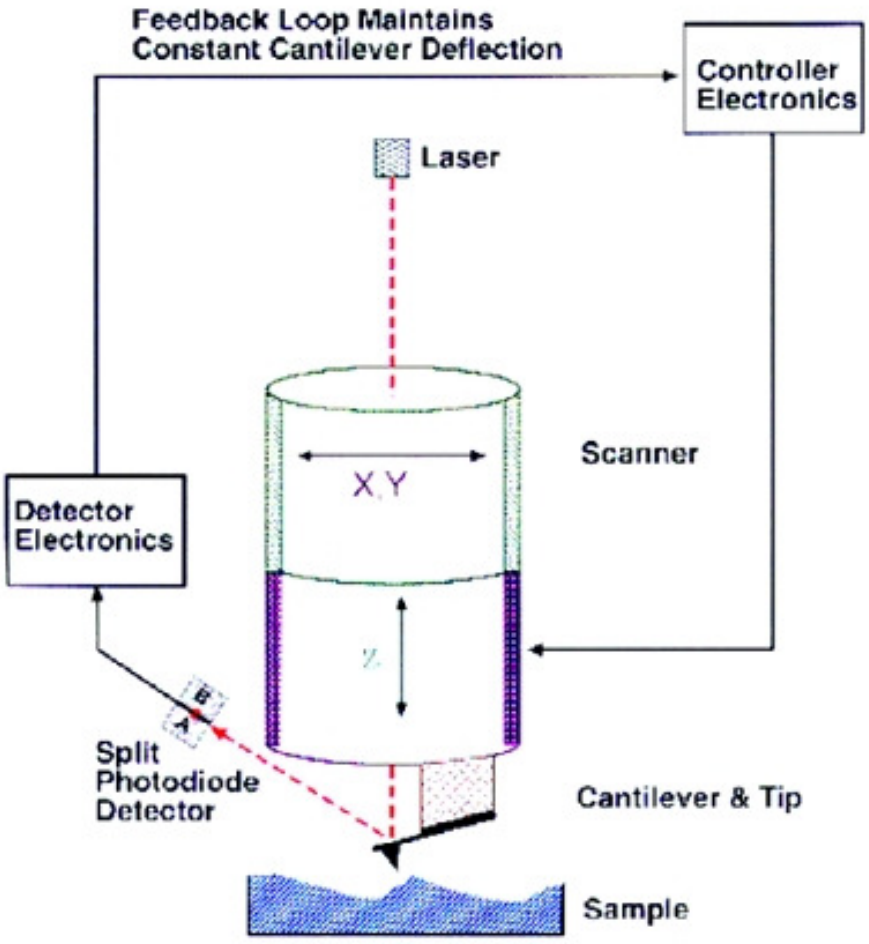

Fig. 2.5. Schematic diagram of an AFM system [12].

There are three imaging modes: contact mode, tapping (semi-contact) mode and non-contact mode. In contact mode, the tip actually makes physical contact with the surface and the cantilever drags across the sample surface. The feedback system adjusts the position of the probe in order to maintain a constant deflection of the cantilever. In tapping mode, the cantilever oscillates up and down at near its resonance frequency. When the tip gets closer to the surface, it “taps” the surface and the amplitude of oscillation decreases. The feedback system adjusts the position of the cantilever in order to maintain a constant oscillation amplitude. The schematic illustration of tapping mode AFM is shown in Fig. 2.5. This is preferable over the

contact mode as it eliminates shear forces, thus it is less damaging for the sample surface and the tip, and higher image resolution is obtained. In non-contact mode, the cantilever oscillates at a frequency slightly above its resonance frequency. When the tip gets closer to the surface, the resonance frequency of the cantilever decreases, the feedback system adjusts the position of the cantilever in order to maintain a constant oscillation amplitude. This latter mode is used for "soft" or liquid samples. In the present study, a DI multimode AFM is employed and the most widely used tapping mode is chosen.

2.2.5 Profilometer

The thicknesses of films are measured using a profilometer. The profilometer measures the surface topography with a stylus that is dragged across the sample surface with a constant load. The fluctuations of the stylus height are recorded as a function of position. An appropriate software calculates surface parameters such as peak-to-valley height and average roughness. In the present study, a KLA-Tencor P-12EX Disk Profiler was employed. It scans with a stationary stylus and a moving sample stage. The scan speed can be controlled from 1 um/sec to 25 mm/sec. The error of height measurement is better than 1 nm for films with thicknesses below 200 nm.

2.3 Magnetic properties characterization

2.3.1 Vibrating sample magnetometer (VSM)

VSM is widely used for magnetic properties measurement. The physical principle of VSM is based on the Faraday's law of electromagnetic induction, which states that the voltage V(t) induced in an electrical circuit is proportional to the rate

of change of magnetic flux $d\phi/dt$ through the circuit.

$$V(t) = - C \cdot d\phi/dt \qquad \text{Eq. 2.7}$$

A typical VSM set up is shown in Fig. 2.6, the sample is suspended on a non-magnetic rod which vibrates vertically at a frequency of 72 Hz. The sample is placed in a magnetic field which is usually created by two electromagnets. As the magnetized sample oscillates in the magnetic field, the magnetic flux through the pick-up coil changes which induces an electrical signal in the coils. The induced AC voltage is proportional to the magnetic moment of the sample at the applied magnetic field. The frequency and amplitude of the vertical vibration are maintained constant by a capacitor (reference signal generator). The magnetic moment of the sample is extracted, by feeding the signals from the pick-up coils and the reference signal into a demodulator.

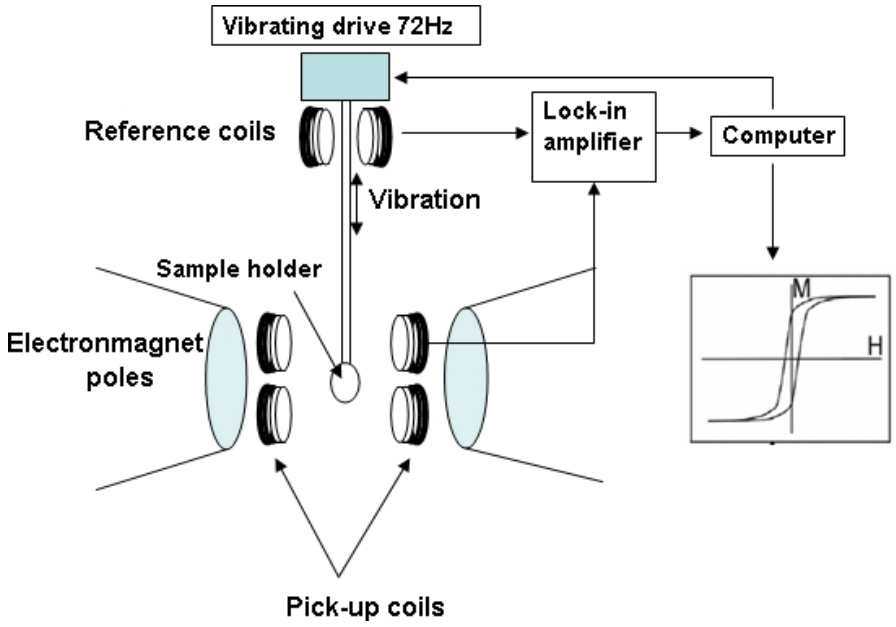

Fig. 2.6. Schematic diagram of a VSM system.

In this study, a Lakeshore 7400 VSM with a maximum applied field of 20 kOe

and a DMS model 10 VSM with a maximum applied field of 29 kOe are employed. All the samples are carefully cut in a size of 5×5 mm by a diamond cutter and are measured at room temperature. Before VSM measurement, first the sample holder is adjusted to make sure it is at the middle of the magnetic field; second a standard 5×5 mm Ni foil is used to calibrate the magnetic moment of the equipment. Finally a sample is tied to the sample holder and the measurements are taken according to the programmed settings.

2.3.2 Superconducting Quantum Interference Device (SQUID)

SQUID is a very sensitive magnetometer based on superconducting loops containing Josephson junctions. In 1911 H. K. Onnes discovered superconductivity in certain materials at very low temperature. The phenomenon was explained successfully by Bardeen, Cooper and Schrieffer (BCS theory). In 1956 Cooper explained a process by which two electrons near the Fermi level could couple to form an effective new particle, even under a very weak attractive force. The superconductivity is due to the Cooper pair transportation in a circuit. If two superconducting regions are kept isolated from each other by a very thin non-superconducting material, there will be a tunneling current across the gap. The tunneling of the electron-pairs across the gap carrying a superconducting current was predicted by Josephson [13].

In the present study, a superconducting quantum interference device (SQUID, MPMS, Quantum design, USA) with a maximum applied field of 50 kOe is used for measurement of $SmCo_5$ thin films with in-plane anisotropy. The samples are cut to 0.5×0.5 cm. A special straw provided by Quantum Design is used as a sample holder.

Before measurement, the magnet is reset to eliminate the remnant magnetic field trapped in superconducting coil. Then a sample is put into the straw and the measurements are taken according to the programmed settings.

2.3.3 Magnetic characterization

Various magnetic curves including hysteresis loop, angular dependence of coercivity, isothermal remanence (IRM) and DC demagnetization (DCD) remanence curves can be obtained by VSM and SQUID. The magnetization is obtained by $M=m/V$, where M is the magnetization of the film, m is the measured moment of the film and V is the volume of the film.

For **hysteresis loop measurement**, a strong magnetic field is applied to saturate sample along the applied field direction. Then the field is decreased step by step and the magnetization is measured at each step. By plotting the applied magnetic field (H) versus magnetization (M), a hysteresis loop is obtained. A typical hysteresis loop is shown in Fig. 2.7. The saturation magnetization M_s is reached when the external field is large enough to saturate the magnet. Even when the external field is removed, the magnet will retain some magnetization which is called remanent magnetization M_r. The reverse field needed to restore M to zero is called intrinsic coercive field ${}_iH_c$. ${}_iH_c$ is a good measure of the resistance of magnetising a material. Other information that can be extracted from the hysteresis loop is the loop squareness which is defined as:

$$S=\frac{M_r}{M_s} \qquad \text{Eq. 2.8}$$

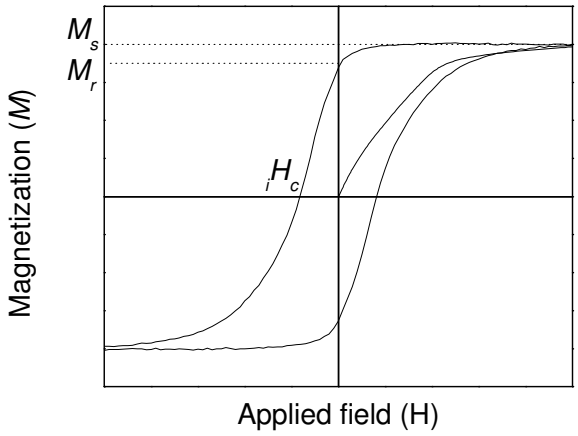

Fig. 2.7. Typical hysteresisi loop.

By rotating the sample, an external magnetic field can be applied at different directions to the film plane, thus **angular dependence of coercivity ($_iH_c$)** can be measured. Conventionally it is measured in the angular range of 90º. It determines the magnetization reversal mechanism of magnetic thin films. The reversal mechanism can be sorted into two kinds: (1) coherent rotation following the Stoner-Wohlfarth (S-W) theory; and (2) domain wall motion following the Kondorsky's model. Since the S-W model is based on the assumption of non-interacting magnetically isolated grains, the measurement of angular dependence coercivity can also be used to obtain the qualitative information about the grains isolation by comparing the experimental results with the S-W theory. According to the S-W theory, coercivity is defined by [14-17]:

$$\begin{cases} \dfrac{{}_iH_c(\psi)}{{}_iH_c(0)} = (\cos^{2/3}\psi + \sin^{2/3}\psi)^{-3/2},\ 0^o \le \psi \le 45^o & \text{Eq. 2.9} \\ \dfrac{{}_iH_c(\psi)}{{}_iH_c(0)} = \sin\psi\cos\psi,\ 45^o < \psi \le 90^o & \text{Eq. 2.10} \end{cases}$$

and, according to Kondorsky's model indicating the domain wall motion mechanism [18], coercivity is given by:

$$\frac{{}_iH_c(\psi)}{{}_iH_c(0)} = \frac{1}{\cos\psi},\ 0^o \le \psi \le 90^o \qquad \text{Eq. 2.11}$$

where, ${}_iH_c(\psi)$ is the intrinsic coercivity at an angle ψ and ψ the angle between the applied field and the easy axis direction. In this thesis, $SmCo_5$ thin films with the easy axis parallel to the film plane and perpendicular to the film plane were respectively studied. Correspondingly, ψ was defined with respect to the film plane or the film normal, respectively. The angular dependences of coercivity based on these two models are shown in Fig. 2.8.

For the **IRM curve measurement**, the sample needs to be demagnetized first. Then a positive field is applied to the sample, the applied field is removed and the remnant magnetization is measured as shown in Fig. 2.9 [19]. This cycle is repeated several times with progressively stronger applied fields until saturation is reached. The IRM curve is obtained by plotting the remnant magnetization versus the corresponding applied positive field. For the **DCD remanence curve measurement**, the sample is magnetized to saturation first. Then a reverse field is applied to the sample, the applied field is removed and the remnant magnetization is measured as shown in Fig. 2.9 [19]. This cycle is repeated several times with progressively increased reverse field until the negative saturation is reached. The DCD remanence curve is obtained by plotting the remnant magnetization versus the corresponding applied reverse field. The typical IRM curve and DCD remanence curve are shown in Fig. 2.10.

The Wohlfarth relation links these two remanence curves:

$$M_d(H) = M_{r,max} - 2M_r(H) \qquad \text{Eq. 2.12}$$

where, $M_d(H)$ is the DCD remanence and $M_r(H)$ is the IRM remanence. It is derived for an assembly of non-interacting single domain particles with uniaxial anisotropy where magnetization reversal occurs by coherent rotation.

The deviation ΔM_d has been widely used for the investigation of inter-granular interaction. It is defined as the deviation of measured DCD remanence $M_d(H)$ from the demagnetization remanence calculated from the Wohlfarth model [20, 21]:

$$\Delta M_d(H)=M_d(H) - [M_{r,max} - 2M_r(H)] \qquad \text{Eq. 2.13}$$

A plot of $\Delta M_d(H)$ verses applied field (H) gives a curve which could present the interactions. Two typical kinds of $\Delta M_d(H)$ curves are shown in Fig. 2.11 [22]. A positive $\Delta M_d(H)$ plot (curve 1 in Fig. 2.11) is usually associated with exchange coupled granular systems [23]. On the other hand, a negative $\Delta M(H)$ plot (curve 2 in Fig. 2.11) indicates interactions that attempt to demagnetize the material.

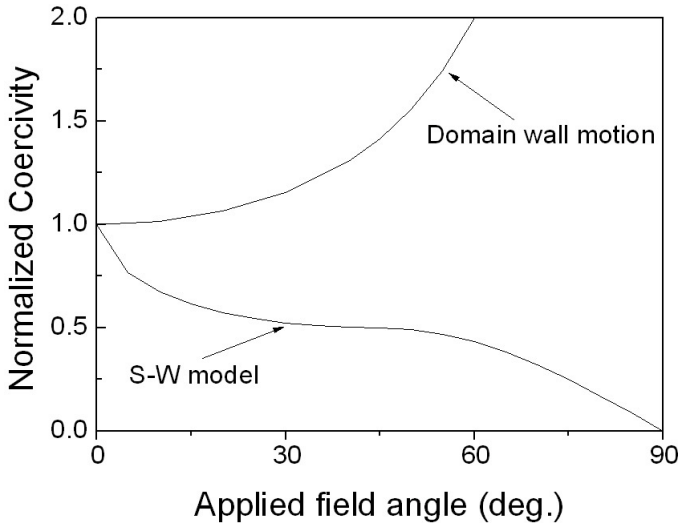

Fig. 2.8. Angular dependence of coercivity based on S-W model and domain wall motion model.

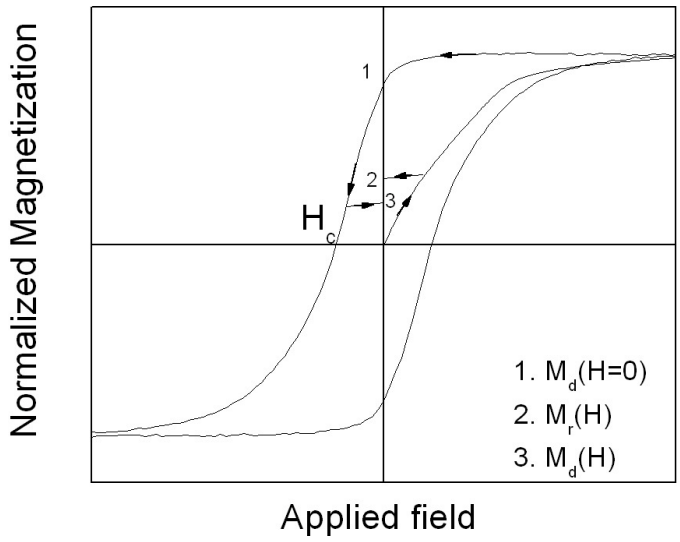

Fig. 2.9. Schematic explanation to measure the field dependant magnetisation remanence (M_r) and demagnetization remanence.

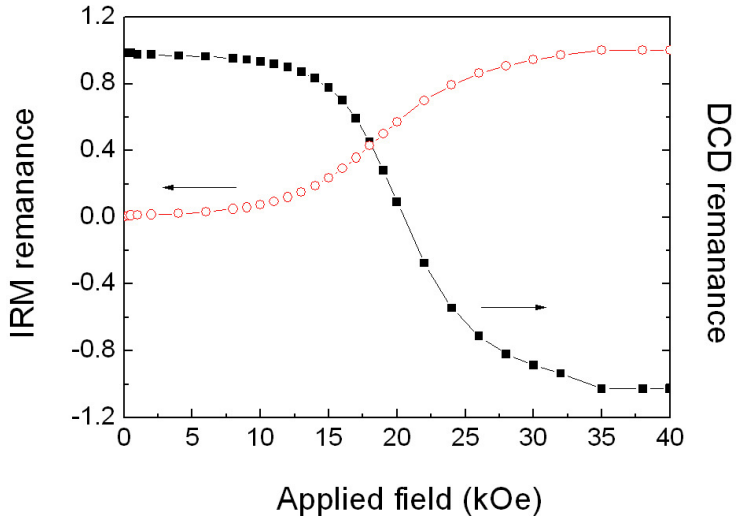

Fig. 2.10. Illustration of typical DCD and IRM curves. Hollow circle represents IRM curve and solid square represents DCD curve.

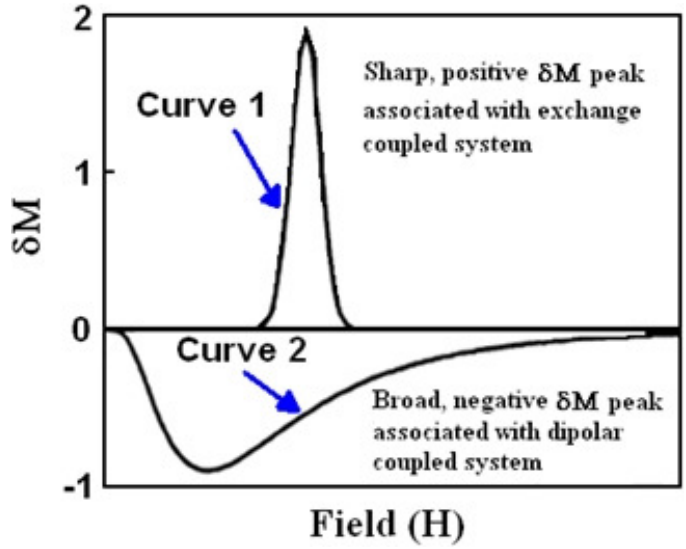

Fig. 2.11. Schematic δM curves illustrating different coupling regimes [22].

2.4 References

[1]. D. L. Smith, “Thin-film deposition principles and practice”, McGraw-Hill, Inc. (1995).

[2]. Oura, K., Lifshits, V.G., Saranin, A.A., Zotov, A.V., and Katayama, M., “Surface Science: An Introduction”, Berlin: Springer-Verlag (2003).

[3]. B. D. Cullity and S. R. Stock, “Elements of X-Ray Diffraction”, 3rd edition Prentice-Hall International (2001).

[4]. H. P. Klug and L. E. Alexander, “X-ray Diffraction Procedures for Polycrystalline and Amorphous Materials”, 2nd edition John wiley & Son Inc., New York (1974).

[5]. B. D. Cullity, “Elements of x-ray diffraction”, Addison-Wesley, New York (1978).

[6]. W. T. Sproull, “X-ray in practice”, Mc Grow-Hill, New York (1946).

[7]. D. B. Williams and C. B. Carter, “Transmission Electron Microscopy, A Textbook for Materials Science, Vol. 1: Basics”, Plenum Press, New York and London (1996).

[8]. D. Sellmyer and R. Skomski, “Advanced magnetic nanostructure”, Springer, New York (2006).

[9]. J. C. Bravman and R. Sinclair, J. Electron. Microsc. Tech. **1**, 53 (1984).

[10]. D. Sarid, “Scanning Force Microscopy with Applications to Electric, Magnetic and Atomic Forces”, Oxford University Press, New York (1991).

[11]. G. Binnig, C. F. Quate and C. Gerber, Phys. Rev. Lett. **56**, 930 (1986).

[12]. F. Giessibl, Reviews of Modern Physics **75**, 949 (2003).

[13]. B. D. Josephson, Rev. Mod. Phys. **46**, 251 (1974).

[14]. S. Chikazumi, “Physics of Ferromagnetism”, Oxford University Press, New York (1997).

[15]. R. C. O’Handley, “Modern Magnetic Materials-Principles and Applications”, John Wiley & Sons, Inc. (1999).

[16]. E. C. Stoner and E. P. Wohlfarth, Philos. Trans. London Ser. **A240**, 599 (1948).

[17]. E. C. Stoner and E. P. Wohlfarth, IEEE Trans. Magn. **27**, 3475 (1991).

[18]. E. Kondorsky, J. Phys. USSR. **2**, 161 (1940).

[19]. M. Fearon and R. W. Chantrell, J. Magn. Magn. Mater. **86**, 197 (1990).

[20]. R. A. McCurrie and P. Gaunt, Philos. Mag. **13**, 567 (1966).

[21]. P. E. Kellyand R. W. Chantrell, IEEE Trans. Magn. **25**, 3881 (1989).

[22]. T. Thomsony and K. O'Grady, J. Phys. D: Appl. Phys. **30**, 1566 (1997).

[23]. G. B. Ferguson and R. W. Chantrell, IEEE Trans. Magn. **25**, 3449 (1989).

3 Chapter III $SmCo_5$ thin films with longitudinal anisotropy grown on Cr underlayer

As discussed in Chapter 1, there is an epitaxial relationship between $SmCo_5$, Cr and MgO: $SmCo_5$ $(11\bar{2}0)$ <0001> // Cr (200) <011> // MgO (200) <010> as illustrated in Fig. 3.1. However, MgO single crystal substrate is rather expensive for industrial application. Hence, it is necessary to develop the technology for obtaining $SmCo_5$ thin films with longitudinal anisotropy and high in-plane coercivity grown on glass substrate at a relatively low temperature. Since glass substrates are amorphous and cannot induce some specific textures of $SmCo_5$, controlling the texture of the Cr underlayer by varying deposition conditions plays a critical role for the granular epitaxial growth (polycrystalline epitaxial growth) of $SmCo_5$. Therefore, in order to obtain the desired properties of $SmCo_5$ thin films, the key point is to understand the mechanism of the growth of Cr thin films and the conditions that would make Cr have the (200) texture.

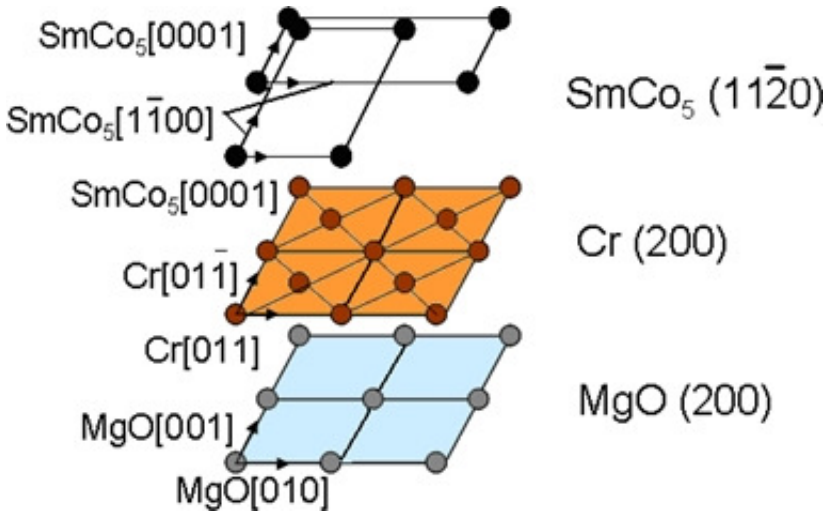

Fig. 3.1. Illustration of the epitaxial relationship: $SmCo_5$ $(11\bar{2}0)$ <0001> // Cr (200) <011> // MgO (200) <010>.

In this chapter, the effects of the deposition temperature, the thickness of the Cr underlayer, the thickness of the $SmCo_5$ layer and the composition of the Sm-Co

layer on the structure and the magnetic properties of $SmCo_5$ / Cr films on glass substrates were systematically investigated. Moreover, a comparison study was conducted concerning the structural and magnetic properties of $SmCo_5$ thin films with a Cr underlayer grown either on a glass substrate or on a MgO single crystal substrate.

3.1 Experimental methods

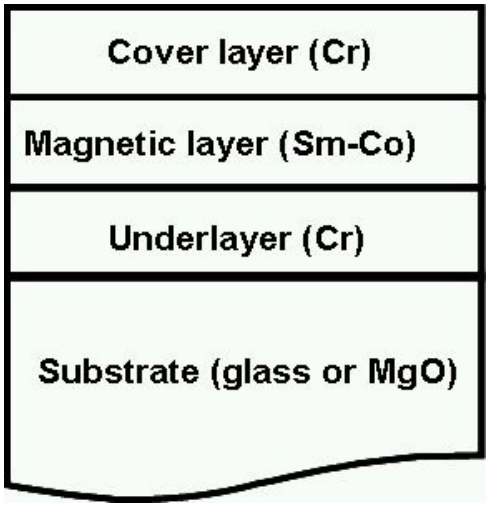

Fig. 3.2. Schematic diagram of the multilayer film structure.

The film structure studied in this chapter is shown in Fig. 3.2. Four series of experiments were conducted to study the effects of the following factors on the structure and magnetic properties of Sm-Co films grown on glass substrate:

(1) The effect of the deposition temperature of the Cr underlayer;

(2) The effect of the thickness of the Cr underlayer;

(3) The effect of the thickness of the $SmCo_5$ layer;

(4) The effect of the composition of the Sm-Co layer.

In (1), (2) and (4), the thickness of the $SmCo_5$ film was kept at 45 nm. In (1), the deposition temperature of the Cr underlayer was adjusted from room temperature to 500 °C, while the thickness of the Cr underlayer was fixed at 60 nm. In (2), the deposition temperature was kept at 400 °C and the thickness of the Cr underlayer varied from 15 nm to 150 nm. In (3), the thickness of the Cr underlayer was kept at 60 nm and the deposition temperature was kept at 400 °C. The thickness of the $SmCo_5$ layer varied from 10 nm to 90 nm. In (4), the composition of 45 nm Sm-Co films varied from $Sm_{13}Co_{87}$ to $Sm_{33}Co_{67}$ when the thickness of the Cr underlayer was kept at 60 nm and the deposition temperature was kept at 400 °C. A 40 nm thick Cr cover layer was deposited to protect the Sm-Co layer from oxidation. The deposition temperature for the $SmCo_5$ films was always fixed at 400 °C. This is the optimal deposition temperature according to the study of $SmCo_5$ films grown on Cu underlayer (discussed in Chapter 4). Finally, a Cr (cover layer, 40 nm) / $SmCo_5$ (45 nm) / Cr (underlayer, 50 nm) film was deposited at 400 °C (temperature and thickness conditions found to be optimal) on a MgO (100) single crystal substrate for comparison between a glass substrate and a MgO (100) substrate.

3.2 Growth of Cr underlayer on glass substrate

3.2.1 Effect of deposition temperature

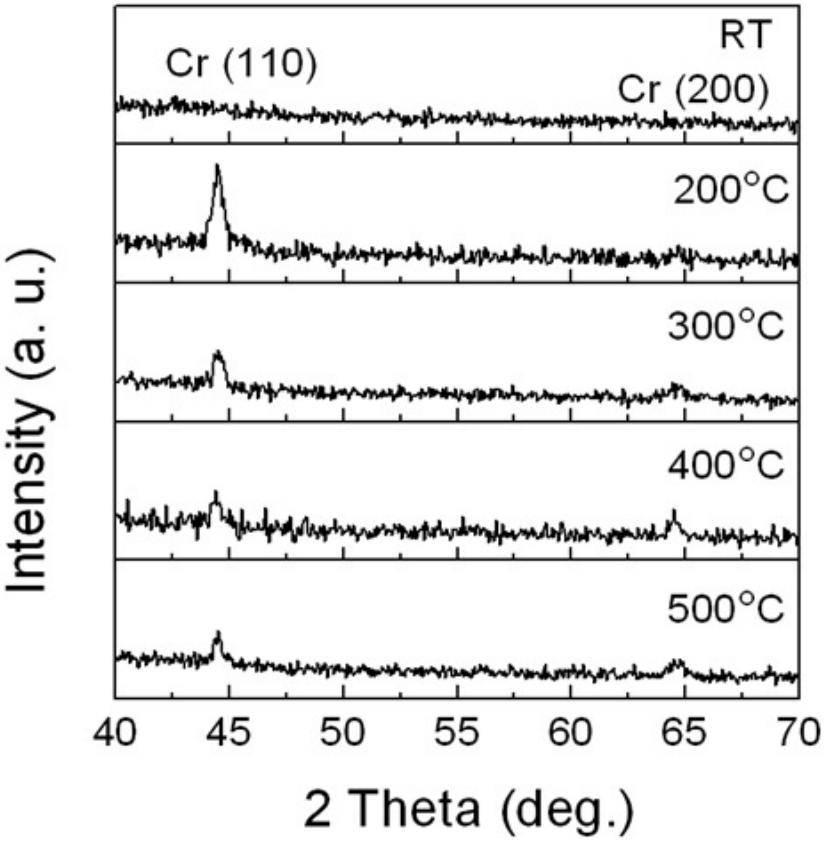

Fig. 3.3. XRD spectra of 60 nm Cr thin films deposited at different temperatures: from room temperature to 500 °C.

Cr films were deposited at different temperatures on glass substrate. The XRD spectra are shown in Fig. 3.3. The Cr film deposited at room temperature shows amorphous-like structure, while the film deposited at 200 °C exhibits the (110) texture which is the closest packed plane of bcc Cr. When the deposition temperature reaches 300 °C or above, the (200) peak appears. Here the integrated intensity ratio $\frac{I_{200}}{I_{110}}$ is used to quantitatively characterize the preferred orientation of Cr films,

where I_{200} and I_{110} are the integrated intensity of Cr (200) and (110) peaks. By comparing the value of $\frac{I_{200}}{I_{110}}$ for standard isotropic Cr powder sample (0.2) with the one obtained when deposing Cr at 400 °C or above (0.95), it can be determined that the preferred texture is (200) for the Cr thin film. The mechanism of the dependence of the Cr crystallographic textures on the substrate temperature was studied by Feng et al. [1]. They stated that before a continuous Cr film forms, the crystallographic texture originates from the preferential orientation of nucleation islands. High temperature increases the surface diffusion and hence promotes the initial islands which have (200) planes parallel to the film plane. Thus the (200) texture develops in the Cr film at elevated temperature.

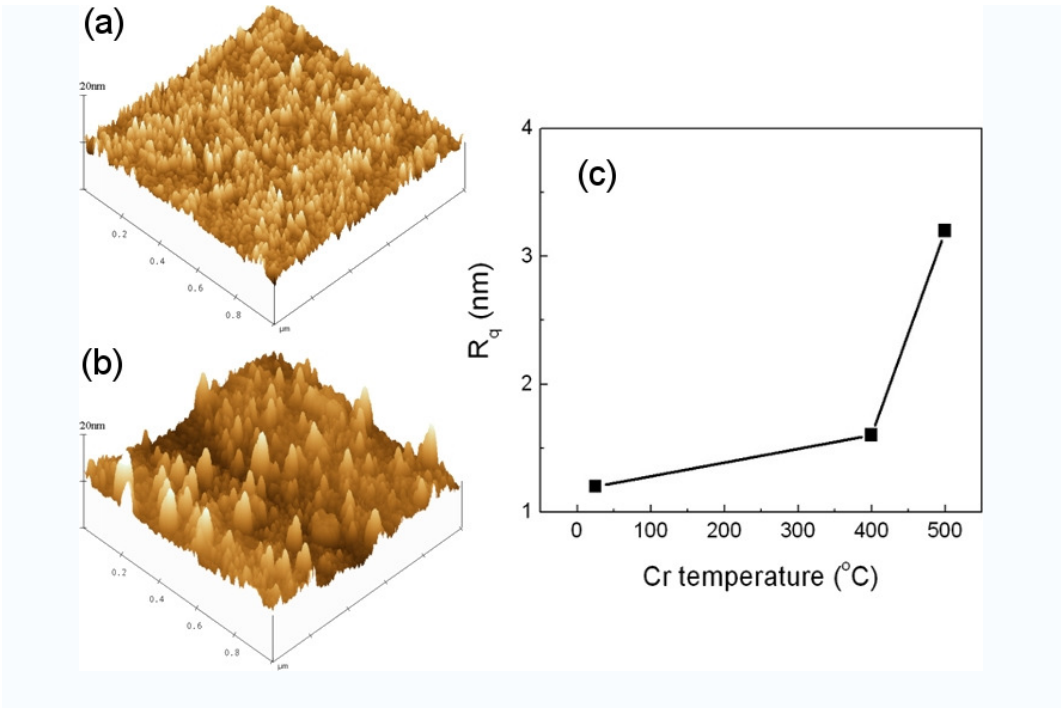

Fig. 3.4. AFM images of the surface of the Cr underlayer deposited (a) at 400 °C, (b) at 500 °C and (c) dependence of R_q of Cr films on the deposition temperature.

AFM was used to examine the surface structure and roughness of the Cr underlayers deposited at different temperatures. Relatively smooth Cr layer with a small particle size was found when the deposition temperature was below 400 °C. The root mean square roughness (R_q) increases from 1.6 nm for the film deposited at 400 °C to 3.2 nm after deposition at 500 °C as shown in Fig. 3.4a and b. The changes of R_q at different temperature are summarized in Fig. 3.4c. It indicates that high temperature (~500 °C) deteriorates the surface roughness. The roughness of the Cr underlayer may affect the crystallinity of the subsequently deposited $SmCo_5$ film.

3.2.2 Effect of thickness

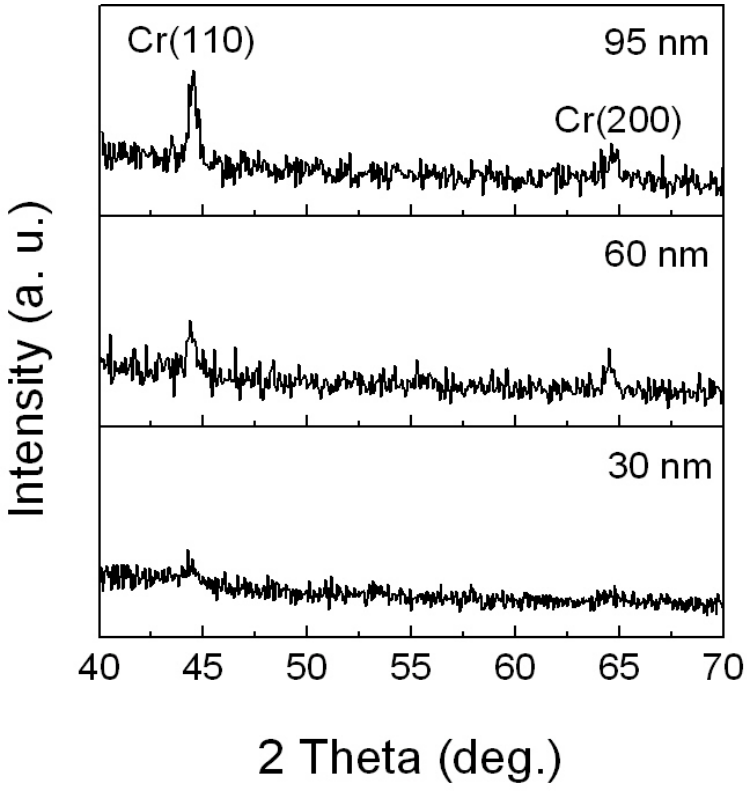

Fig. 3.5. XRD spectra of Cr thin films with different thicknesses deposited at 400 °C: from 30 nm to 95 nm.

From section 3.2.1, it can be seen that 400 °C is the optimized temperature for the growth of a high quality Cr (200) textured layer with a relatively small roughness. I studied the crystallographic structure and surface morphology of the pure Cr underlayers with different thickness deposited at 400 °C as shown in Fig. 3.5. The Cr underlayer with a thickness of 30 nm shows a disordered structure, as the crystalline peaks are very weak. The Cr underlayer with a thickness of 60 nm shows a clear (200) texture and an improved crystallinity. When the film thickness is increased to 95 nm, the crystallinity improves further, while the (200) texture declines. The AFM study indicates that there is no significant difference in the smoothness among the Cr underlayers with different thickness. The R_q are 1.6 nm, 1.6 nm and 2.3 nm for the Cr films with the thickness of 30 nm, 60 nm and 95 nm, respectively (Fig. 3.6).

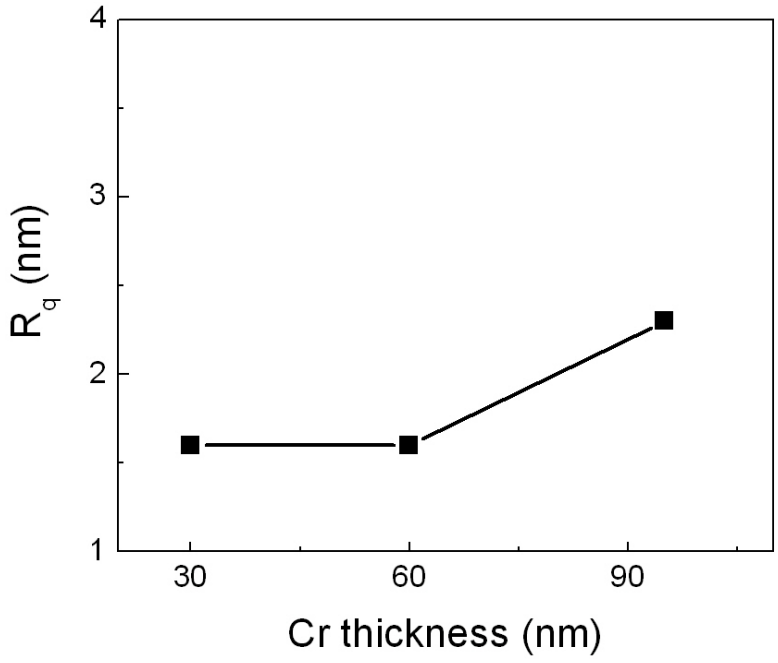

Fig. 3.6. Dependence of R_q of Cr films with different thickness.

3.3 Evaluation of Sm / Co atomic composition

All the Sm-Co films were deposited on Si substrates for calibration. The deposition power of Co was fixed at 50 W where its deposition rate was 3.3 nm / min. The deposition power of Sm was adjusted from 12 W to 30 W. The relation between the deposition rate of Sm and the deposition power is plotted in Fig. 3.7. The deposition rate is proportionally increasing with the deposition power.

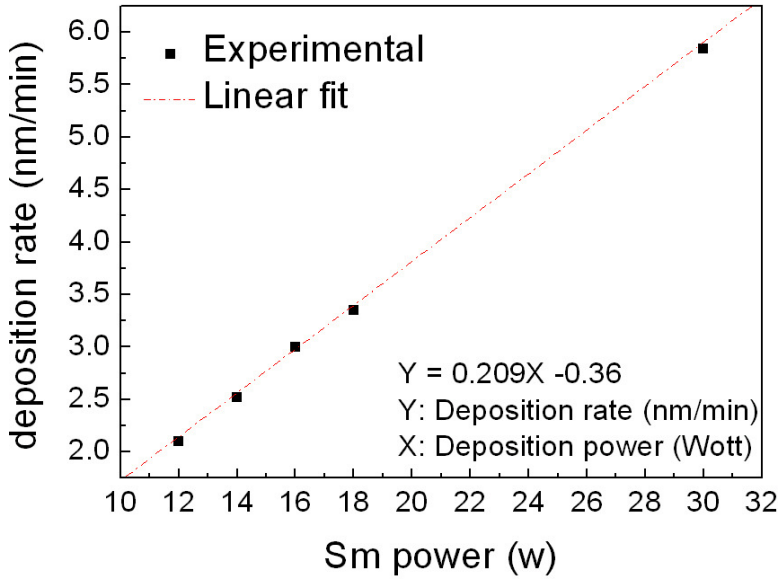

Fig. 3.7. Relation between deposition rate of Sm and deposition power.

Thus the deposition rate of Sm at different deposition power can be estimated from this relation. Thereafter the composition of Sm-Co films can be estimated by the following equation:

$$\frac{A_{Sm}}{A_{Co}} = \frac{N_A \quad D_{Sm} v_{Sm} \quad t / M_{Sm}}{N_A \quad D_{Co} v_{Co} \quad t / M_{Co}} = \frac{1}{3.09} \frac{v_{Sm}}{v_{Co}} \qquad \text{Eq. 3.1}$$

where, A is the number of atoms, N_A is Avogadro constant, D is density, v is deposition rate, t is deposition time and M is molar mass.

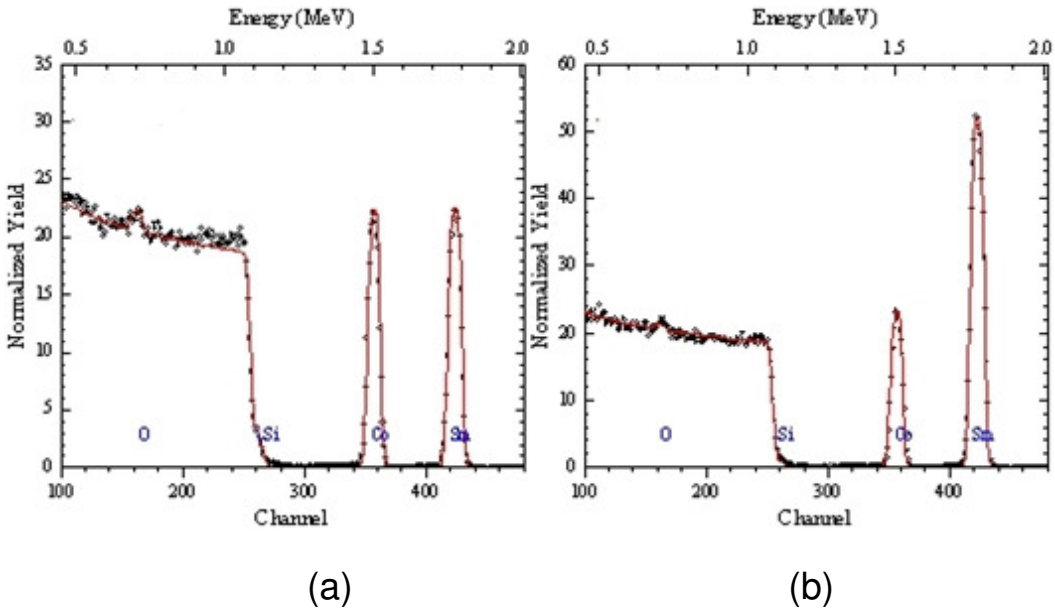

Fig. 3.8. RBS spectra of SmCo thin films deposited on Si substrate: (a) Sm at 14 W and Co at 50 W and (b) Sm at 20 W and Co at 50 W. The open circles represent the experimental data, whereas the solid curves represent the simulated data.

Table 3.1. Calibration of the atomic compositions of Sm-Co films deposited at different powers.

Sm power (W)	**Sm deposition rate (nm/min)**	**Co deposition rate (nm/min)**	**Estimated $SmCo_x$**	**Calibrated composition by RBS**
12	2.15	3.3	$SmCo_{4.8}$	$SmCo_{6.7}$
13	2.36	3.3	$SmCo_{4.3}$	$SmCo_{5.8}$
14	2.57	3.3	$SmCo_{4.0}$	$SmCo_5$
15	2.78	3.3	$SmCo_{3.7}$	$SmCo_{4.4}$
16	2.98	3.3	$SmCo_{3.4}$	$SmCo_{3.8}$
18	3.40	3.3	$SmCo_{3.0}$	$SmCo_{2.9}$
20	3.82	3.3	$SmCo_{2.7}$	$SmCo_{2.2}$
22	4.24	3.3	$SmCo_{2.4}$	$SmCo_{1.6}$

In order to calibrate accurately the Sm-Co composition, two samples were carefully evaluated by Rutherford Backscattering Spectometry (RBS). Fig. 3.8 shows the RBS spectra of two Sm-Co films deposited at (a) 14 W for Sm and 50 W for Co; (b) 20 W for Sm and 50 W for Co, respectively. The atomic compositions of these two films are identified as $SmCo_5$ and $SmCo_{2.2}$ respectively. According to those, I calibrated the atomic compositions of all the films deposited at different powers as summarized in Table 3.1.

3.4 Fabrication of $SmCo_5$ films with Cr underlayer on glass substrate and study of their structure and magnetic properties

3.4.1 Effect of deposition temperature of Cr underlayer

XRD spectra of the $SmCo_5$ films with the Cr underlayer deposited at different temperatures are shown in Fig. 3.9. The Cr diffraction line indexing is based on PDF File No. 06-0694 and the $SmCo_5$ indexing is based on PDF File No. 35-1400. It can be seen that only the Sm-Co film with the Cr underlayer deposited at 400 °C shows a clear $SmCo_5$ $(11\bar{2}0)$ peak. The Sm-Co layers might have a disordered structure (amorphous-like) in the cases where Cr underlayer was deposited at relatively lower deposition temperatures (room temperature to 300 °C). Furthermore, the average grain size of $SmCo_5$ on glass substrate was calculated to be 5-10 nm according to Scherrer's equation. However, no $SmCo_5$ peaks could be found on the Cr underlayer when it was deposited at 500 °C. This is probably due to the rough surface of the Cr underlayer deposited at 500 °C which may affect the crystallinity of the subsequently deposited $SmCo_5$ film as discussed in the Cr underlayer study (Fig. 3.4).

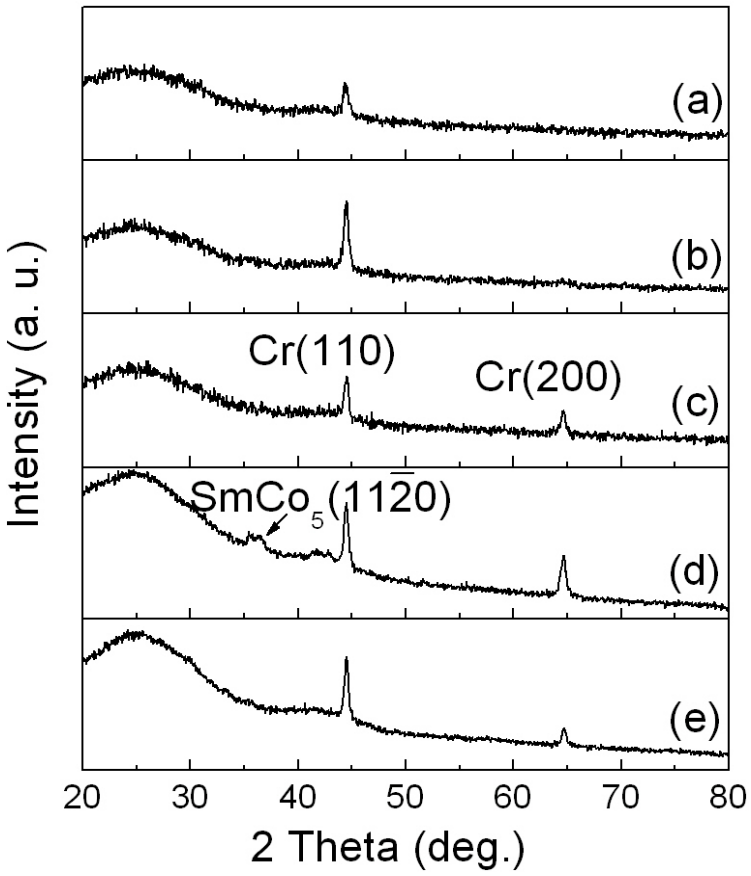

Fig. 3.9. XRD spectra of Cr/Sm-Co/Cr thin films with the Cr underlayers deposited at different temperatures: (a) room temperature, (b) 200 °C, (c) 300 °C, (d) 400 °C, (e) 500 °C.

Fig. 3.10 shows the corresponding M-H loops of $SmCo_5$ thin film with Cr underlayers deposited at different temperatures. The dependence of the in-plane and out-of-plane ${}_iH_c$ of 45 nm $SmCo_5$ films on the deposition temperature of the Cr underlayer are summarized in Fig. 3.11. Results indicate that the ${}_iH_c$ of $SmCo_5$ films strongly depends on the deposition temperature of the Cr underlayer. The in-plane ${}_iH_c$ of the $SmCo_5$ film increases slightly as the deposition temperature of Cr underlayer varies from room temperature to 300 °C, while it increases greatly to 18 kOe at 400 °C, but it drops to 2 kOe at 500 °C. This is probably due to the rough surface of Cr underlayer deposited at 500 °C (Fig. 3.4) that affected the growth of

Sm-Co film as discussed in the above section. On the other hand, all the films exhibit very small out-of-plane ${}_iH_c$ (<1 kOe). These results indicate that the films exhibit a large in-plane magnetic anisotropy, suggesting that the easy axis of magnetization of $SmCo_5$ lies in the film plane. The high in-plane intrinsic coercivity and high in-plane magnetic anisotropy demonstrated in the $SmCo_5$ film with the Cr underlayer deposited at 400 °C is due to a good crystallinity of $SmCo_5$ phase with a $(11\bar{2}0)$ texture as shown in Fig. 3.9.

From the above results, one can conclude that the intrinsic coercivity of Sm-Co film is strongly dependent on the crystallinity and texture, which can be strongly affected by the Cr underlayer (crystallinity, texture and roughness).

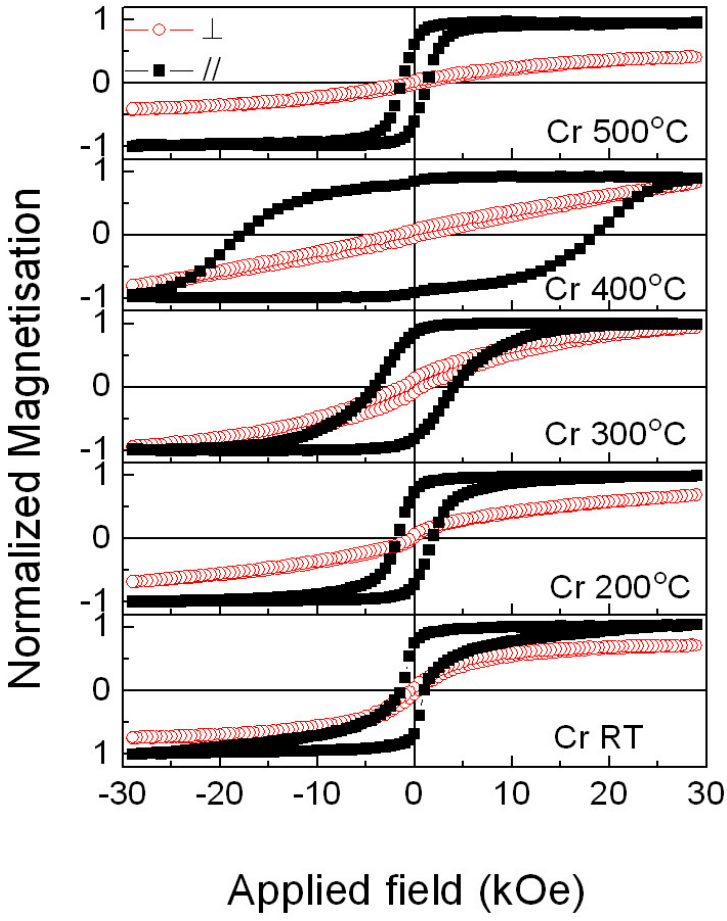

Fig. 3.10. M-H loops of $SmCo_5$ thin film with Cr underlayers deposited at different temperatures.

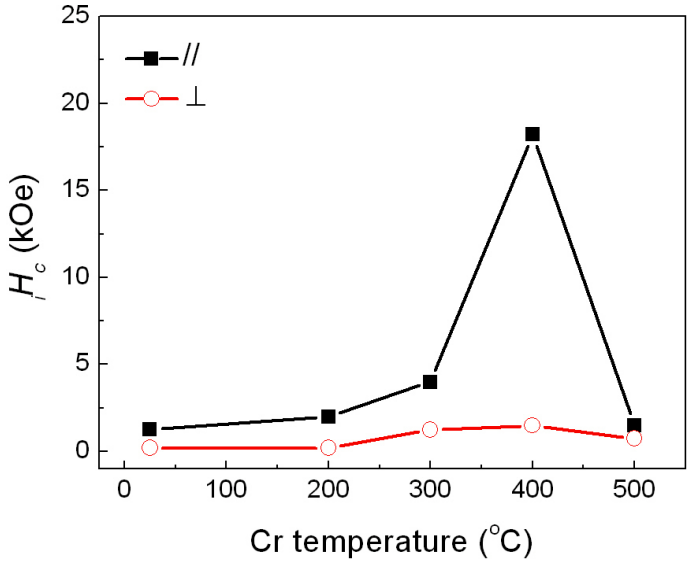

Fig. 3.11. Dependence of in-plane and out-of-plane ${}_iH_c$ of $SmCo_5$ films on the Cr underlayer deposition temperature.

3.4.2 Effect of thickness of Cr underlayer

The effect of the Cr underlayer thickness on the magnetic properties of $SmCo_5$ films was investigated. As shown in Fig. 3.12, the $SmCo_5$ film deposited on the Cr underlayer with a thickness of 30 nm shows a poor crystallinity, indicated by a weak and broad $(11\bar{2}0)$ peak. On the other hand, a relatively strong $(11\bar{2}0)$ peak in $SmCo_5$ film with a 95nm Cr underlayer shows an improved crystallinity.

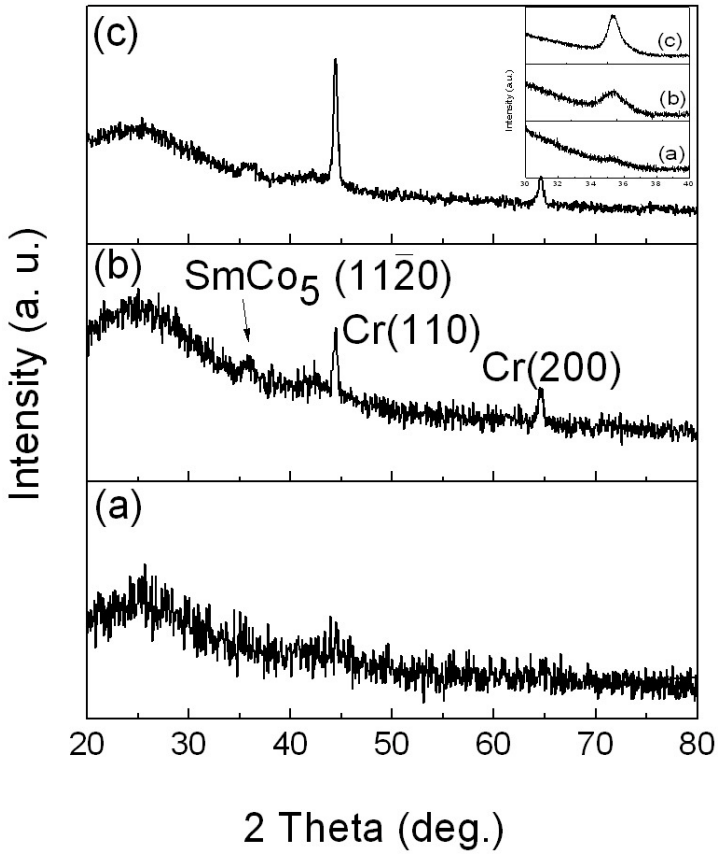

Fig. 3.12. XRD spectra of Cr / Sm-Co / Cr thin films with (a) 30 nm Cr underlayer and (b) 60 nm Cr underlayer and (c) 95 nm Cr underlayer. The inset is the XRD spectra of $SmCo_5$ $(11\bar{2}0)$ peaks of these three samples with a long time scan.

Fig. 3.13 summarizes the in-plane and out-of-plane intrinsic coercivities for $SmCo_5$ films which were deposited on Cr underlayers with different thicknesses in

the range of 15-150 nm. It can be seen that Sm-Co films show soft isotropic magnetic properties without a Cr underlayer or with a thin Cr underlayer. The in-plane ${}_iH_c$ of the $SmCo_5$ films increases significantly with the increased thickness of Cr underlayer from 30 nm to 45 nm. The results indicate that the crystallinity of Cr plays an important role in the magnetic properties of $SmCo_5$ films.

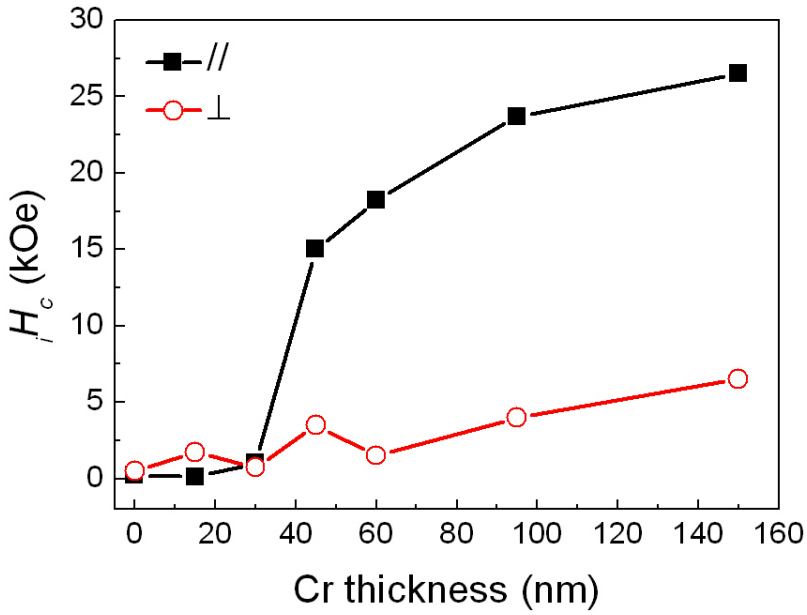

Fig. 3.13. Dependence of in-plane and out-of-plane ${}_iH_c$ in $SmCo_5$ films on the thickness of Cr underlayer.

This work shows again, that high intrinsic coercivity is accompanied by good crystallinity. The largest in-plane intrinsic coercivity, 26.5 kOe, was obtained in the sample with the Cr underlayer of 150nm which was measured by SQUID with a maximum filed of 50 kOe.

3.4.3 Effect of thickness of $SmCo_5$ layer

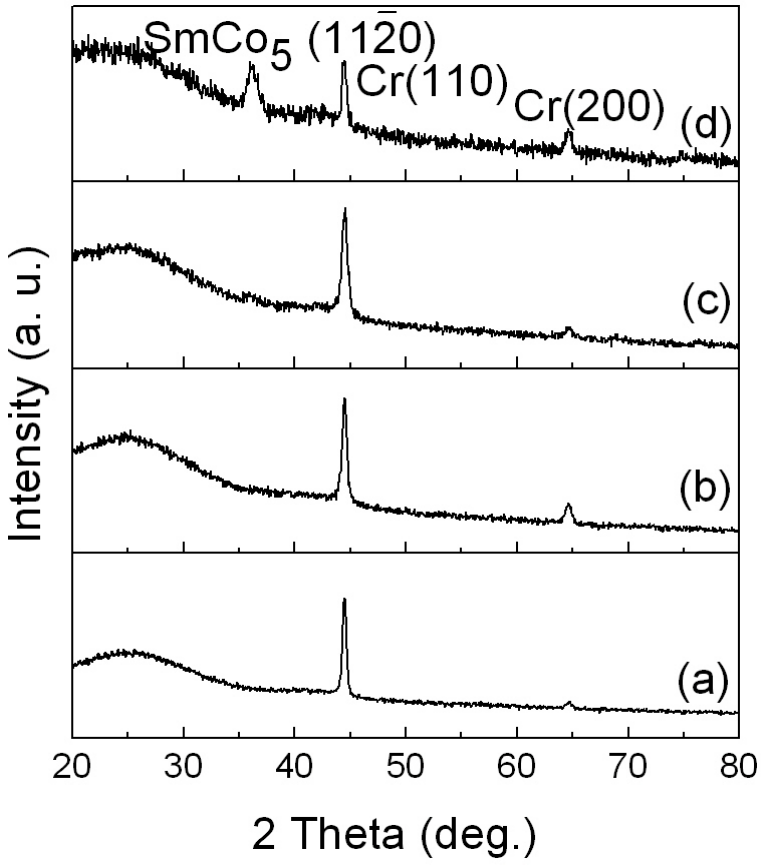

Fig. 3.14. XRD spectra of Cr(40 nm) / Sm-Co(*t* nm) / Cr(60 nm) thin films: (a) *t*=10 nm, (b) *t*=30 nm, (c) *t*=45 nm and (d) *t*=90 nm.

The following work is the investigation of the effect of the thickness of $SmCo_5$ layer on the magnetic properties of $SmCo_5$ films. Sm-Co films with layer thickness ranging from 10 to 90 nm were prepared on 60 nm Cr underlayer at 400 °C. The corresponding XRD spectra for these samples are shown in Fig. 3.14. With the increasing Sm-Co film thickness, the $SmCo_5$ $(11\bar{2}0)$ peak becomes visible and stronger. Though the film thickness can affect the peak intensity, the much higher intensity of the $(11\bar{2}0)$ peak of the $SmCo_5$ film with a thickness of 90 nm implies an

improved crystallinity. The out-of-plane ${}_iH_c$ remain low, similar to the results shown in Fig. 3.11 and Fig. 3.13. The in-plane ${}_iH_c$ as a function of the thickness of the Sm-Co films is shown in Fig. 3.15. It can be seen that the ${}_iH_c$ increases with the increasing $SmCo_5$ film thickness and goes to a value of 20 kOe at a thickness of 90 nm. The increase of the in-plane intrinsic coercivity may be due to the improvement of the crystallinity of $SmCo_5$ $(11\bar{2}0)$.

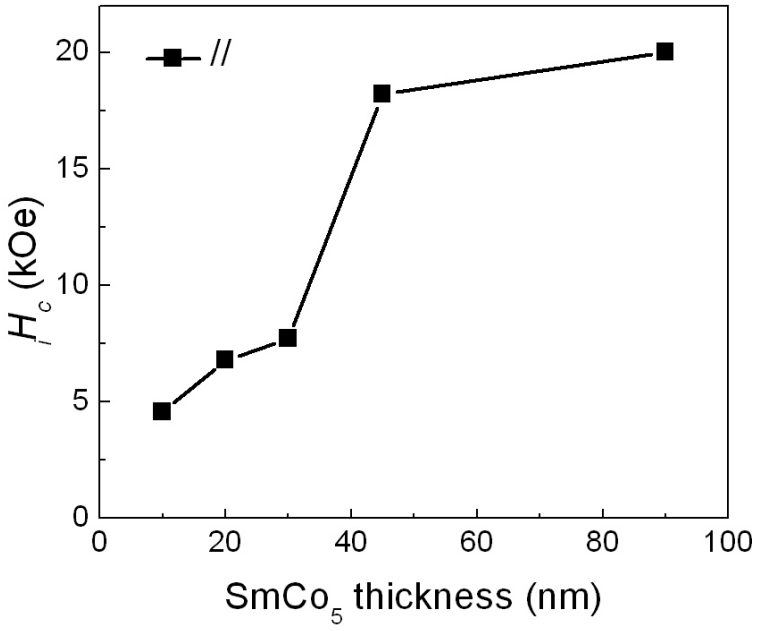

Fig. 3.15 Dependence of in-plane intrinsic coercivity in $SmCo_5$ films on the thickness of $SmCo_5$ layer.

3.4.4 Effect of Sm / Co composition

Fig. 3.16 shows the dependence of the in-plane ${}_iH_c$ on Sm content. The highest ${}_iH_c$ is achieved in the $SmCo_5$ films where Sm content is 16.7%. The ${}_iH_c$ decreases rapidly with either lower Sm content ($SmCo_7$) or higher Sm content ($SmCo_4$ - $SmCo_{2.2}$). From the XRD results, it was observed that only the film with a

composition of $SmCo_5$ shows $(11\bar{2}0)$ peak. The other Sm-Co films show no distinct $SmCo_5$ peaks. Therefore the high ${}_iH_c$ in $SmCo_5$ film is probably due to a better crystallinity compared to other films. Speliotis et al. [2] and Zhang et al. [3] reported similar results.

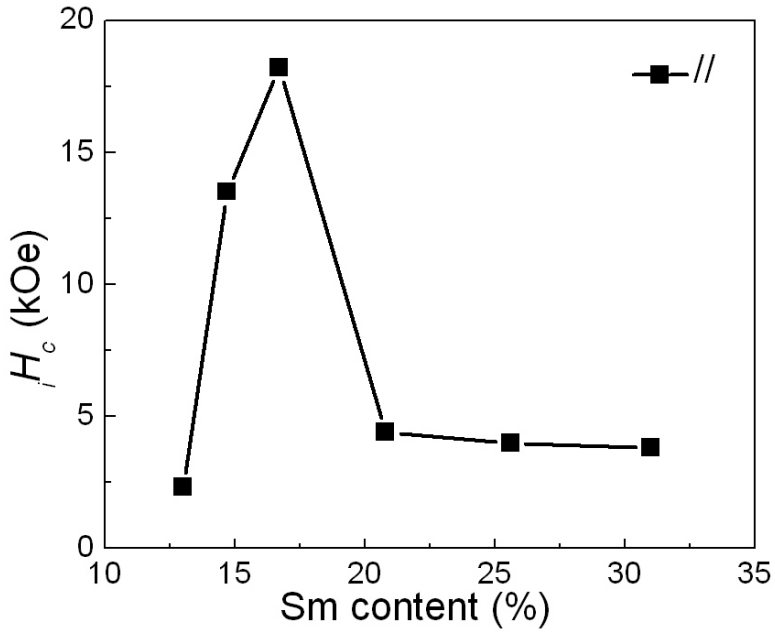

Fig. 3.16. Dependence of in-plane intrinsic coercivity of $SmCo_5$ thin films on Sm content.

3.5 Comparison study of $SmCo_5$ thin film grown on MgO (100) and glass substrates with Cr underlayer

For the comparison study, the Sm-Co/Cr thin films were deposited on the MgO (100) (Sample A) and glass substrates (Sample B) at the optimal condition as shown in Table 3.2.

Table 3.2. Film structure and magnetic properties of Sample A and Sample B.

	Substrate	Film structure	T_{sub} ($^{\circ}C$)	H_c (kOe)	M_r/M_s
Sample A	MgO (100) single crystal	Cr 40 nm / $SmCo_5$ 45 nm / Cr 50 nm	400	17.5	0.80
Sample B	Corning glass	Cr 40 nm / $SmCo_5$ 45 nm / Cr 50 nm	400	18.5	0.88

3.5.1 Crystallographic structure and microstructure

Fig. 3.17a and b show the XRD spetra of Sample A and Sample B. For Sample A, the peaks from MgO (200), Cr (200) and $SmCo_5$ $(11\bar{2}0)$ reflections are clearly observed. The average grain size of $SmCo_5$ is around 20 nm based on the XRD (calculated from $SmCo_5$ $(11\bar{2}0)$ peak using the Scherrer's equation) and TEM examinations. For Sample B, both (110) and (200) peaks of Cr were detected. As discussed before, the pure Cr underlayer grown on glass substrate has a preferred (200) orientation because the $\frac{I_{200}}{I_{110}}$ ratio of the Cr underlayer is 0.95, where I_{200} and I_{110} are the integrated intensity of Cr (200) and (110) peaks. This ratio is much larger than that of standard isotropic Cr sample (0.2). A relatively weak and broad peak from $SmCo_5$ $(11\bar{2}0)$ shows the possibility of a $(11\bar{2}0)$ texture. According to Scherrer's equation, the average grain size of $SmCo_5$ on glass substrate is around 8 nm. The inset in Fig. 3.17b shows the selected area electron diffraction pattern (SAED) of the $SmCo_5$ film from a cross section of Sample B. The diffraction ring

from $SmCo_5$ (11 $\bar{2}$ 0) is observed which confirms the $SmCo_5$ (11 $\bar{2}$ 0) texture in Sample B. The microstructure of the $SmCo_5$ films was examined using TEM.

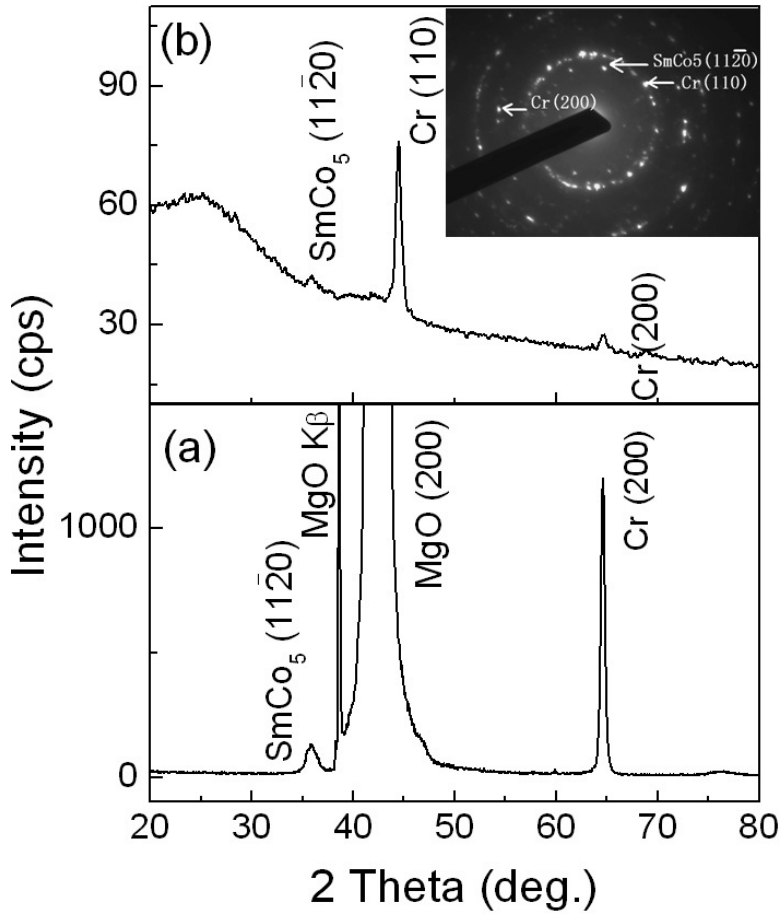

Fig. 3.17. XRD spectra of (a) Sample A and (b) Sample B. The inset in (b) shows the selected area electron diffraction (SAED) pattern of Sample B.

The TEM bright field of Sample A and Sample B are shown in Fig. 3.18. The Cr underlayer, $SmCo_5$ magnetic layer and Cr cover layer are clearly shown. The interface between the Cr underlayer and the $SmCo_5$ magnetic layer is relatively smooth whereas the interface between the $SmCo_5$ layer and the Cr cover layer is relatively rough because of the high deposition temperature. The nanocrystalline structure could be seen in the $SmCo_5$ layer. Amorphous or amorphous-like structure

has been reported in Sm-Co films [6-9]. Liu *et al.* proposed that very small crystallites of 5nm are surrounded by amorphous phase in Sm-Co films [8].

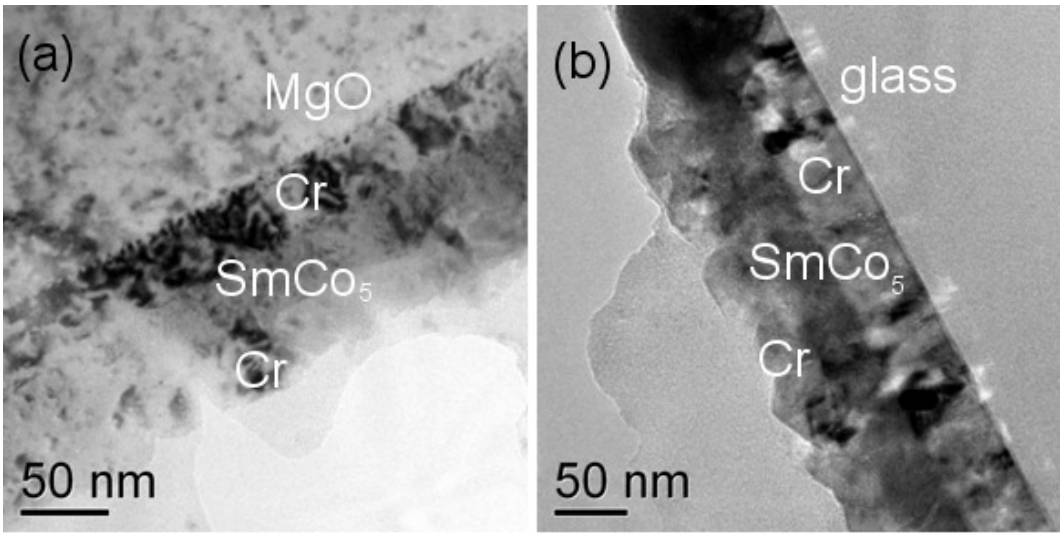

Fig. 3.18. TEM bright field image and dark field image of Sample B.

The epitaxial relationships between the $SmCo_5$ film, the Cr underlayer and the MgO substrate were investigated by off-specular reflection (also called phi scan). For Sample A, the off-specular MgO (111), Cr (101) and $SmCo_5$ (111) phi scans (53.5º, 45º and 32º away from the specular rod, respectively) were used to measure the epitaxial relationships among $SmCo_5$/Cr/MgO. The typical phi scan results of Sample A are shown in Fig. 3.20. Four MgO {111} diffraction peaks with an even spacing of 90º are observed and four Cr {101} peaks are found at the same positions. Four $SmCo_5$ {111} peaks with an even 90° spacing appear at 45° rotated positions with respect to the Cr surface. This indicates that the Cr underlayer epitaxially grows on the MgO substrate and $SmCo_5$ in turn follows an epitaxial growth on Cr.

According to the relative directions of the MgO, Cr and $SmCo_5$ crystalline axes, the epitaxial relationship is derived as $SmCo_5$ $(11\bar{2}0)$ <0001> // Cr (200) <110> // MgO (200) <010>. The epitaxial relationship is illustrated in Fig. 3.1. This

epitaxial relationship was first reported by Fullerton et al. [4] and later was proved by Singh et al. using pole figure measurements [5]. On the other hand, for Sample B, Cr (101) and $SmCo_5$ (111) phi scans have been measured but no peaks are observed.

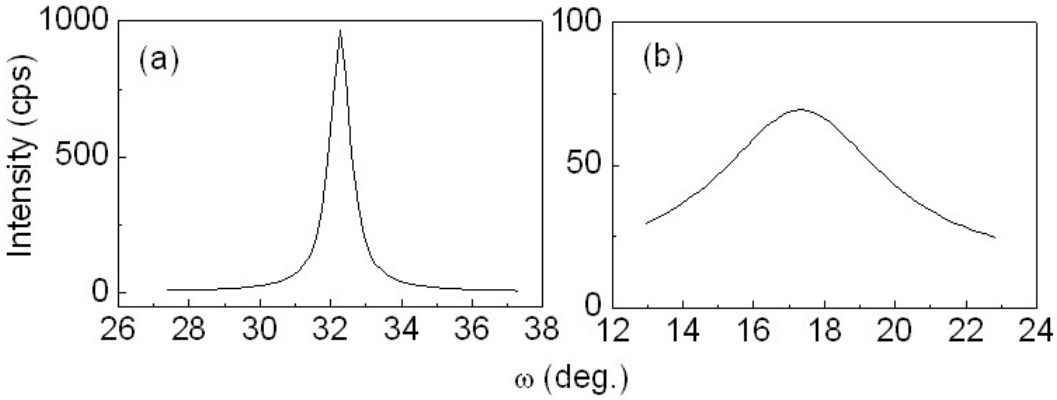

Fig. 3.19. XRD rocking curves of (a) Cr (200) and (b) $SmCo_5$ (110) peaks of Sample A.

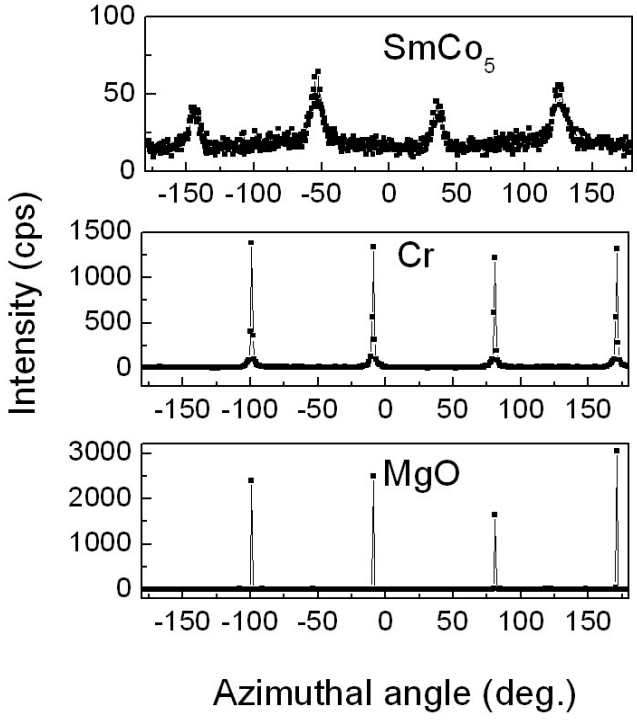

Fig. 3.20. XRD off-spectra phi scan of MgO (111), Cr (101) peaks and $SmCo_5$ (111) of Sample A.

Hence, with the results discussed above, the microstructure models are proposed for Sample A and Sample B as illustrated in Fig. 3.21. For Sample A, the $SmCo_5$ film is well $(11\bar{2}0)$ textured with the easy axis – [0001] either along Cr [011] or Cr $[01\bar{1}]$ directions. The grain size is around 20 nm. For Sample B, the $SmCo_5$ film has only a preferred $(11\bar{2}0)$ orientation. The easy axes of $SmCo_5$ grains are supposed to have a random distribution.

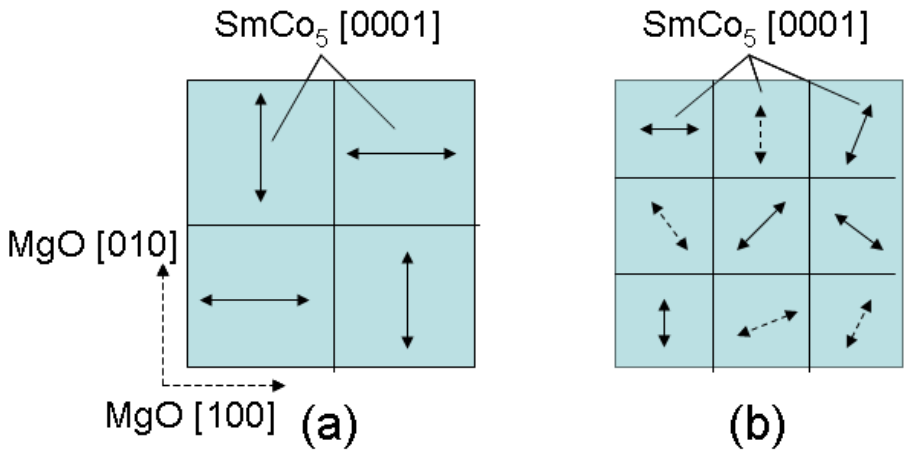

Fig. 3.21. The illustration of grains distribution in (a) Sample A and (b) Sample B. The arrows indicate the easy axis directions. The solid arrows represent the easy axes which lie in the film plane and the dash arrows represent those are not in the film plane.

3.5.2 Magnetic properties

Fig. 3.22 shows the magnetic hysteresis loops of Sample A and Sample B measured in three different directions: for Sample A, in the film plane along the MgO [010], in the film plane along the MgO [001], and in the out-of-plane direction (along the MgO [100]); for Sample B, in the film plane along a certain direction, in the film plane after a rotation of 45° and in the out-of-plane direction. It can be seen that both samples show high in-plane anisotropy. The ${}_iH_c$ of sample A and B are 17.5

kOe and 18.5 kOe respectively while the out-of-plane ${}_iH_c$ of both samples are small around 2 kOe.

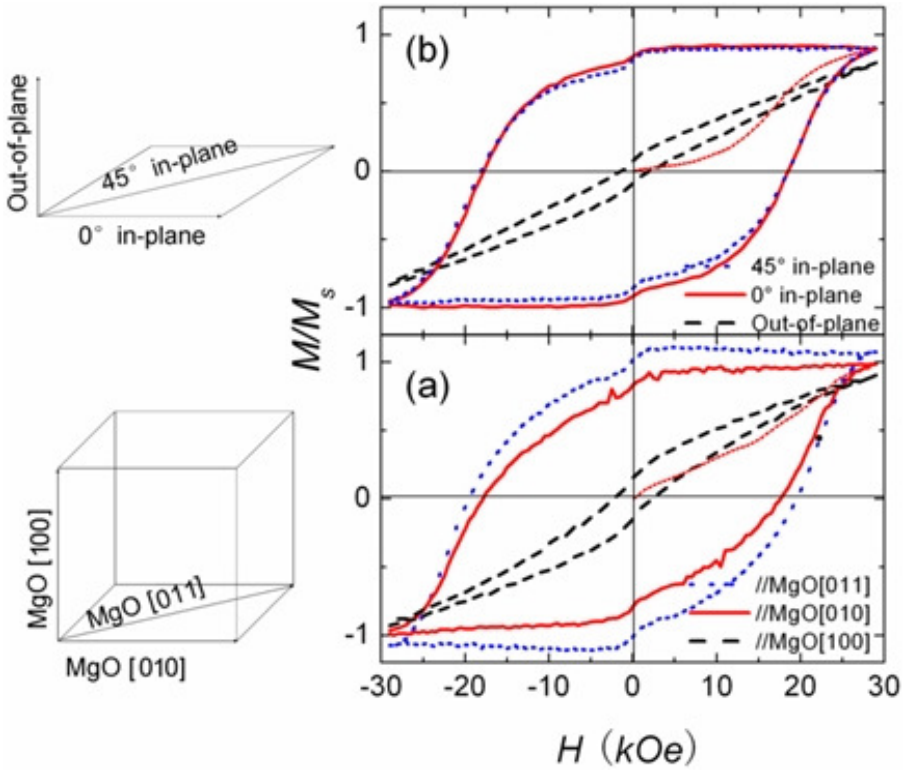

Fig. 3.22. M-H loops of (a) Sample A, measured along the MgO [011], MgO [011], and MgO [100] directions; (b) Sample B, measured along 0° in-plane, 45° in-plane and out-of-plane directions.

Besides the in-plane anisotropy, a large in-the-film-plane anisotropy is exhibited in the epitaxial $SmCo_5$ film grown on MgO substrate. Here I defined the "in-the-film-plane anisotropy" as the dependence of the internal energy on the direction of easy magnetization in the film plane. For example, Sample A exhibits higher coercivity field and remanent magnetization along the MgO [011] direction than those along the MgO [010] direction (shown in Fig. 3.22a). The increases of coercivity along the MgO [011] direction were reported by other researchers [4, 5, 10]. Benaissa and Krishnan proposed the possible reason for the enhancement of

coercivity in the bicrystalline microstructure [10]. Due to the ferromagnetic exchange coupling, a "cluster" may form by an ensemble of adjacent SmCo grains which are along either the Cr [011] or the Cr [$01\bar{1}$] directions (as illustrated in Fig. 3.1). Such a cluster has an effective anisotropy along the MgO [011]. The increase of coercivity along the MgO [011] direction depends on the strength of the inter-granular exchange coupling. The increase of coercivity along the MgO [011] in my sample maybe due to the exchange coupling which will be discussed below. Unfortunately, due to the limited applied field of the available VSM, the M-H loop can not be saturated along MgO [011] direction. Thus the observed coercivity may be smaller than the real value. On the other hand, Sample B shows similar hysteresis loops at different in-plane directions. It indicates that there is no distinct easy axis direction within the film plane.

I also studied remanence for the two samples. For the remanence analysis, The measurements in MgO [010] direction and MgO [011] direction were performed for Sample A. If it is assumed that the [0001] direction of the $SmCo_5$ grains randomly lies along either in the direction of the Cr [011] or [$01\bar{1}$], there should be a 50% possibility for each case. Therefore, when a sufficiently strong external field is applied along the MgO [010] (Cr [011]), all magnetizations are aligned to MgO [010] direction. When the external field decreases to 0, 50% of the domain magnetizations turn back to their easy axis direction (// Cr [$01\bar{1}$]), which do not contribute to the overall magnetization along the MgO [010] with a perpendicular configuration. The remanent magnetization M_r should be one-half (0.5) of the saturation magnetization M_s. On the other hand, when a strong external field is applied along the MgO [011], all magnetizations are parallel to the direction of the

MgO [011]. When the external field is removed, every domain magnetization rotates to its easy axis direction along the direction of either Cr [011] or [$01\bar{1}$]. Thus the remanent magnetization M_r should be $\sqrt{2}/2\ M_s$ (0.71). The remanence along the direction of the MgO [011] is expected to be higher than that along the direction of the MgO [010]. Sample A shows a remanent magnetization M_r along MgO [010] direction is 0.80 M_s while the M_r along MgO [011] direction is 0.94 M_s. Though the measurements agree with my expectation (higher remanence along the MgO [011] direction), the values are significantly higher than the expected values (0.5 and 0.71). The high remanence values may be attributed to exchange coupling between grains, as discussed below.

For Sample B, a part the $SmCo_5$ grains show the ($11\bar{2}0$) orientation, the easy axes of which are expected to distribute randomly in the film plane. The rest grains may not have their easy axes aligned in the film plane. The distribution of the easy axes in sample B should be between 2 dimensional isotropic distribution (if easy axes are randomly distributed in the film plane) and 3 dimensional distribution (if easy axes are randomly distributed without any preferred orientation). The intensity of the remanent magnetization is calculated to be [11]:

$$M_r = \frac{1}{\pi}\int_{-\pi/2}^{\pi/2} M_s \cos\theta d\theta = 0.637 M_s \quad \text{(2D model)} \qquad \text{Eq. 3.1}$$

$$M_r = \int_{0}^{\pi/2} M_s \cos\theta \sin\theta d\theta = 0.5 M_s \quad \text{(3D model)} \qquad \text{Eq. 3.2}$$

where, θ is the angle between the direction of applied field and easy axis (in the film plane).

However, the remanent magnetization M_r of Sample B is 0.88 M_s which is much larger than both of these models above. The remanence enhancement was explained by the exchange coupling between spins in the grain boundary areas [12, 13]. The exchange coupling occurs when the grain size is comparable to the exchange length which is two times the thickness of the domain wall. The thickness of the domain wall is 2.2-2.7 nm for $SmCo_5$ [14]. As discussed above, the $SmCo_5$ grain size of Sample A and Sample B are around 20 nm and 8 nm respectively. The small grain sizes in the two samples are comparable to the thickness of the domain wall and result in exchange coupling. The exchange coupling leads to the increased coercivity along the MgO [011] in Sample A and enhanced remanence in both sample A and sample B. A smaller grain size in Sample B leads to a larger remanence increase. The remanence enhancement in nanocrytalline SmCo has been reported previously [15]. The film structure and magnetic properties of Sample A and Sample B are summarized in Table 3.2.

The demagnetization curve and recoil curves for Sample B are shown in Fig. 3.23a. The curves are similar to those of nanocrystalline single-phase $Nd_{12}Fe_{14}B$ magnets showing remanence enhancement [12, 13]. The reversible ability of the $SmCo_5$ film is high (spring-magnet behavior [12, 13]). As discussed in Chapter 2, according to the demagnetization curve, the Wohlfarth relationship: $M_d(H) = M_{r,max} - 2M_r(H)$ could be decuced and it has been widely used for the investigation of intergranular interaction. The deviation ΔM_d has been used to characterize the interactions.

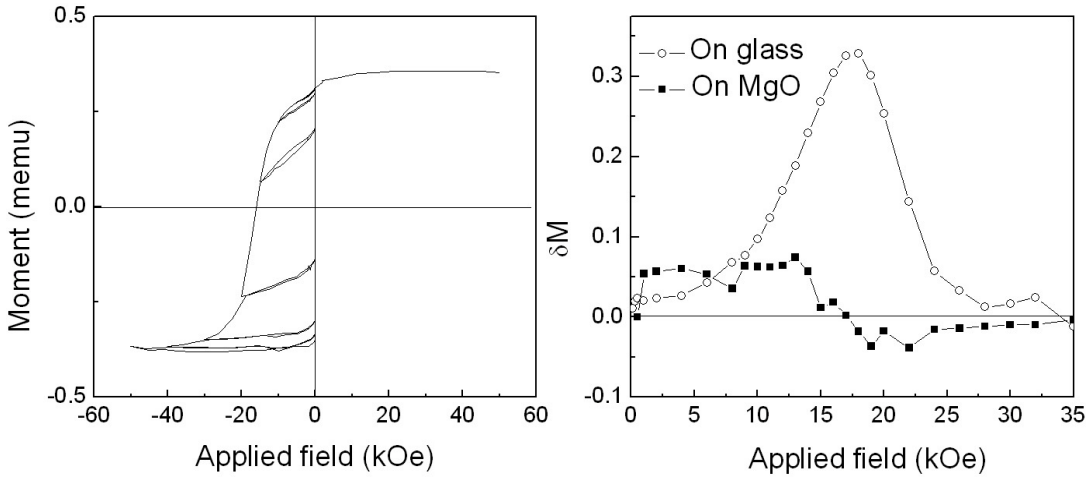

Fig. 3.23. (a) The demagnetization curve and recoil curves for Sample B. (b) The normalized deviation of demagnetization remanence $\Delta M_d(H)$ versus the applied field for Sample A and B.

Fig. 3.23b shows the curves of the normalized deviation ΔM_d versus the applied field for Sample A and Sample B. Both of the curves from two samples show positive peaks which indicate exchange coupling between grains. For Sample B, the curve shows a relatively large positive peak, which indicates a strong exchange coupling between grains in the nanocrystalline $SmCo_5$ film. The result is associated with the large remanence enhancement discussed before. Moreover, because of the strong interactions between these oriented grains and the neighbour grains, although only part of the grains have a $(11\bar{2}0)$ orientation, they can hold the overall magnetization direction in the film plane to enable a large in-plane anisotropy and high remanence. In contrast, the textured $SmCo_5$ film with larger grains grown on MgO substrate shows a much smaller positive peak due to the weak interactions between the grains.

Fig. 3.24 shows the angular dependence of coercivity field for $SmCo_5$ films deposited on different substrates. ψ is the angle between the applied field and the

easy direction of magnetization. The Sample A shows increased coercivity in the range of 0°-45° which is similar to Kondorsky's relation. The analytical model-Kondorsky's relation which is proportional to 1/cos(ψ) usually indicates a domain wall motion mechanism [16]. It may indicate that there are some pinning sites in Sample A. For Sample B, the coercivity field keeps decreasing with the increasing angle. It might due to the large misalignment of easy axis in Sample B. Since the single domain diameter of $SmCo_5$ was around 710 - 960 nm [14], the particles (here grains) in my samples are too small to contain a domain wall inside of a grain. The switching modes of two samples may follow the incoherent nucleation curling model [17-19].

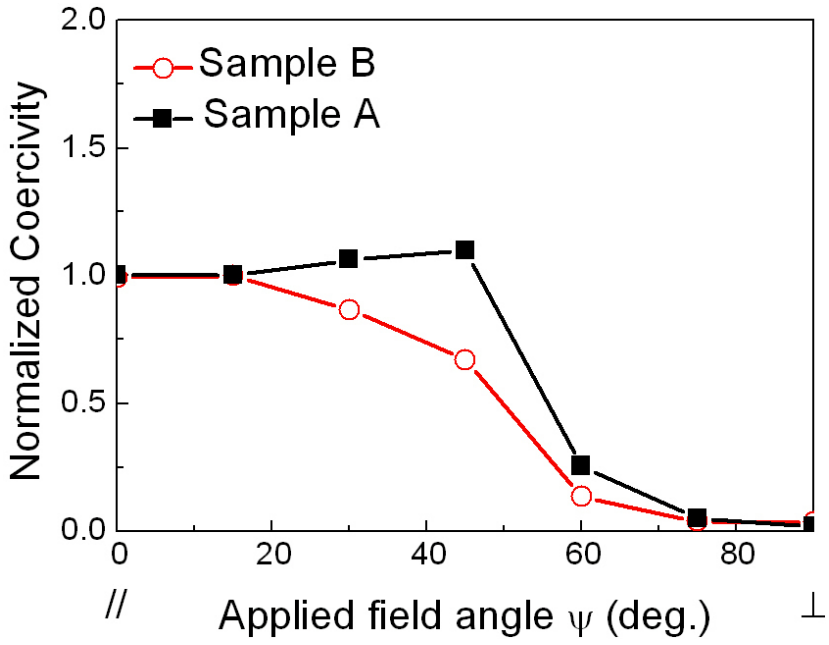

Fig. 3.24. Angular dependence of normalized coercivity of Sample A and Sample B. Zero field refers to in plane direction.

3.6 Summary

Three effects on magnetic properties of $SmCo_5$/Cr films deposited on glass substrates have been investigated. It has been found that a high-quality Cr underlayer can be obtained after deposition at 400 °C with a good (200) texture and a smooth surface. A lower deposition temperature prefers the formation of a disordered Cr film with a (110) texture, while a higher deposition temperature causes rough film surface. The Cr underlayer needs a minimum thickness of 40-60 nm in order to have a good crystallinity. When $SmCo_5$ is deposited at 400 °C, a $(11\bar{2}0)$ texture can be induced if the Cr underlayer has a (200) texture. Again, high intrinsic coercivity requires a minimum thickness of the $SmCo_5$ layer in the order of 50 nm, as a thinner film possesses a poor crystallinity. The resultant films exhibit high in-plane coercivity and a large in-plane magnetic anisotropy with a nanocrystalline structure. High in-plane intrinsic coercivity up to 26.5 kOe and large in-plane anisotropy can be achieved in $SmCo_5$ films on glass substrate, if a smooth Cr underlayer with a (200) texture is present.

Moreover, a comparison study was conducted concerning the crystallographic structure, microstructure and magnetic properties of the $SmCo_5$ thin films with Cr underlayer grown on MgO (100) and glass substrates. The epitaxial relationship $SmCo_5$ $(11\bar{2}0)$ <0001> // Cr (200) <011> // MgO (200) <010> is demonstrated between $SmCo_5$, Cr and MgO substrate. Polycrystalline $SmCo_5$ with a preferred $(11\bar{2}0)$ orientation on amorphous glass substrate shows an even higher in-plane coercivity and remanence enhancement due to the nanocrystalline structure and strong interaction between grains.

3.7 References

[1]. Y. C. Feng, D. E. Laughlin and D. N. Lambeth, J. Appl. Phys. **76**, 7311 (1994).

[2]. T. Speliotis and D. Niarchos, J. Magn. Magn. Mater. **290**, 1195 (2005).

[3]. J. Zhang, Y. K. Takahashi, R. Gopalan and K. Hono, J. Magn. Magn. Mater. **310**, 1 (2007).

[4]. E. E. Fullerton, J. S. Jiang, C. Rehm, C. H. Sowers, S. D. Bader, J. B. Patel, and X. Z. Wu, Appl. Phys. Lett. **71**, 1579 (1997).

[5]. A. Singh, V. Neu, R. Tamm, K. Subba Rao, S. Fähler, W. Skrotzki, L.

[6]. Schultz, and B. Holzapfel, Appl. Phys. Lett. **87**, 072505 (2005).

[7]. E. M. T. Velu and D.N. Lambeth, J. Appl. Phys. **69**, 5175 (1991).

[8]. E. M. T. Velu and D.N. Lambeth, IEEE Trans. Magn. **28**, 3249 (1992).

[9]. Y. Liu, B.W. Robertson, Z. S. Shan, S. Malhotra, M. J. Yu, S. K. Renukunta, S. H. Liou and D. J. Sellmyer, IEEE Trans. Magn. **30**, 4035 (1994).

[10]. S. Takei, Y. Otagiri, A. Morisako and M. Matsumoto, J. Appl. Phys. **85**, 6145 (1999).

[11]. M. Benaissa, K. M. Krishnan, E. E. Fullerton and J. S. Jiang, IEEE Trans. Magn. **34**, 1204 (1998).

[12]. J. Ding, Y. Li and P. T. Yong, J. Phys. D: Appl. Phys. **31**, 2745 (1998).

[13]. J. Ding, Y. Li and K.Y. Lee, J. Phys.: Condens. Matter. **10**, 9081 (1998).

[14]. S. Chikazumi, “Physics of Magnetism”, JOHN WILEY & SONS, INC. 249, (1964).

[15]. D. Weller, A. Moser, L. Folks, M. E. Best, W. Lee, M. F. Toney, M. Schwickert, J. Thiele and M. F. Doerner, IEEE Trans. Magn. **36**, 10 (2000).

[16]. J. Ding, Y. Liu, P. G. McCormick and R. Street, J. Magn. Magn. Mater. **123**, L239 (1993).

[17]. E. Kondorsky, J. Phys. USSR **2**, 161 (1940).

[18]. Y. Ishii, J. Appl. Phys. **70**, 3765 (1991).

[19]. P. L. Kim and J. C. Lodder, J. Magn. Magn. Mater. **242–245**, 395 (2002).

[20]. Y. F. Ding, J. S. Chen, E. Liu and J.P. Wang, J. Magn. Magn. Mater. **285**, 443 (2005).

4 Chapter IV $SmCo_5$ thin films with perpendicular anisotropy grown on Cu underlayers

In the previous chapter, $SmCo_5$ thin films with longitudinal anisotropy were successfully prepared by introducing a Cr underlayer. Since $SmCo_5$ thin films with perpendicular anisotropy have attracted increasing attention for perpendicular recording, attempts to create perpendicular anisotropy in $SmCo_5$ thin films were carried out in this chapter.

Copper (Cu) is considered as a possible underlayer to induce a (0001) textured $SmCo_5$ layer based on the small lattice misfit between the (111) lattice of Cu and the (0001) lattice of $SmCo_5$ which is around 2% for the standard samples (as illustrated in Fig. 4.1).

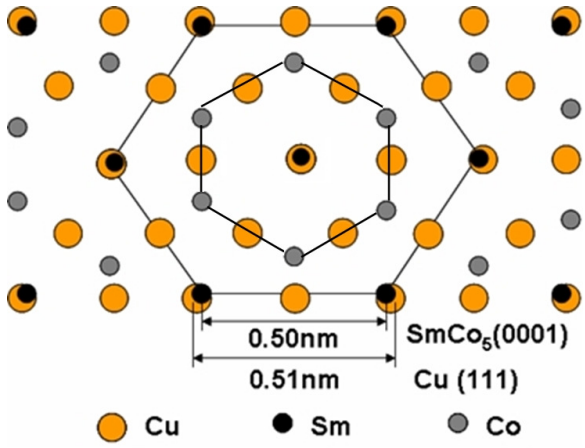

Fig. 4.1. Illustration of lattice matching between Cu (111) and $SmCo_5$ (0001).

The possibility of growing $SmCo_5$ crystallites with perpendicular anisotropy on a Cu underlayer has recently been demonstrated [2-11]. Moreover, it has been studied that the corrosion resistance of $SmCo_5$ film can be significantly improved by the Cu additive and was comparable with previous used CoCr media [7]. The control of the texture and surface morphology of the Cu underlayer plays a key role in obtaining the desired texture and magnetic properties of $SmCo_5$ magnetic layer. However, a good texture requires a certain thickness of Cu and the crystallinity of Cu

needs to be improved [2, 3]. $SmCo_5$ (0001) textured films with perpendicular anisotropy have been obtained on Cu (111) underlayer with a thickness that is greater than 100 nm by sputtering a $SmCo_5$ alloy target and laminating the Co and Sm sub-layers alternatively [2]. However, the texture and perpendicular anisotropy of $SmCo_5$ thin films were poor. It is challenging to decrease the thickness of Cu and maintain good texture and crystallinity at the same time. Sayama et al. reported that the thickness of Cu underlayer can be reduced with a good (111) texture when a titanium (Ti) seed layer is used [4]. Otherwise, a ruthenium (Ru) seed layer can be used to decrease the Cu surface roughness [5]. However, although Cu with good (111) texture has been obtained with either Ti or Ru seed layers, only relatively weak $SmCo_5$ (0001) and $SmCo_5$ (0002) peaks have been observed [4-6].

Table 4.1. Melting temperatures (T_m) and calculated values of surface free energies (γ_i^o) at room temperature of different materials [16].

Material	T_m (^oC)	γ_i^o (Jm^{-2}) (at 298.2K)
Cu	1084	1.934
Ta	2996	3.018
Ti	1660	2.570
W	3410	3.468

A seed layer with high melting point and large surface free energy can help the succeeding layer to form a layer-like structure (as opposed to island-like) with small grains and smooth surface [12-15]. Tantalum (Ta) possessing high melting temperature and surface energy (Table 4.1 [16]) has been reported to improve texture for Co alloys [17] as well as to be an effective diffusion barrier to prevent Cu diffusing into Si and SiO_2 substrates [18, 19]. Therefore, this chapter focuses on the study of Ta seed layers. Cu / Ta dual underlayers were prepared to induce $SmCo_5$ thin

films with large perpendicular anisotropy. The influence of the thickness of the Ta seed layer on the surface morphology and texture of the Cu underlayer, and the influence of the resulting Cu underlayer on the structure and magnetic properties of $SmCo_5$ thin films were studied. The effects of the deposition temperature of $SmCo_5$ layer, the thickness of the Cu underlayer, the thickness and composition of the Sm-Co layer on the structure and magnetic properties of Sm-Co / Cu / Ta films were also systematically investigated. Moreover, at the optimal conditions, titanium (Ti) and tungsten (W) which also have high melting temperature and surface free energy (Table 4.1 [16]) were tried as seed layers for $SmCo_5$ thin films as well.

4.1 Experimental methods

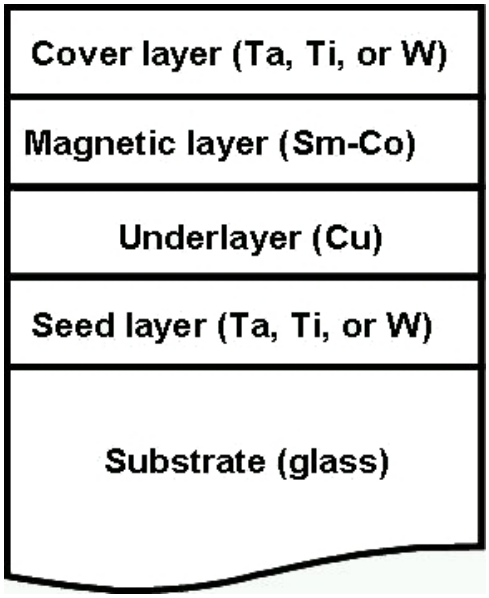

Fig. 4.2. Schematic diagram of multilayer structure.

The film structure studied in this chapter is shown in Fig. 4.2. Six series of experiments were conducted:

(1) To study the effect of the thickness of the Ta seed layer, the thickness of Ta

varied from 0 nm to 50 nm, the thicknesses of the Cu and $SmCo_5$ layers were fixed at 50 nm and 65 nm respectively. The Ta and Cu layers were deposited at room temperature while the $SmCo_5$ layer was deposited at 400 ^oC which is the temperature found to be optimal;

(2) To study the effect of the deposition temperature of $SmCo_5$, $SmCo_5$ (65 nm) / Cu (50 nm) / Ta (4 nm) films were prepared. Cu / Ta underlayers were deposited at room temperature and $SmCo_5$ layers were deposited at a temperature ranging from 300 ^oC to 450 ^oC;

(3) To study the effect of the thickness of the Cu underlayer, $SmCo_5$ (65 nm) / Cu (15 ~ 100 nm) / Ta (4 nm) films were prepared;

(4) To study the effect of the thickness of the $SmCo_5$ layer, $SmCo_5$ (20 ~90 nm) / Cu (50 nm) / Ta (4 nm) films were prepared;

(5) To study the effect of the composition of the Sm-Co layer, Sm-Co layer with a composition from $Sm_{13}Co_{87}$ to $Sm_{37}Co_{63}$ were fabricated;

(6) To study the effect of different seed layers (Ti and W), $SmCo_5$ (65 nm) / Cu (50 nm) / Ti or W (4 nm) films were prepared.

Except in (5), the atomic ratio of Sm/Co in the Sm-Co layer was controlled to be 1:5 by adjusting the sputtering rate of the two targets as discussed in Chapter 3. A 20 nm cover layer was deposited to protect $SmCo_5$ from oxidization. Here the same material for seed layer and cover layer were used because of the limited targets positions in the sputtering chamber employed. Cu can be deposited at room temperature since it naturally forms the (111) texture which is this close-packed plane thus having the lowest surface energy. Moreover, room temperature is favorable for industrial applications and results in a smoother surface of Cu [5].

4.2 Growth of Cu underlayer on Ta seed layer on glass substrate

4.2.1 Growth of Ta seed layer

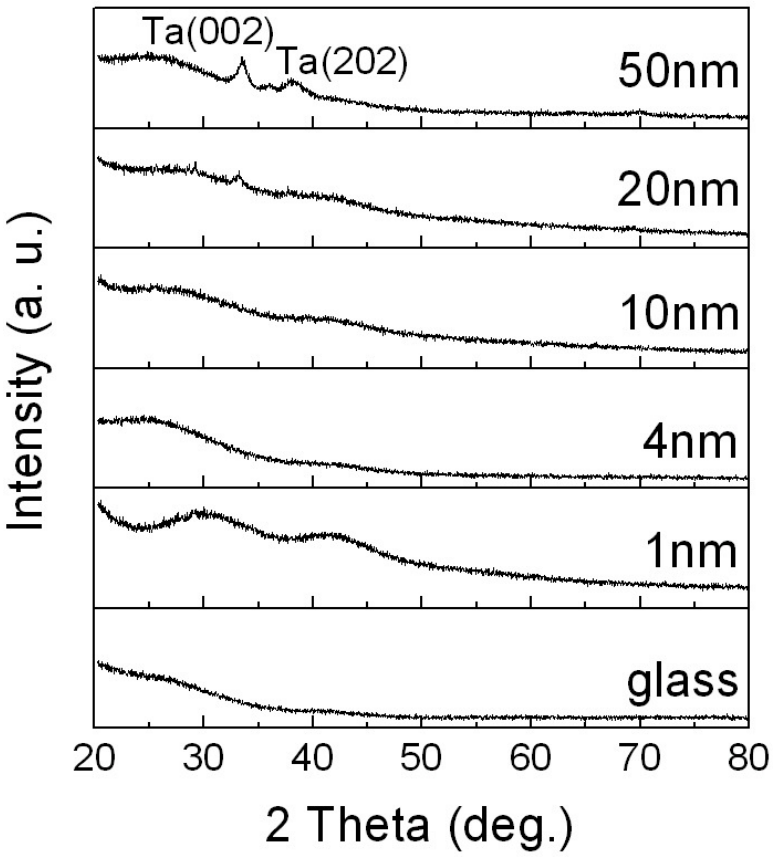

Fig. 4.3. θ-2θ XRD spectra of Ta films with different thicknesses (0-50 nm).

Pure Ta films with different thicknesses of 1 nm, 4 nm, 10 nm, 20 nm and 50 nm were deposited on glass substrates at room temperature. Then 50 nm Cu films were grown at room temperature on Ta films with different thicknesses of 0nm, 1 nm, 4 nm, 10 nm, 20 nm and 50 nm.

Fig. 4.3 shows the conventional θ-2θ XRD spectra of Ta seed layers with different thicknesses. There is no peak observed for the Ta films with a thickness of

10 nm or below which indicates a disordered structure in these Ta films (amorphous-like). For the 20 nm Ta film, the β-Ta (002) peak begins to appear, indicating the beginning of crystallization. For the 50 nm Ta film, both the β-Ta (002) and (202) peaks appear and the peaks intensities increase. It implies that the crystallization is enhanced.

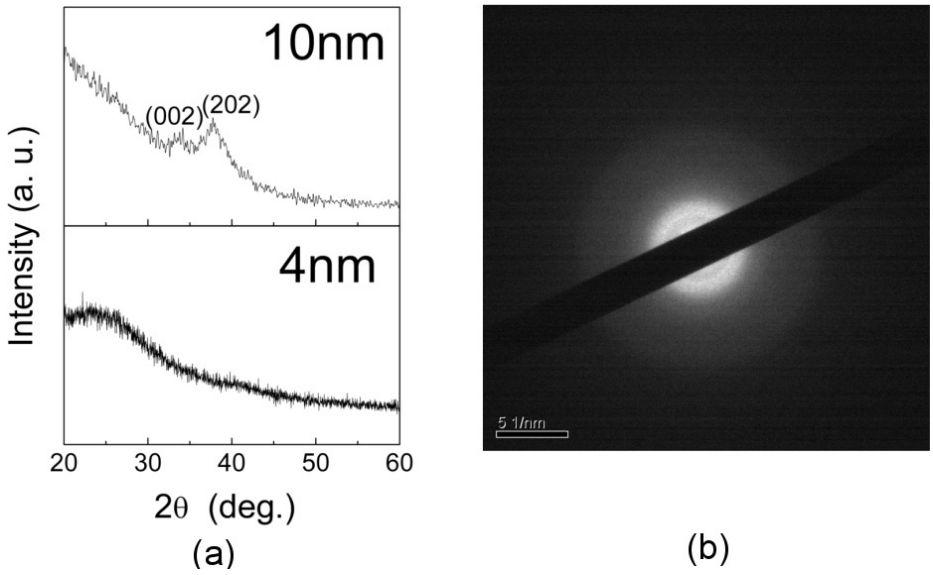

Fig. 4.4. (a) Glancing angle XRD spectra of 4 nm and 10 nm Ta films measured at a fixed 0.5° incidence angle. (b) The electron diffraction pattern of the 4 nm Ta film.

The XRD intensity is dependent on the film thickness in the θ-2θ mode. Therefore, a careful glancing angle XRD study was performed to examine these thin films (≤10 nm) with a scan time of more than 20 hours. The results are shown in Fig. 4.4a. β-Ta (002) and (202) peaks are observed in the Ta film with a thickness of 10 nm, whereas no peak can be seen in the Ta film with a thickness of 4 nm. It indicates that the Ta film of 10 nm is crystallized (it might be a mixture of crystalline and amorphous phases) and the 4 nm Ta film stays in the disordered (amorphous-like) state. The electron diffraction pattern of the Ta film of 4 nm shows amorphous ring which further confirms the amorphous state in the Ta film of 4 nm (shown in Fig.

4.4b). Here the metastable tetragonal β-Ta phase (a=0.534 nm, c=0.994 nm) was observed rather than the bcc structure of α-Ta (a=0.33058 nm) in thicker Ta films ($\geq$10 nm) after deposition at room temperature. It has been reported that metastable β-Ta is often formed on corning glass [18, 20, 21]. Hieber and Mayer reported that β phase transforms into stable α phase after a post-annealing at elevated temperatures for thicker Ta films [21].

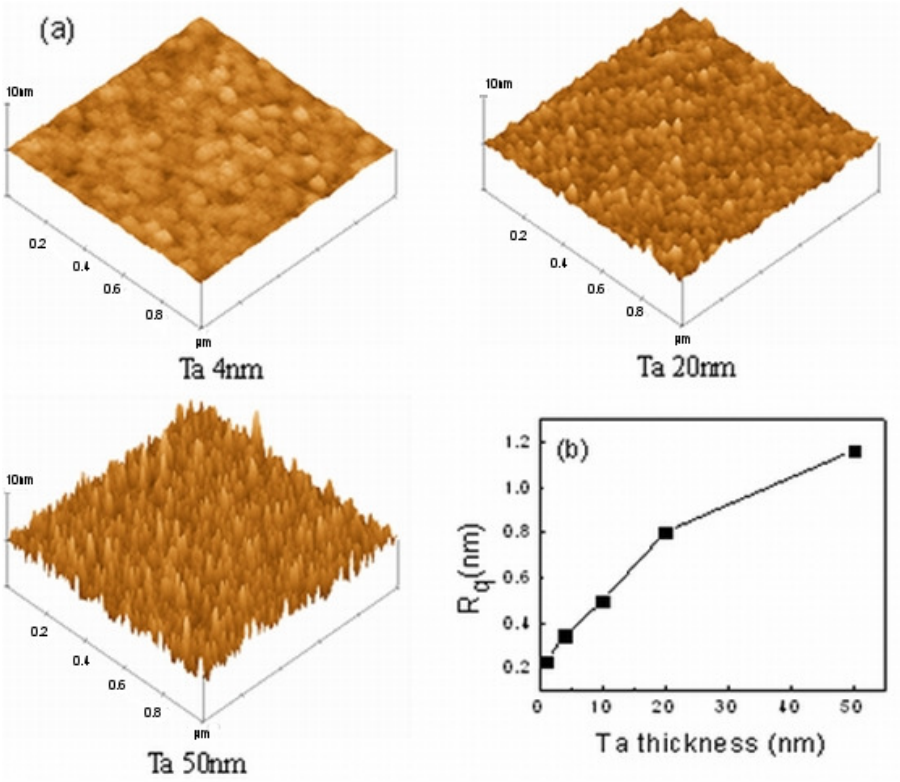

Fig. 4.5. (a) AFM images of Ta films with different thicknesses (4 nm, 20 nm and 50 nm). (b) The changes of roughness as a function of film thickness.

The AFM images of Ta films with different thicknesses are shown in Fig. 4.5a. It can be seen that the Ta film of 4 nm shows a very smooth surface. On the other hand, the thicker Ta films with higher crystallization degree show rougher surface. The dependence of surface root-mean-square roughness (R_q) on the thickness of films is plotted in Fig. 4.5b. The surface roughness continually increases in thicker

films.

4.2.2 Growth of Cu on Ta seed layer

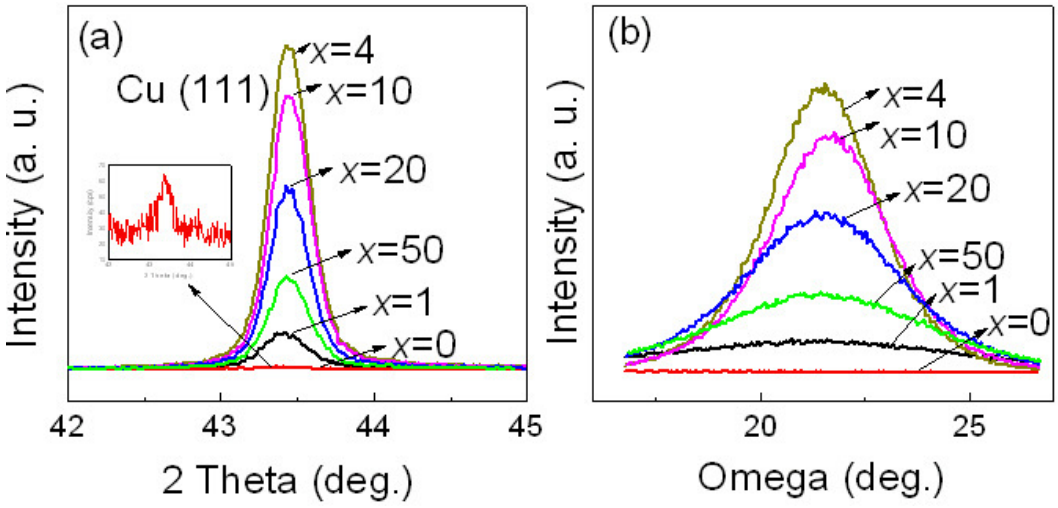

Fig. 4.6. (a) θ-2θ XRD spectra of Cu films grown on Ta seed layer of different thicknesses (0-50 nm). (Inset is XRD spectrum of Cu film without Ta seed layer). (b) Rocking curves (ω scan) of 50 nm Cu films grown on Ta seed layer of different thicknesses (0-50 nm).

The thickness of Cu was fixed to be 50 nm in this work, and the Cu underlayer was deposited at room temperature. For fcc structured Cu, (111) is its close packed plane which has the lowest surface energy. Therefore, Cu films tend to have a (111) texture. From Fig. 4.6a, it can be seen that (111) peaks appear in all of the Cu films no matter with or without Ta seed layers. However, the intensities of the (111) peaks vary significantly. The Cu film grown directly on glass shows a very weak (111) peak which indicates a poor crystallinity or/and a poor texture. On the other hand, the Cu film grown on a 4 nm Ta seed layer shows a clear peak with strong intensity. This indicates that the Cu film has good crystallinity and probably a good texture. In order to examine the texture quality, X-ray rocking curve analysis (ω scan) of Cu (111) peak was conducted. From Fig. 4.6b, it can be seen that the full width at half

maximum of the rocking curve ($\Delta\theta_{50}$) of Cu film grown directly on glass substrate is undetectable within the measurement range of 20°. A broad peak appears when there is a Ta seed layer of 1 nm. The sharpest $\Delta\theta_{50}$ peak is found at the Ta seed layer with a thickness of 4 nm. And with thicker Ta seed layers, θ_{50} of Cu (111) increases considerably.

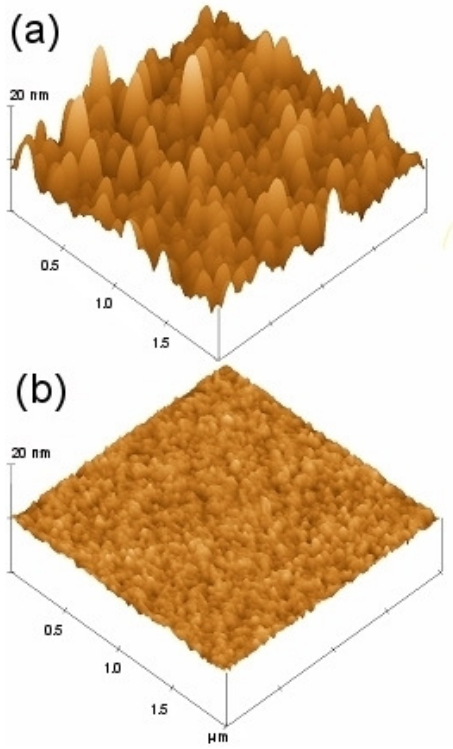

Fig. 4.7. AFM images of 50 nm Cu films grown on (a) glass and (b) 4 nm Ta coated glass substrates.

Fig. 4.7 shows the AFM images of Cu films grown on 0 nm or 4 nm Ta seed layers. The surface roughness R_q of Cu reduced from 4.3 nm to 0.5 nm when a 4 nm Ta seed layer is added. Moreover, the Cu film has a smaller particle size when grown on a 4 nm Ta seed layer compared to that grown directly on glass substrate.

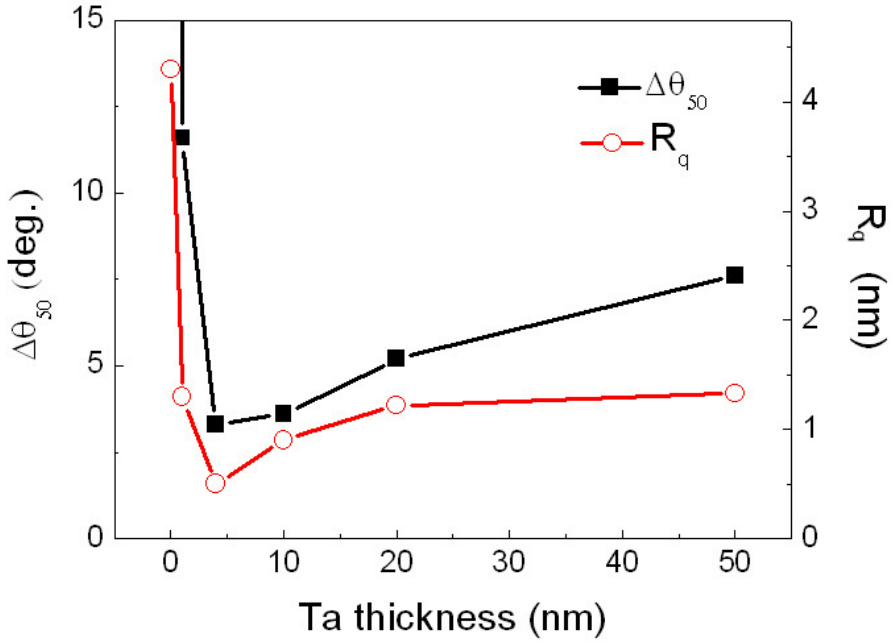

Fig. 4.8. Dependence of $\Delta\theta_{50}$ and R_q of 50 nm Cu films on the thicknesses of Ta seed layer.

The changes in $\Delta\theta_{50}$ of Cu (111) peak and the surface root-mean-square roughness (R_q) of 50nm Cu films are plotted in Fig. 4.8 as a function of underlying Ta layer thickness. $\Delta\theta_{50}$ and R_q show the similar trend: they decrease significantly from 0 nm Ta to 4 nm Ta and then increase slowly from 4 nm Ta to 50 nm Ta. The best texture and smoothness of Cu films happen for a 4 nm Ta seed layer. The $\Delta\theta_{50}$ of Cu (111) peak and the R_q of Cu surface are as small as 3.9° and 0.5 nm, respectively. These results indicate that with addition of Ta seed layer, the texture and surface roughness of Cu films are effectively improved and the improvement depends on the thickness of Ta seed layer.

There is no epitaxial relationship between β-Ta and Cu. The possible reason for the significant improvements in the texture, crystallinity and smoothness of Cu film on Ta seed layer could be explained by surface free energy and kinetic effects. Cu has relatively low melting point and surface free energy compared to those of Ta

seed layer (Table 4.1). It has been noticed that Cu is hard to wet on glass substrate because of the small surface free energy, as shown by poor adhesion. It is possible that Cu forms three-dimensional islands or clusters at the initial stage on glass substrate. Therefore, the following growth of Cu tends to have a random orientation distribution and rough surface. On the other hand, due to the large surface energy of Ta layer, Ta seed layer tends to soon cover the substrate surface and forms layer-like film with a smooth surface [18]. The wetting of Cu is favorable on Ta seed layer. Cu is strongly adhesive to the Ta layer. It is likely that Cu formed two-dimensional flat islands with a (111) preferred orientation at the initial stage. Then the oriented islands impinge on each other and a highly textured polycrystalline (111) Cu film forms. If the Ta seed layer is only 1 nm thick, the film may not fully cover the glass substrate. If the thickness of the Ta seed layer is 10 nm or larger, larger grain size and greater roughness of the Ta seed layer may cause the decline of the quality of the Cu layer. Therefore, the greatest improvements of Cu texture and surface smoothness appear with a 4 nm Ta seed layer.

4.3 Fabrication of $SmCo_5$ films with Cu / Ta dual underlayer on glass substrate and study of their structure and magnetic properties

4.3.1 Effect of thickness of Ta

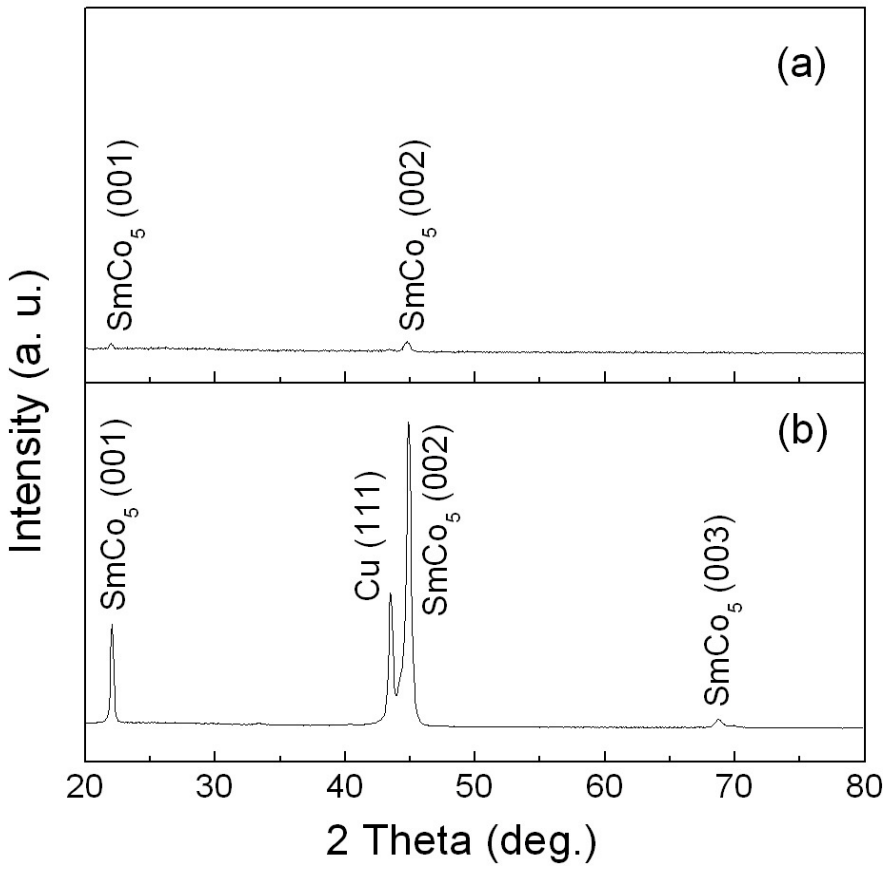

Fig. 4.9. XRD spectra of 65 nm $SmCo_5$ films grown on (a) glass and (b) a 4 nm Ta coated glass substrates.

$SmCo_5$ films with a fixed thickness of 65 nm were deposited at a constant temperature of 400 °C on Cu (50 nm) / Ta (0-50 nm) underlayers. 400 °C is the optimized deposition temperature for $SmCo_5$ film as discussed in the next section. The XRD spectra of the samples grown on glass and 4nm Ta coated glass substrates,

respectively, are shown in Fig. 4.9a and b. For the sample without a Ta seed layer, the integrated intensity of the $SmCo_5$ (0001) and $SmCo_5$ (0002) peaks are only 17.5 and 59.2 (counts per second). $\Delta\theta_{50}$ is undetectable when measuring in 20° range. On the other hand, for the sample with a 4 nm Ta seed layer, the integrated intensity of the $SmCo_5$ (0001) and $SmCo_5$ (0002) peaks significantly increase to 298 and 1556 (counts per second). The $\Delta\theta_{50}$ of $SmCo_5$ (0001) and $SmCo_5$ (0002) peaks are 3.4° and 3.2°, respectively. A $SmCo_5$ (0003) reflection peak is also observed. It indicates a good crystallinity and texture in the $SmCo_5$ film grown on the Cu (50 nm) / Ta (4 nm) underlayer. With thicker Ta seed layers, $\Delta\theta_{50}$ of $SmCo_5$ (0001) and $SmCo_5$ (0002) peaks increases, showing similar trend as those of Cu (111) peaks (Fig. 4.8).

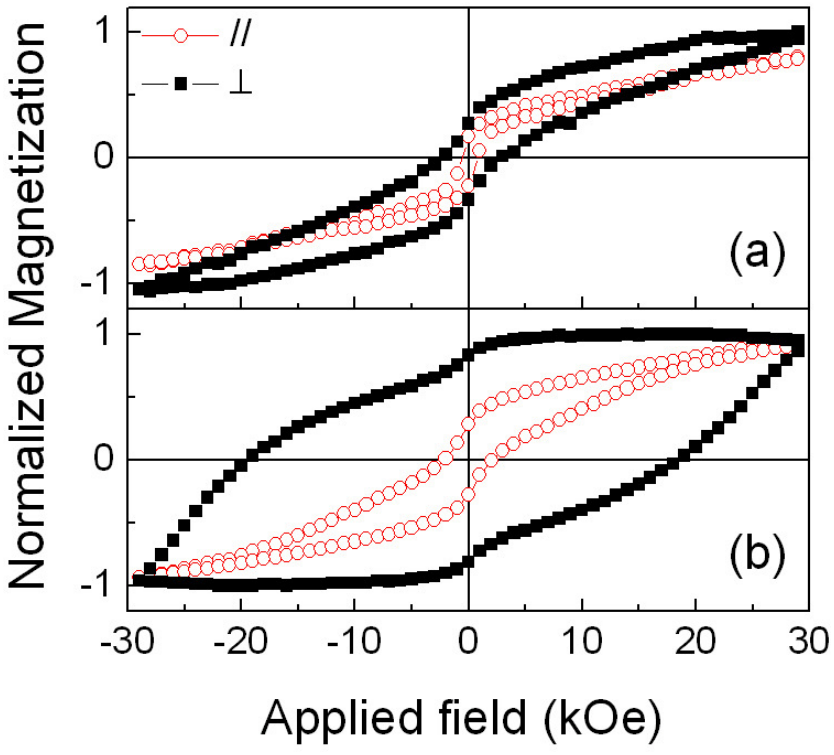

Fig. 4.10. M-H loops of the samples (a) without seed layer and (b) with a 4 nmTa seed layer.

It has been found that all the samples show perpendicular anisotropy. The M-H loops of $SmCo_5$ thin films grown on Cu underlayer without and with a 4nm Ta seed layer are shown in Fig. 4.10. For the sample without Ta seed layer, the out-of-plane and in-plane ${}_iH_c$ are 2.5 kOe and 0.5 kOe, respectively. By introducing a thin Ta seed layer, the out-of-plane ${}_iH_c$ of the $SmCo_5$ dramatically increases to 19.5 kOe which is much higher than that of the reported $SmCo_5$ thin film fabricated by laminating Sm and Co sublayer alternatively [4]. The in-plane coercivity somewhat increased to 2.3 kOe. A kink is observed in the out-of-plane M-H loop of the $SmCo_5$ thin film with a Ta seed layer. It implies that a small amount of soft magnetic phase which could be the amorphous Sm-Co phase exists in the hard magnetic $SmCo_5$ thin films. The inhomogeneity causes the non-uniform demagnetization.

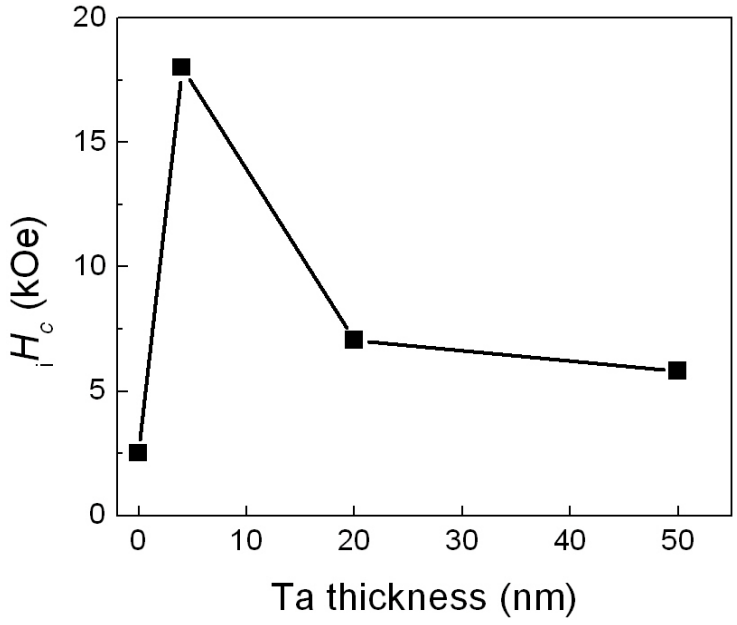

Fig. 4.11. Dependence of out-of-plane ${}_iH_c$ of $SmCo_5$ on the thickness of Ta seed layer.

The out-of-plane ${}_iH_c$ of $SmCo_5$ films as a function of the thickness of Ta seed layer is shown in Fig. 4.11. The trend is consistent with that of $SmCo_5$ (0001) texture,

as a larger out-of-plane ${}_iH_c$ corresponds to a smaller $\Delta\theta_{50}$.

These results indicate that a Cu / Ta dual underlayer with a good Cu (111) texture and smooth surface offers excellent template for the granular epitaxial growth of $SmCo_5$. Thus it leads to a good crystallinity and good (0001) texture of $SmCo_5$. This desired crystallographic structure of $SmCo_5$ films results in large perpendicular anisotropy and perpendicular coercivity.

4.3.2 Study of Cu diffusion

It is to note that in Fig. 4.9 the (0001) and (0002) peaks of $SmCo_5$ shift to a smaller 2θ angle compared to standard bulk $SmCo_5$. Table 4.2 lists the 2θ positions of (0002) peaks and the calculated lattice constants of a and c of standard $SmCo_5$, $SmCo_{3.3}Cu_{1.7}$, $SmCu_5$ powder samples and my samples. It can be seen that the $SmCo_5$ (0002) peak of my sample is located at 44.8^o which is close to that of $SmCo_{3.3}Cu_{1.7}$. Since the atomic radius of Cu (1.28 Å) is slightly larger than that of Co (1.25 Å), when a Cu atom substitutes a Co atom, the lattice constant would expand and 2θ would shift to a smaller angle. The peak shifts towards a smaller angle indicating that an amount of the Co atoms in $SmCo_5$ are replaced by Cu atoms. A cross sectional TEM sample of the $SmCo_5$ / Cu / Ta was prepared for the Nanobeam EDX analysis. The EDX analysis of the $SmCo_5$ layer shows a composition of $SmCo_3Cu_{2.1}$ (Fig. 4.12). It proves the Cu diffusion into the $SmCo_5$ layer. Similar results have been reported by Takahashi *et al.* [6] who proved by energy filtered elemental map that the diffusion of Cu into the Sm-Co layer forms a $Sm(Co, Cu)_5$ solid solution. Sayama et al. states that the formation of a $Sm(Co, Cu)_5$ alloy favors good crystallinity and large perpendicular anisotropy [7].

Table 4.2. The positions of SmCo(Cu) (0002) peak in θ - 2 θ XRD spectra and the lattice constants a and c. The values for $SmCo_5$, $SmCo_{3.3}Cu_{1.7}$, $SmCu_5$ are based on PDF File No. 35-1400, No. 23-934 and No. 65-933, respectively.

	2θ (0002) (°)	a (Å)	c (Å)
$SmCo_5$	45.61	4.995	3.978
$SmCo_{3.3}Cu_{1.7}$	45.00	5.006	4.018
$SmCu_5$	44.12	5.080	4.100
My sample	**44.80**	--	**4.027**

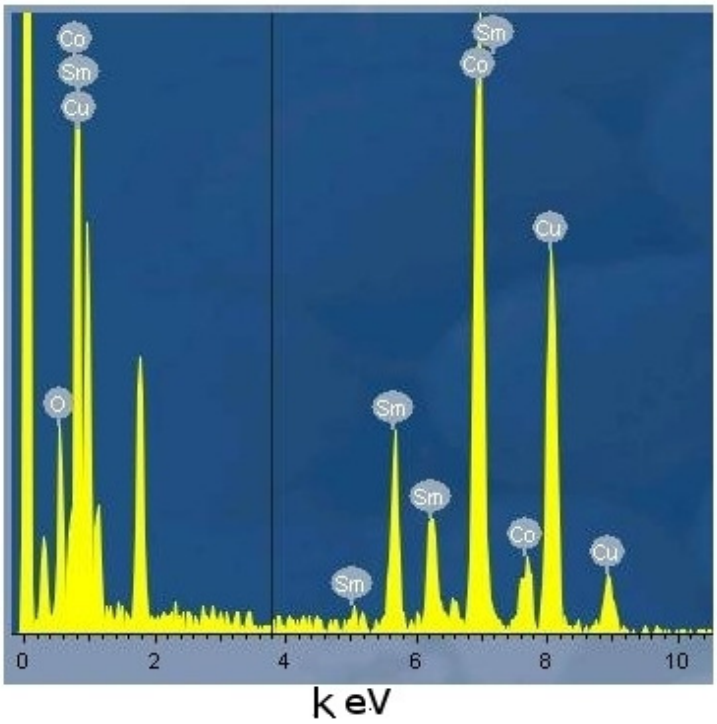

Fig. 4.12. EDX spectrum of the $SmCo_5$ layer.

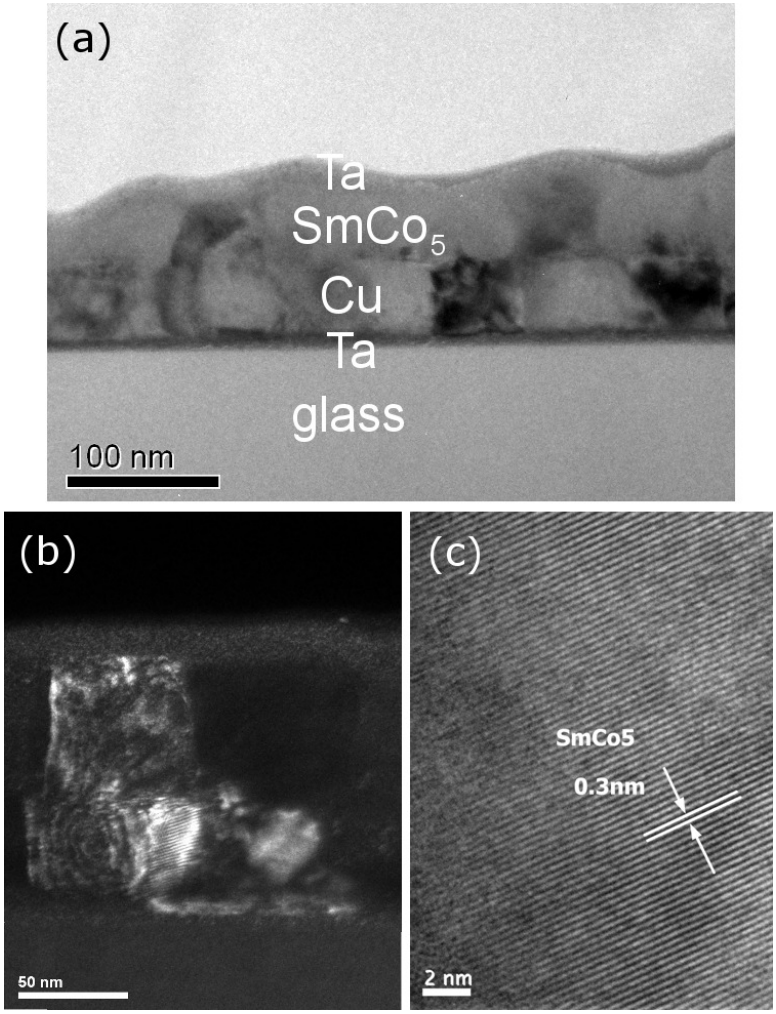

Fig. 4.13. (a) TEM bright field image, (b) dark field image and (c) high resolution image of cross sectional sample of Ta (20 nm) / $SmCo_5$ (65 nm) / Cu (50 nm) / Ta (4 nm).

Fig. 4.13 shows the TEM bright field image, dark field image and high resolution (HRTEM) image of the cross sectional sample of the Ta (20 nm) / $SmCo_5$ (65 nm) / Cu (50 nm) / Ta (4 nm) thin film. The multilayer structure is clearly observed in the bright field image. The dark field image indicates that the grain size of $SmCo_5$ and Cu are both around 60 nm. In the HRTEM image, the lattice fringes with an inter-fringe spacing of 0.3 nm are clearly observed in the $SmCo_5$ layer. This spacing is close to the inter-plane distance of the $(11\bar{2}0)$ planes in hcp-structured

$SmCo_5$. Because the $(11\bar{2}0)$ planes is perpendicular to the (0001) plane in $SmCo_5$, the $(11\bar{2}0)$ planes should be observed in the cross-sectional (0001) textured $SmCo_5$ sample. This result further confirms the (0001) texture and indicates a good crystallinity of the $SmCo_5$ phase.

4.3.3 Effect of deposition temperature of $SmCo_5$ layer

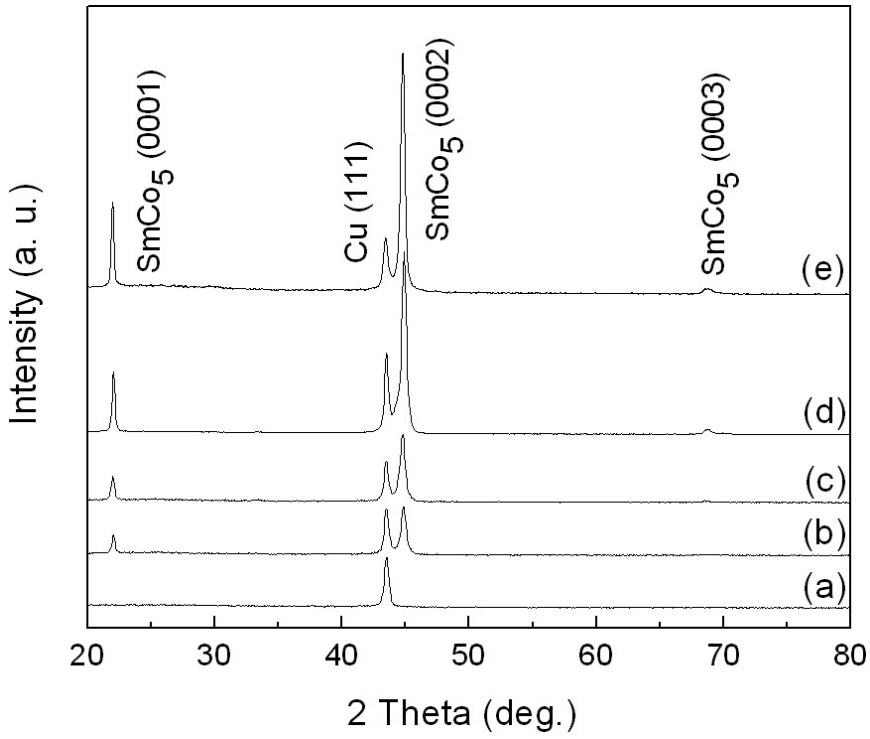

Fig. 4.14. XRD spectra of the samples with $SmCo_5$ layer deposited at different temperatures of (a) 300 ^oC; (b) 325 ^oC; (c) 350 ^oC; (d) 400 ^oC and (e) 450 ^oC.

The temperature dependence of the crystallization of $SmCo_5$ phase and (0001) texture was investigated when a 4-nm Ta seed layer and a 50-nm Cu underlayer were used. Fig. 4.14 shows the XRD spectra of the samples with $SmCo_5$ layers deposited at various temperatures. At 300 ^oC, no $SmCo_5$ (0001) or (0002) peak is observed, suggesting either that the Sm-Co film is amorphous or that the grain size is too small

to be detected. At 325 °C, sharp $SmCo_5$ (0001) and (0002) diffraction peaks are observed. At 350 °C, a small $SmCo_5$ (0003) peak starts to appear in the XRD spectrum. The integrated intensity of both $SmCo_5$ (000l) and (0002) diffraction peaks increases at elevated temperatures. The $\Delta\theta_{50}$ of the $SmCo_5$ (0001) peak decreases monotonically from 4.4° to 3.1° with the increase of the temperature from 325 °C to 450 °C. These results indicate that the crystallization of $SmCo_5$ has already occurred at the temperature of 325 °C and the (0001) texture and crystallinity of $SmCo_5$ films are improved by elevating the temperature. The intensity of the Cu (111) diffraction peak slightly increases and the $\Delta\theta_{50}$ of the Cu (111) peak decreases from 6.5° to 3.8° with the increase in temperature from 300 °C to 450 °C. It may be attributed to the post-annealing effect on Cu underlayers occurring during the increase in temperature from room temperature to the different target temperatures. Besides the temperature effect on the crystallization and texture improvement of $SmCo_5$, the post-annealing effect improves the (111) texture of the Cu underlayer. Moreover, the degree of Cu diffusion into the $SmCo_5$ layer increases with the temperature. The two above reasons may also contribute to the improvement in crystallization and texture of $SmCo_5$ films.

Fig. 4.15 shows the corresponding M-H loops of $SmCo_5$ thin film deposited at different temperatures. Results indicate that the in-plane and out-of-plane $_iH_c$ of $SmCo_5$ films strongly depend on the deposition temperature of the $SmCo_5$ layer. After deposition at 300 °C, the $SmCo_5$ film possesses an amorphous-like structure and shows isotropic magnetic properties. Both in-plane and out-of-plane $_iH_c$ are around 7.7 kOe. Perpendicular anisotropy appears in the film deposited at 325 °C, when the crystalline $SmCo_5$ phase with the (0001) texture is found in the XRD examination (Fig. 4.14). The out-of-plane $_iH_c$ increases from 7.6 kOe to 19.5 kOe

when the temperature increases from 325 °C to 400 °C. This corresponds to a better crystallinity and (0001) texture of $SmCo_5$. However, the out-of-plane ${}_iH_c$ of $SmCo_5$ film drops significantly to 2.3 kOe after deposition at 450 °C. This is probably due to the increased grain size of $SmCo_5$ and heavier Cu diffusion. The average grain size of $SmCo_5$ increased from 45 nm to 53 nm with the increase of the deposition temperature from 400 °C to 450 °C based on the XRD results (calculated from $SmCo_5$ (0001) peak using the Scherrer's equation).

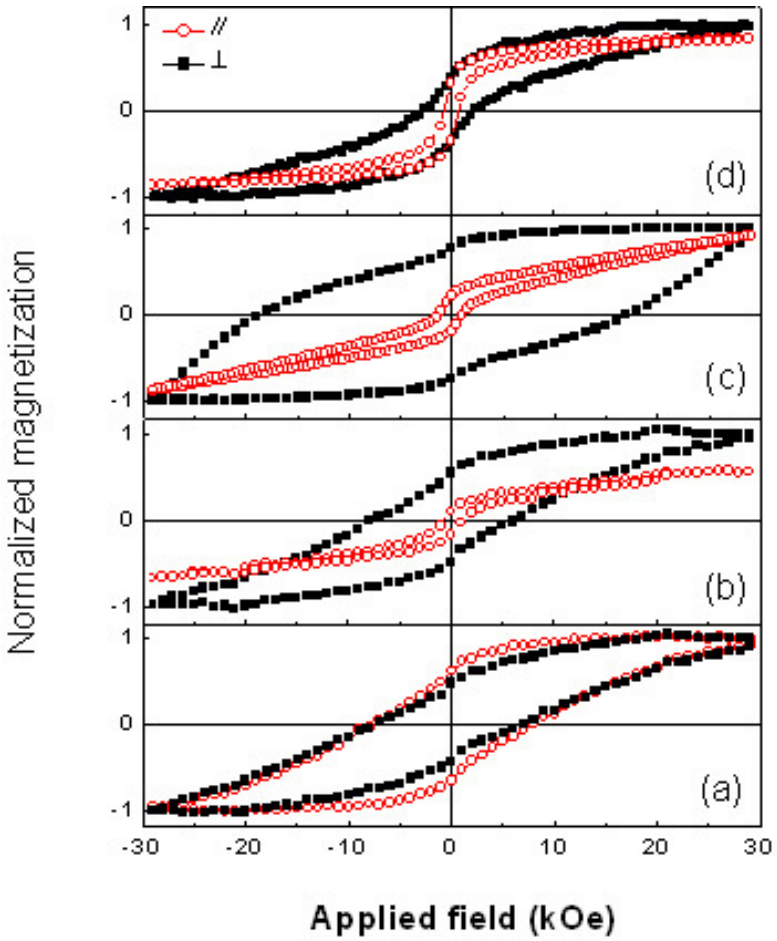

Fig. 4.15. M-H loops of the samples with $SmCo_5$ layers deposited at different temperatures of (a) 300 °C; (b) 325 °C; (c) 400 °C and (d) 450 °C.

From the above results, it can be seen that 400 °C is the optimal deposition temperature for the $SmCo_5$ layer, thus the deposition temperature was fixed at

400 ^oC for $SmCo_5$ layers in the following studies.

4.3.4 Effect of thickness of Cu underlayer

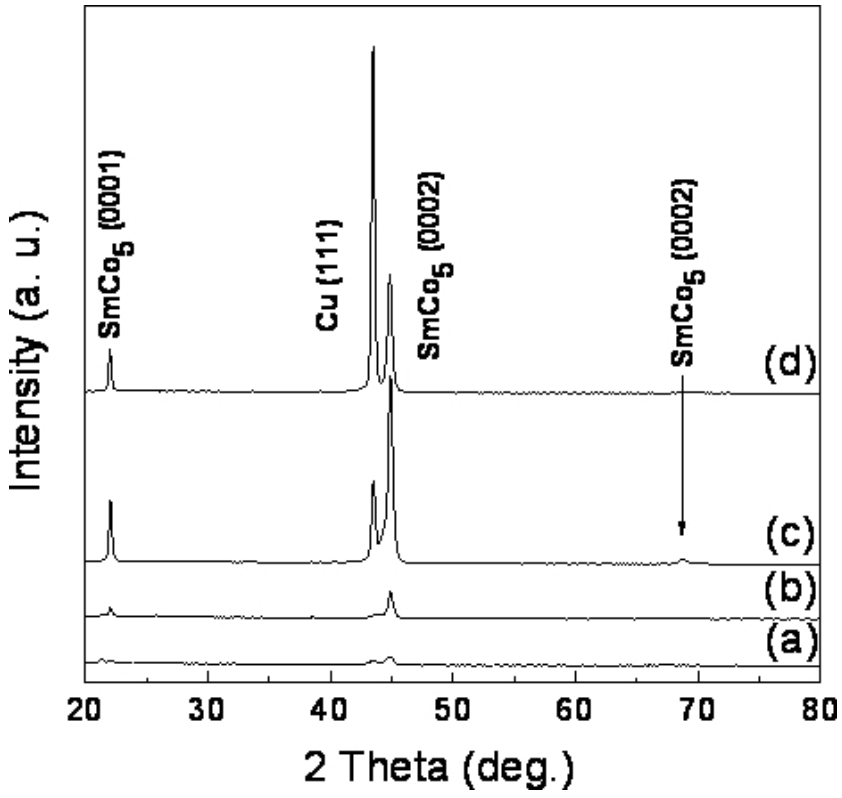

Fig. 4.16. XRD spectra of Ta / $SmCo_5$ / Cu / Ta thin films with (a) a 15 nm Cu underlayer, (b) a 25 nm Cu underlayer, (c) a 50 nm Cu underlayer and (d) a 100 nm Cu underlayer.

I investigated the effect of the thickness of the Cu underlayer on the magnetic properties of $SmCo_5$ films. As shown in Fig. 4.16, the $SmCo_5$ film deposited on the Cu underlayer with a thickness of 15 nm shows a poor crystallinity, indicated by a weak and broad (0002) peak. With the increasing thickness of Cu underlayers, $SmCo_5$ films show improved crystallinity and texture. Strong $SmCo_5$ (0001) and (0002) peaks are clearly observed for $SmCo_5$ films grown on the 50 nm and 100 nm Cu underlayers. The $\Delta\theta_{50}$ values of the Cu (111) peak and $SmCo_5$ (0002) peak are

summarized in Table 4.3. The continuous decrease in the $\Delta\theta_{50}$ of $SmCo_5$ (0002) peaks is consistent with the decrease of the $\Delta\theta_{50}$ of Cu (111) peaks, which indirectly demonstrates the granular epitaxial growth of $SmCo_5$ on Cu (111) underlayers. The integrated intensity of the Cu (111) peak increases with the increase of thickness. However, the integrated intensity of the $SmCo_5$ (0002) peak does not monotonically increase when the thickness of Cu is larger than 50 nm. This is probably due to a deteriorated surface roughness of the 100 nm Cu underlayer (R_q=1.1 nm) compared with the one of the 50 nm Cu underlayer (R_q=0.5 nm) which in turn influenced the crystallinity of $SmCo_5$ phase.

Fig. 4.17 summarizes the in-plane and out-of-plane ${}_iH_c$ for $SmCo_5$ films which were deposited on Cu underlayers with different thicknesses in the range of 15-100 nm. It can be seen that 50 nm is the optimal thickness for the Cu underlayer. The out-of-plane ${}_iH_c$ of $SmCo_5$ film reaches its maximum value with a 50 nm Cu underlayer. The results indicate that the crystallinity of $SmCo_5$ plays an important role in the magnetic properties of $SmCo_5$ films.

Table 4.3. $\Delta\theta_{50}$ of Cu (111) peak and $SmCo_5$ (0002) peak of Ta / Sm-Co / Cu / Ta thin films with different Cu thicknesses.

Thickness of Cu (nm)	$\Delta\theta_{50}$ of Cu (111) (^{o})	$\Delta\theta_{50}$ of $SmCo_5$(0002) (^{o})
15	10.5	10.2
25	9.0	3.4
50	3.9	3.2
100	2.9	3.0

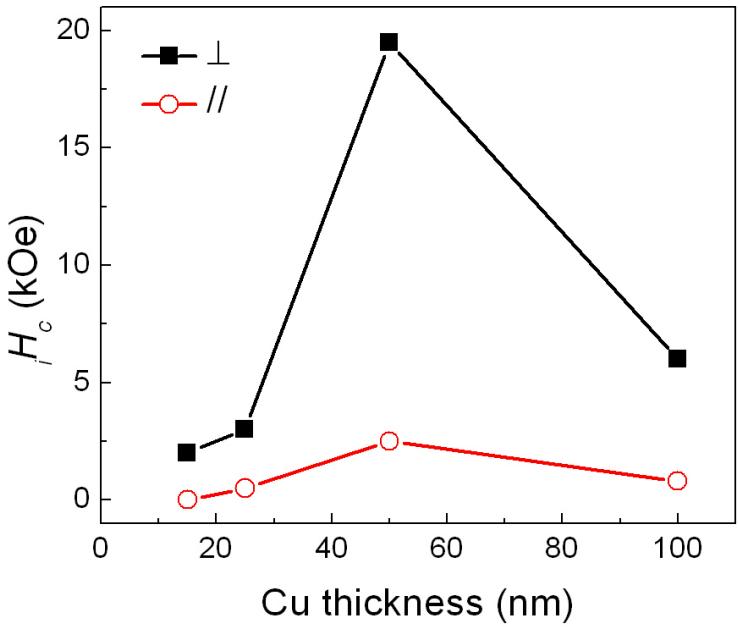

Fig. 4.17. Dependence of in-plane and out-of-plane $_iH_c$ in SmCo$_5$ films on the thickness of Cu underlayer.

4.3.5 Effect of thickness of SmCo$_5$ layer

In this study, the effect of the thickness of SmCo$_5$ layer on the magnetic properties of SmCo$_5$ films is investigated. SmCo$_5$ films with thicknesses ranging from 20 to 90nm were prepared on Cu (50 nm) / Ta (4 nm) underlayer at 400 °C. The XRD spectra for these samples are shown in Fig. 4.18. With the increasing thickness, the intensities of SmCo$_5$ (0001) and (0002) peaks continuously increase. Although the film thickness can affect the peak intensity, the much higher intensities in the SmCo$_5$ films with a thickness of 65nm and 90 nm imply improved crystallinities. Moreover, the $\Delta\theta_{50}$ of SmCo$_5$ (0001) and (0002) continuously decrease in the thicker SmCo$_5$ films indicating an improved (0001) texture as shown in Table 4.4.

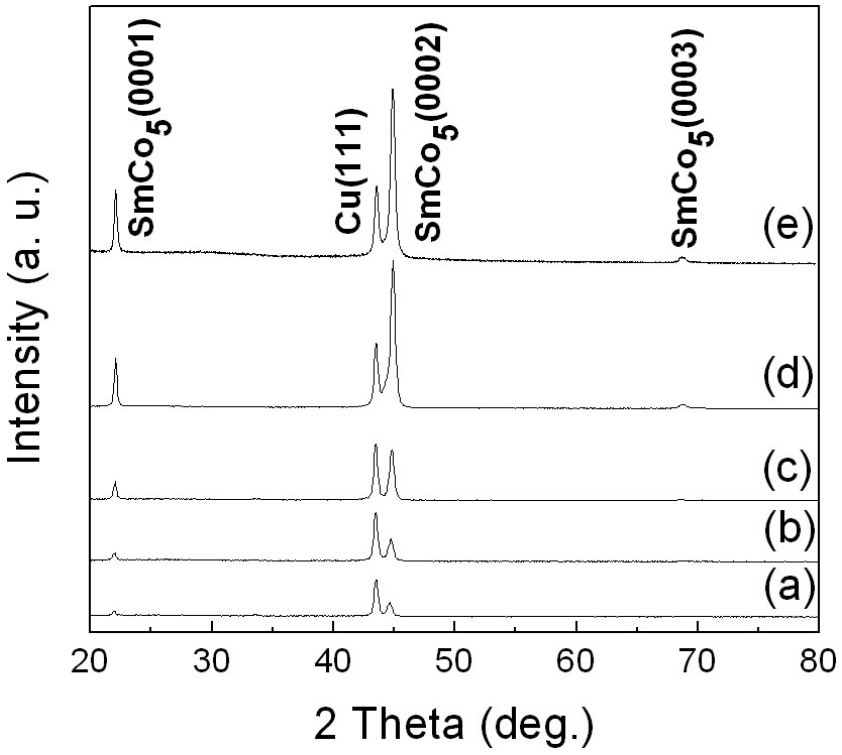

Fig. 4.18. XRD spectra of Ta (20 nm) / $SmCo_5$ (*t* nm) / Cu (50 nm) / Ta (4 nm) thin films: (a) *t*=23 nm, (b) *t*=35 nm, (c) *t*=45 nm, (d) *t*=65 nm and (e) *t*=90 nm.

Table 4.4. $\Delta\theta_{50}$ of $SmCo_5$ (0001) peak and $SmCo_5$ (0002) peak in $SmCo_5$ films with different thicknesses.

Thickness of $SmCo_5$ (nm)	$\Delta\theta_{50}$ of Cu (111) (^{o})	$\Delta\theta_{50}$ of $SmCo_5$(0002) (^{o})
23	11.1	5.6
35	10.2	4.8
45	3.8	3.5
65	3.4	3.2
90	3.2	3.1

The out-of-plane and in-plane ${}_iH_c$ as a function of the thickness of the $SmCo_5$ film is summarized in Fig. 4.19. All the $SmCo_5$ films show perpendicular anisotropy. The out-of-plane ${}_iH_c$ and perpendicular anisotropy increase with the increasing $SmCo_5$ film thickness. The increase of the out-of-plane ${}_iH_c$ is again due to the

improvement of the crystallinity and a better texture of $SmCo_5$ (0001).

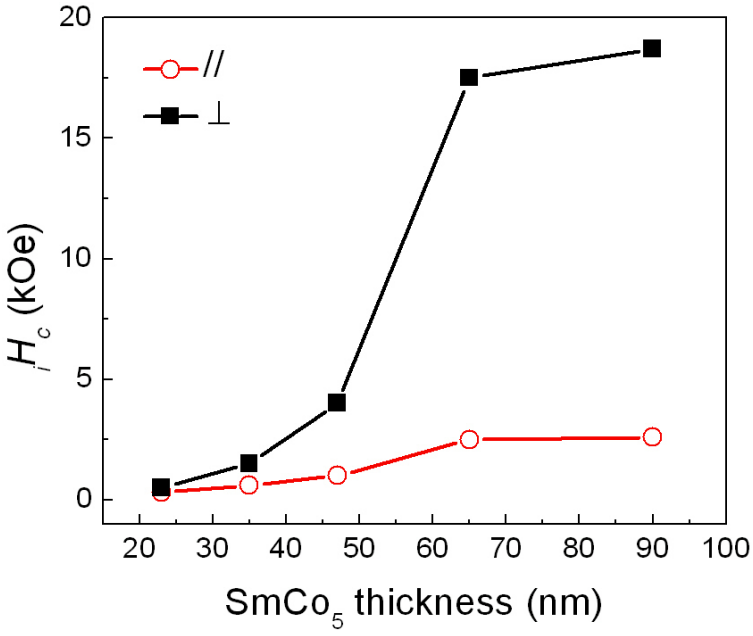

Fig. 4.19. Dependence of in-plane and out-of-plane intrinsic coercivity in $SmCo_5$ films on the thickness of $SmCo_5$ layer.

4.3.6 Effect of Sm / Co composition

Fig. 4.20 shows the XRD spectra of Sm-Co films grown on Cu (50 nm) / Ta (4 nm) underlayers with different Sm-Co compositions where the atomic percentage of Sm varies from 13.2 at.% to 37.0 at.%. The peaks of Cu (111), $SmCo_5$ (0001) and $SmCo_5$ (0002) are clearly observed in all the films and no other crystalline peak could be observed. It indicates that a crystallographic (111) texture forms in 50 nm Cu underlayers, that a crystallographic (0001) texture forms in 65 nm $SmCo_5$ magnetic layers and 4 nm Ta seed layers and that 20 nm Ta cover layers stay in amorphous like structure. Surprisingly, the respective positions of $SmCo_5$ (0001) and (0002) peaks for different samples remain the same despite the Sm-Co composition varying in a large range. It implies that $SmCo_5$ is the preferable phase to form in all the films. However, the intensities of the $SmCo_5$ (0001) and (0002) peaks vary

significantly. The Sm-Co film with a content of Sm of 16.7 at.% corresponding to the stoichiometric composition of $SmCo_5$ shows very strong $SmCo_5$ (0001) and (0002) peaks indicating a good crystallinity and/or good texture. The texture quality was studied by measuring the rocking curves of the $SmCo_5$ (0002) peaks. The variations of the integral intensity and the full width at half maximum of the rocking curve ($\Delta\theta_{50}$) of $SmCo_5$ (0002) peak as a function of Sm content are summarized in Fig. 4.21.

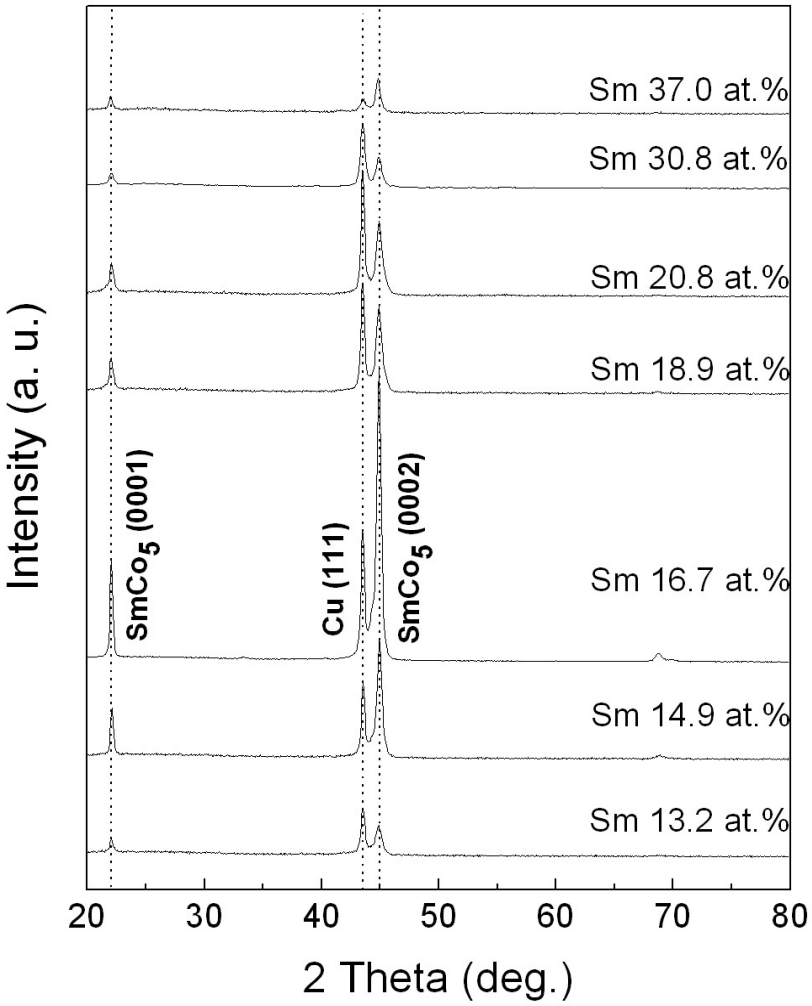

Fig. 4.20. XRD spectra of 65 nm Sm-Co films with different Sm contents grown on Ta (4 nm) / Cu (50 nm) underlayers.

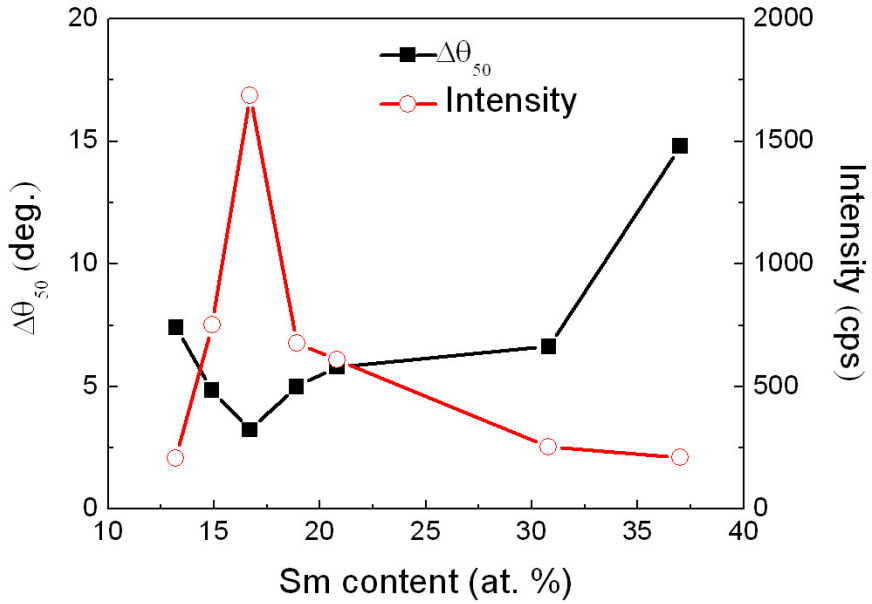

Fig. 4.21. Dependence of full width at half maximum of the rocking curves ($\Delta\theta_{50}$) and integral intensity of (0002) peaks of $SmCo_5$ according to the Sm-Co composition.

The intensity of the $SmCo_5$ (0002) peak increases significantly when the Sm content increases from 13.2 at. % to 16.7 at. %. It reaches a maximum at 16.7 at. % and decreases continuously from 16.7 at. % to 37.0 at. %. The $\Delta\theta_{50}$ reaches a minimum of 3.2° at 16.7 at. % of Sm indicating an excellent (000l) texture of the $SmCo_5$ phase. One may notice that the intensity of the Cu (111) peak is different in the different samples. The intensity of Cu (111) peak was the same for all samples before the deposition of the Sm-Co film at high temperature. During the deposition of Sm-Co film, the structure of the Cu underlayer is deteriorated due to diffusion which is significantly dependent on the composition of the Sm-Co film. Consequently, the deteriorated texture of the Cu underlayer affects the texture of $SmCo_5$. Therefore, the texture of Sm-Co layer is affected by both Sm content and the subsequently deteriorated Cu underlayer.

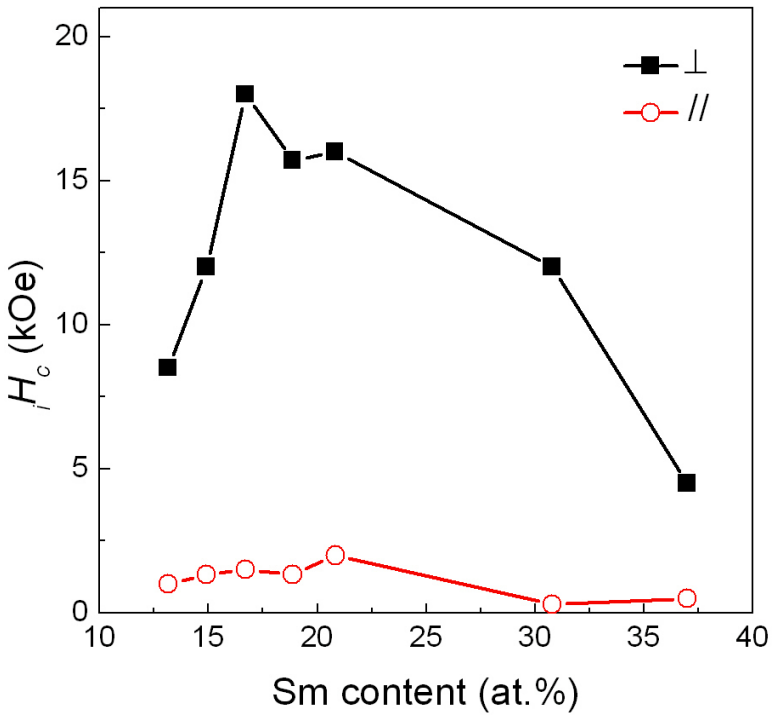

Fig. 4.22. Dependence of in-plane and out-of-plane $_iH_c$ of Sm-Co films on the Sm-Co composition.

The trends of $_iH_c$ in the in-plane and out-of-plane direction of Sm-Co films with different compositions are summarized in Fig. 4.22. All the films exhibit a perpendicular anisotropy where the out-of-plane $_iH_c$ is much larger than the in-plane $_iH_c$. The coercivities of the films are strongly dependent on the Sm-Co composition. The out-of-plane $_iH_c$ trend is consistent with the trend of the intensity and the $\Delta\theta_{50}$ of the $SmCo_5$ (0002) peak shown in Fig. 4.21, where larger out-of-plane $_iH_c$ corresponds to larger intensity and smaller $\Delta\theta_{50}$ of the $SmCo_5$ (0002) peak.

4.4 Fabrication of $SmCo_5$ films with Cu / Ti and Cu / W dual underlayers on glass substrates and study of their structure and magnetic properties

As discussed earlier, the improvement of the crystallinity of the Cu underlayer was due to the smooth metallic seed layer of Ta. Ta has a much higher melting temperature and surface free energy than those of Cu. It is easier to form a smooth seed layer on glass substrate even if the metallic layer is very thin (4 nm). It is interesting to study how melting temperature of metal may affect the crystallinity and texture of Cu underlayer and its effect on the magnetic properties of the subsequently deposited $SmCo_5$ layer. In this project, other two metals (Ti and W) were investigated as the seed layer. The selection of the two metals was based on their melting temperatures (T_m = 1668 ^oC for Ti, which is much lower than that of Ta, while W has a much higher T_m – 3422 ^oC).

$SmCo_5$ films were deposited on Cu (50 nm) / Ti or W (4 nm) underlayers under the optimal conditions found previously where the thickness of $SmCo_5$ layer was fixed at 65 nm and the deposition temperature of $SmCo_5$ was fixed at 400 °C.

4.4.1 Deposition of $SmCo_5$ thin film on Cu / Ti underlayer

Fig. 4.23a shows the XRD spectrum of the $SmCo_5$ thin film grown on Cu / Ti underlayer. The Cu (111), $SmCo_5$ (0001) and $SmCo_5$ (0002) reflection peaks are clearly observed. The $\Delta\theta_{50}$ of these peaks are summarized in Table 4.5. The table also includes the surface roughness (R_q) of the Cu underlayer deposited on a 4 nm Ti seed layer. The R_q of the Cu underlayer significantly decreases from 4.3 nm to 0.8 nm

when grown on a 4 nm Ti seed layer. Results from the $SmCo_5$ films deposited with only a Cu underlayer and a Cu / Ta underlayer are also listed for comparison. For the sample with only a Cu underlayer, the rocking curves of $SmCo_5$ (0001) and $SmCo_5$ (0002) peaks are a horizontal line within the measurement range of 20^o and thus it is believed that the $\Delta\theta_{50}$ is larger than 20^o. The $\Delta\theta_{50}$ of Cu (111), $SmCo_5$ (0001) and $SmCo_5$ (0002) peaks significantly decreases to 4.0^o, 3.4^o and 3.9^o, respectively when a 4nm Ti seed layer is introduced.

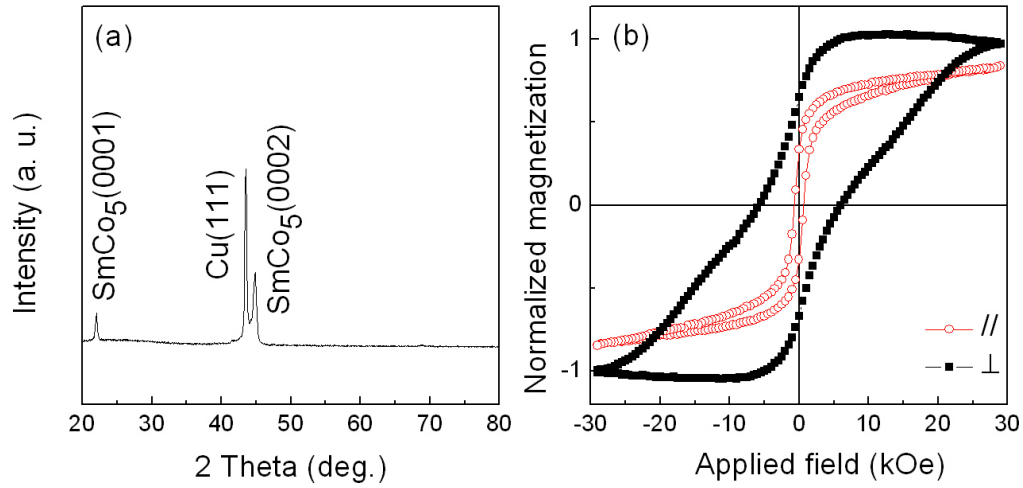

Fig. 4.23. (a)XRD spectrum and (b) M-H loops of the $SmCo_5$ film grown on Cu / Ti dual underlayer.

Fig. 4.23b shows the M-H loops of the $SmCo_5$ thin film grown on Cu / Ti underlayer. The out-of-plane ${}_iH_c$ is around 6 kOe and the in-plane coercivity is only 0.5 kOe. The perpendicular anisotropy and out-of-plane coercivity of the $SmCo_5$ film are enhanced by a thin Ti seed layer. The enhancements are attributed to the improved crystallinity and texture of the $SmCo_5$ phase.

Compared with a Ta seed layer, a Ti seed layer is slightly less effective with respect to the improvement of the surface roughness and the (111) texture of Cu underlayer, and the improvement of the (0001) texture and out-of-plane coercivity of

the $SmCo_5$ film. But the results imply that Ti is still an effective seed layer for improving the crystallinity, the (0001) texture and the out-of-plane coercivity of $SmCo_5$ films.

Table 4.5. $\Delta\theta_{50}$ of the Cu (111), $SmCo_5$ (0001) and $SmCo_5$ (0002) peaks and R_q of Cu underlayers for film samples with different seed layers.

Seed layer	$\Delta\theta_{50}$ of Cu (111) (^{o})	$\Delta\theta_{50}$ of $SmCo_5$ (0001) (^{o})	$\Delta\theta_{50}$ of $SmCo_5$ (0002) (^{o})	R_q of Cu (nm)
No seed layer	undetectable	> 20	> 20	4.3
Ta	3.9	3.4	3.2	0.5
Ti	4.0	3.4	3.9	0.8
W	3.1	2.4	2.5	0.8

4.4.2 Deposition of $SmCo_5$ thin film on Cu / W underlayer

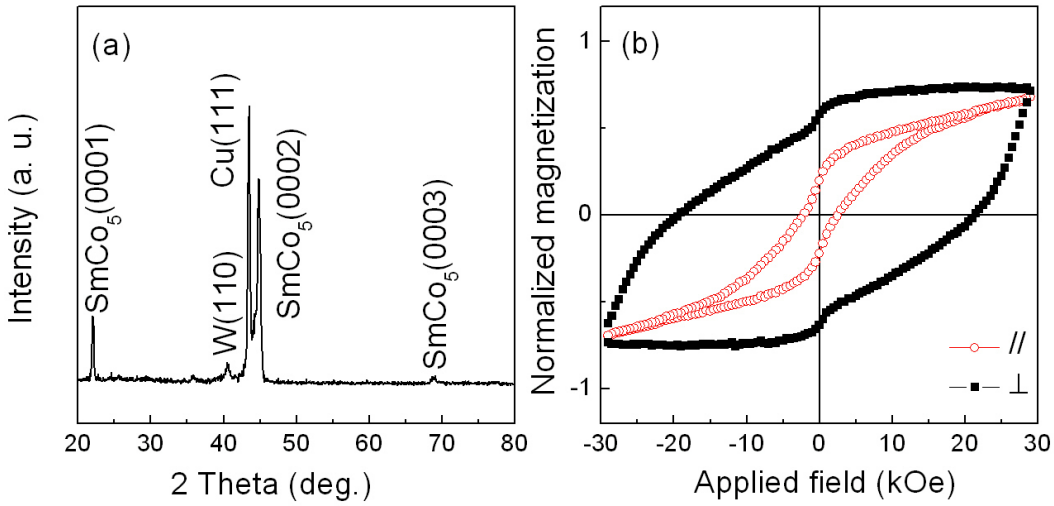

Fig. 4.24. (a)XRD spectrum and (b) M-H loops of the $SmCo_5$ film on Cu / W dual underlayer.

Fig. 4.24 shows the XRD spectrum and the M-H loops of the $SmCo_5$ thin film grown on Cu / W underlayer. The Cu (111), $SmCo_5$ (0001) and $SmCo_5$ (0002)

reflection peaks are clearly observed. A $SmCo_5$ (0003) reflection peak is also observed. A W (110) peak comes from the 20 nm W cover layer. From Table 4.5, it can be seen that with a Cu / W underlayer, the $\Delta\theta_{50}$ of Cu (111), $SmCo_5$ (0001) and $SmCo_5$ (0002) peaks are 3.1°, 2.4° and 2.5°, respectively which are even smaller that the results from the $SmCo_5$ film grown on Cu / Ta underlayer. It suggests that W serves as the most effective seed layer for improving the crystallinity and the (0001) texture of $SmCo_5$ films. The better texture does not bring larger coercivity. The out-of-plane coercivity of the $SmCo_5$ film grown on Cu / W underlayer is around 20.5 kOe which is slightly larger than the one grown on Cu / Ta underlayer (19.5 kOe).

4.4.3 Magnetic reversal mechanism of $SmCo_5$ thin films

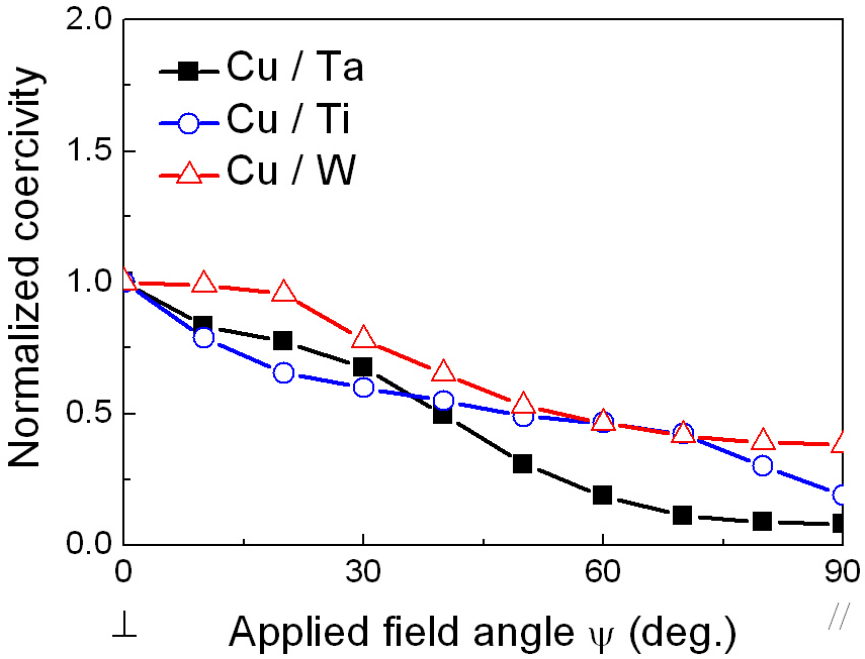

Fig. 4.25. Angular dependence of normalized coercivity of the $SmCo_5$ films grown on Cu / Ta, Cu / Ti and Cu / W underlayers. Zero field refers to out-of-plane direction.

The angular dependences of normalized coercivity were measured to

investigate the magnetization reversal mechanism. Fig. 4.25 shows the angular dependences of the normalized coercivity for $SmCo_5$ films deposited on Cu / Ta, Cu / Ti and Cu / W underlayers. ψ is the angle between applied field and easy direction of magnetization. For all the samples, the coercivities keep decreasing with the increasing angle. These curves resemble to the S-W model. It indicates that the $SmCo_5$ grains rotate coherently.

4.5 Summary

A Ta seed layer can effectively improve the crystallinity, texture and surface morphology of the Cu underlayer. The improvement is strongly dependent on the thickness of the seed layer. The optimal Ta seed layer is a thin, continuous and amorphous-like layer with a thickness of 4 nm. The crystallinity, (0001) texture and magnetic properties of $SmCo_5$ thin films are found to be dependent on the deposition temperature, the texture of the Cu (111) underlayer, the roughness of the Cu underlayer and the formation of $Sm(Co,Cu)_5$ alloy through the diffusion of Cu. Under the optimal conditions, with a Cu (50 nm) / Ta (4 nm) underlayer, after deposition at 400 ^oC the $SmCo_5$ magnetic layer possesses a good (0001) texture, a small $\Delta\theta_{50}$ value (3.2^o) and a large perpendicular coercivity around 19.5 kOe. Furthermore, a thin Ti and a thin W seed layer have been proved to be effective in improving the crystallinity, (0001) texture and magnetic properties of $SmCo_5$ thin films as well.

4.6 References

[1]. D. Weller, A. Moser, L. Folks, M. Best, W. Lee, M. Toney, M. Schwickert, J. Thiele and M. Doerner, IEEE Trans. Magn. **36**, 10 (2000).

[2]. J. Sayama, T. Asahi, K. Mizutani and T. Osaka, J. Phys. D: Appl. Phys. **37**, L1–L4 (2004).

[3]. S. Takei, A. Morisako and M. Matsumoto, J. Magn. Magn. Mater. **272–276**, 1703 (2004).

[4]. J. Sayama, K. Mizutani, T. Asahi and T. Osaka, Appl. Phys. Lett. **85**, 5640 (2004).

[5]. I. Kato, S. Takei, X. Liu and A. Morisako, IEEE Trans. Magn. **42**, 2366 (2006).

[6]. Y. K. Takahashi, T. Ohkubo and K. Hono, J. Appl. Phys. **100**, 053913 (2006).

[7]. J. Sayama, K. Mizutani, T. Asahi, J. Ariake, K. Ouchi and T. Osaka, J. Magn. Magn. Mater. **301**, 271 (2006).

[8]. A. Morisako and X. Liu, J. Magn. Magn. Mater. **304**, 46 (2006).

[9]. J. S. Chen, L. N. Zhang, J. F. Hu and J. Ding, J. Appl. Phys. **104**, 093905 (2009).

[10]. L. N. Zhang, J. F. Hu, J. S. Chen and J. Ding, J. Appl. Phys. **105**, 07A743 (2009).

[11]. M. Ohtake, Y. Nukaga, F. Kirino and M. Futamoto, J. Appl. Phys. **105**, 07C315 (2009).

[12]. M. Tsunoda, T. Ito, M. Takahashi and T. Shiba, J. Magn. Soc. Jpn. **22**, 457 (1998).

[13]. M. Takahashi, H. Shoji, D. D. Djayaprawira and S. Yoshimura, IEEE Trans. Magn. **36**, 2315 (2000).

[14]. S. Yoshimura, D. D. Djayaprawira, T. K. Kong, Y. Masuda, H. Shoji and M. Takahashi, J. Appl. Phys. **87**, 6860 (2000).

[15]. S. Yoshimura, D. D. Djayaprawira, M. Mikami, Y. Takakuwa and M. Takahashi, IEEE Trans. Magn. **38,** 1958 (2002).

[16]. L. Z. Mezey and J. Giber, Jpn. J. Appl. Phys. **21**, 1569 (1982).

[17]. A. G. Roy and D. E. Laughlin, J. Appl. Phys. **91**, 8076 (2002).

[18]. K. Holloway and P. M. Fryer, Appl. Phys. Lett. **57**, 1736 (1990).

[19]. S. Q. Wang, Mater. Res. Soc. Bull. **19**, 30 (1994).

[20]. R. Hoogeveen, M. Moske, H. Geisler and K. Samwer, Thin Solid Films **275**, 203 (1996).

[21]. K. Hieber and N. M. Mayer, Thin Solid Films **90**, 43 (1982).

5 Chapter V $SmCo_5$ thin films with perpendicular anisotropy grown on Ni-alloy underlayers

As we saw in Chapter 4, Cu-(111) is an effective underlayer to induce (000l) textured $SmCo_5$ thin films showing perpendicular anisotropy. Different seed layers including titanium (Ti) [1], ruthenium (Ru) [2], tantalum (Ta) [3, 4] and tungsten (W) have been found useful in improving the quality and crystallinity of the (111)-textured Cu underlayer.

However, a Cu underlayer poses two main issues: heavy diffusion of Cu into the $SmCo_5$ layer and formation of large grains of $SmCo_5$. First, Cu diffusion is problematic because it forms the $Sm(Co, Cu)_5$ alloy which decreases the intrinsic magnetocrystalline anisotropy of the thin film and also because it is more difficult to optimize the microstructure and the magnetic properties of the thin film in the presence of an uncontrollable diffusion phenomenon (although it has been proven that Cu can lower the crystallization temperature of $SmCo_5$). Second, relatively large grains of $SmCo_5$ tend to form on the Cu underlayer even if the crystallinity of the Cu underlayer is poor. Large grains are not desirable for magnetic recording.

As shown in Chapter 4, Cu diffusion may produce inhomogeneities which are evidenced by the apparition of a step around the magnetic remanence in the hysteresis loop (due to non-uniform demagnetization) and the $Sm(Co, Cu)_5$ grains can be as large as 60 nm.

Therefore, it is necessary to look for an alternative underlayer with a much lower diffusion rate and which can induce the (0001) texture of $SmCo_5$ with a nanocrystalline microstructure. Recently, Seifert et al. [5] reported that epitaxial $SmCo_5$ with perpendicular anisotropy could be prepared on a Ru buffered Al_2O_3 (0001) single crystal substrate without any Cu addition. However, the lattice misfit between Ru (0002) and $SmCo_5$ (0001) is rather large (8 %) which generates misfit dislocations and results in a rough surface morphology. Moreover, the expensive

sapphire substrate and exceedingly rare Ru are not favorable for practical applications. Therefore, an economic layer system with good properties, based on a glass substrate and producible at relatively low deposition temperature needs to be investigated.

Selection of alternative metallic underlayer

Table 5.1. Metals with a melting temperature (T_m) higher than 1200 ^oC and with a fcc or a hcp structure and the lattice misfits between these metals and $SmCo_5$. "+" represents a bigger lattice constant of listed metal compared with that of $SmCo_5$, whereas "-" represents a smaller lattice constant of listed metal compared with that of $SmCo_5$.

Structure	Metals	T_m (^oC)	Lattice constant (Å)	Lattice misfit (%)
fcc	Cu	1084	a=3.61	+2.1
fcc	**Ni**	**1455**	**a=3.54**	**-0.4**
fcc	Mo	2623	a=3.14	-12.6
fcc	Rh	1964	a=3.80	+7.0
fcc	Pd	1555	a=3.88	+8.9
fcc	Ir	2466	a=3.83	+7.7
fcc	Pt	1768	a=3.92	+9.8
hcp	Ti	1668	a=2.95	+15.3
hcp	Co	1495	a=2.50	-0.4
hcp	Ru	2334	a=2.71	+7.7
hcp	Re	3186	a=2.76	+9.4
hcp	Os	3033	a=2.73	+8.4

Metals with a higher melting temperature (T_m) can be expected to have a smaller diffusion rate than that of Cu. The suitable candidates should possess an fcc structure or an hcp structure because the (111) plane of the fcc structure or the (0001) plane of the hcp structure can possibly match the (0001) plane of the hcp structured $SmCo_5$ as perpendicular magnetic media. The possible candidates are listed in Table 5.1 with a higher T_m than that of Cu and with a fcc or a hcp structure. The calculated

lattice misfits between the candidate metals and $SmCo_5$ are also listed. It can be seen that fcc-Ni and hcp-Co have small lattice misfits with $SmCo_5$. However, Co films deposited at room temperature may not be of the single hcp-phase, as the fcc-phase may be mixed. Therefore, it is difficult to form a (0001) textured hcp Co thin film at room temperature. Thus, Ni is the only ideal candidate.

Structure of Ni and Ni-W alloy

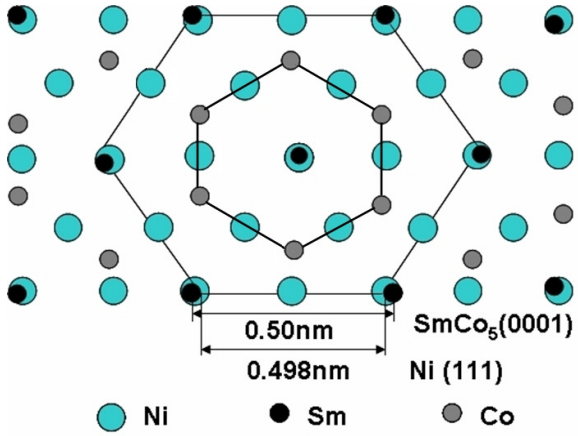

Fig. 5.1. Illustration of lattice matching between Ni (111) and $SmCo_5$ (0001).

As discussed above, Nickel (Ni) is a possible candidate underlayer for inducing (0001) textured $SmCo_5$ because of the excellent lattice-matching between Ni close-packed (111) planes and $SmCo_5$ (0001) planes with a lattice misfit of only 0.4% (as shown in Fig. 5.1). However, Ni is a soft ferromagnet with a Curie temperature of 354 °C. If a $SmCo_5$ layer is deposited on a soft magnetic underlayer, it may significantly reduce the overall coercivity and magnetic remanence. Therefore, the Curie temperature of Ni has to be reduced below room temperature. In this project, the method of alloying with another non-magnetic element was used to reduce the Curie temperature. The alloying metal should have a high melting temperature to avoid diffusion into the $SmCo_5$ layer and to avoid a significant

decrease in the melting temperature of the Ni-alloy. Thus, the refractory metals, such as W, Re, Ta and Mo, are possible candidates. However, the dopant should be able to form a solid solution phase with Ni at room temperature in a relatively large compositional range in order to keep the fcc structure of the Ni-alloy and reduce the Curie temperature to below room temperature. After the investigation of the binary phase diagrams between the refractory metals and Ni, W has been indentified to be the suitable candidate.

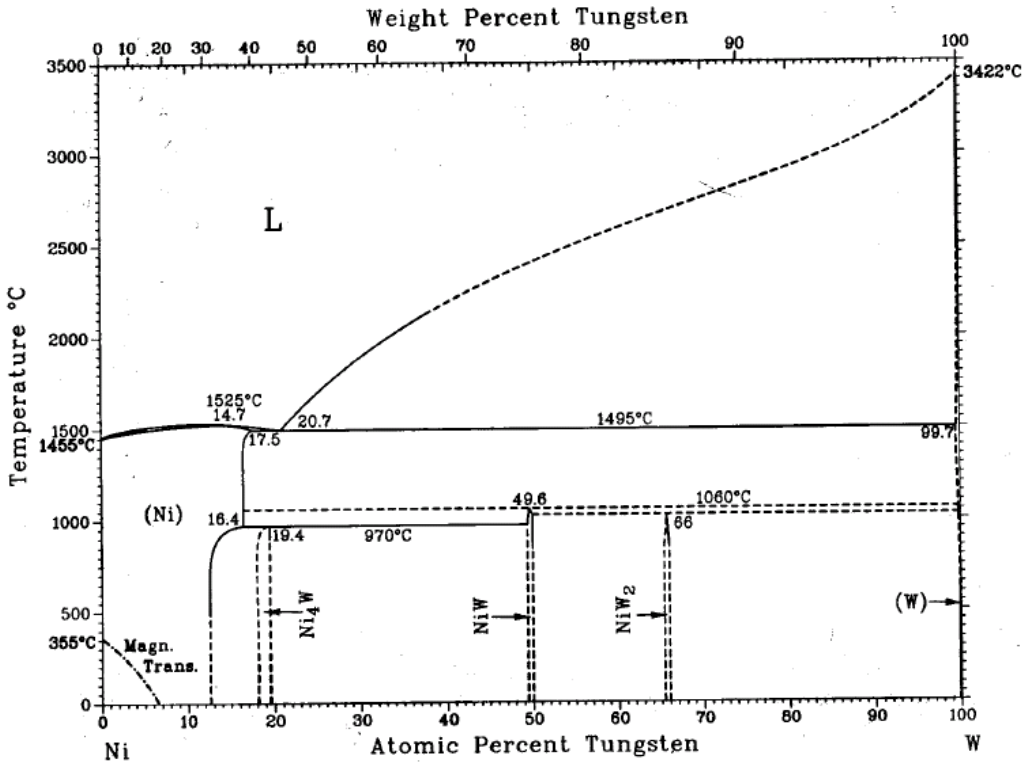

Fig. 5.2. Phase diagram of Ni-W binary alloys [6].

The Ni-W phase diagram is shown in Fig. 5.2 [6]. Doping with W can reduce the Curie temperature of Ni below room temperature by the formation of a fcc Ni-W solid solution with a W concentration of approximately 8 at.% or higher (see ref. [7]). The solubility of W in Ni is around 12 at.% at room temperature. Moreover, in

the Ni-W phase diagram, the presence of the intermediate phase Ni_4W is noticed. It is also able to induce hcp-$SmCo_5$ as discussed in the next paragraph.

The crystal structure of the Ni_4W phase is shown in Fig. 5.3a. Ni_4W is an ordered superstructure of an fcc lattice of the Ni_4Mo type [8-10]. This tetragonal structure belongs to the *I4/m* space group. The dimensions of unit cell are a=5.73Å and c=3.553Å based on PDF file No. 65-2673 (as shown in Fig. 5.3a). The close-packed ordered plane (211) is outlined and labeled in Fig. 5.3a. As reported in Ref. 11, the Ni-Ni and Ni-Mo distances are equal in the Ni_4Mo structure type. Therefore, the nearest atomic distances of Ni-Ni and Ni-W in the (211) plane of the Ni_4W structure is 2.56 Å calculated from the dimensions of the unit cell. An experimental confirmation has been provided by Nasu et al. [11] who claimed that the nearest Ni–Ni distance was 2.49 Å and the Ni–W distance was 2.50 Å by using EXAFS and SAXS methods.

The Ni and W atoms in the (211) plane have a hexagonal structure which is very similar to the structure of the $SmCo_5$ (0001) plane (as shown in Fig. 5.3b). Sm and Co atoms can match either Ni or W atoms. The lattice misfit between Ni_4W (211) and $SmCo_5$ (0001) is around 2.3%. Therefore, it should be possible to induce a (0001)-textured $SmCo_5$ film on a (211)-textured Ni_4W underlayer.

In this chapter, a systematic study was carried out on the structure and the magnetic properties of $SmCo_5$ films on Ni-W underlayers with different W concentration.

.

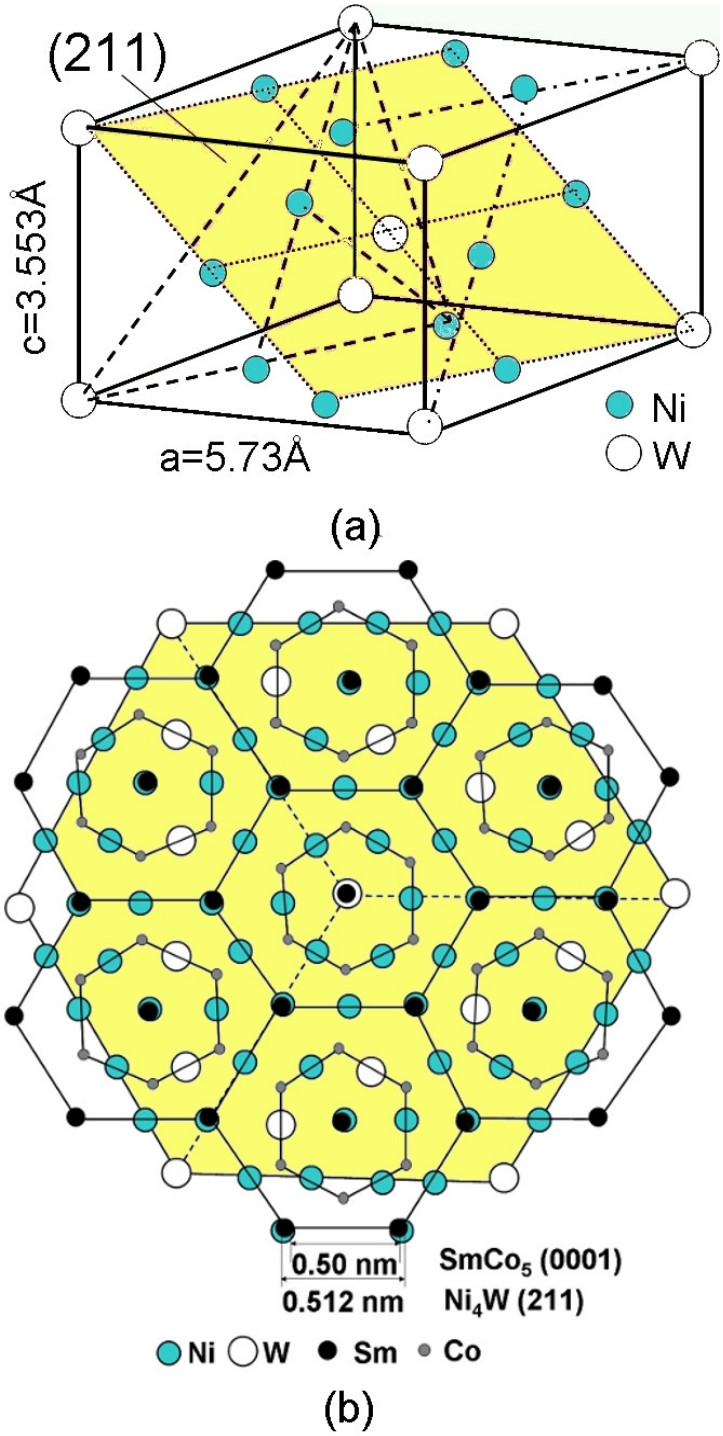

Fig. 5.3. (a) Tetragonal unit cell of Ni_4W. (b) The relationship between the Ni_4W (211) plane and the $SmCo_5$ (0001) plane.

5.1 Experimental methods

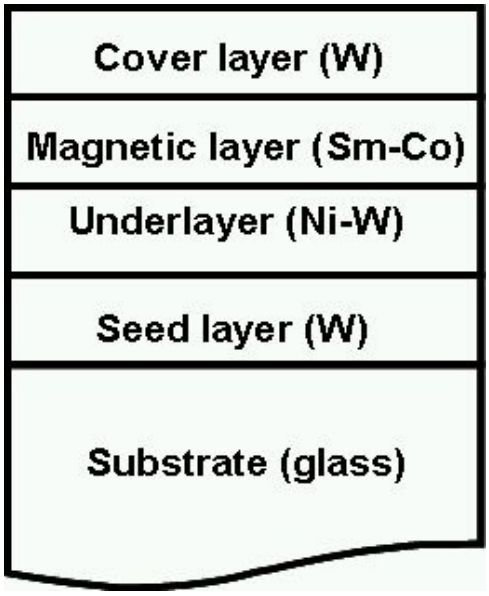

Fig. 5.4. Schematic diagram of the multilayer structure.

The multilayer film structure developed in this chapter is shown in Fig. 5.4. Experiments were conducted in three parts:

(1) Study of the Ni-W underlayer. A 4 nm W seed layer was first deposited on glass substrate at room temperature. The $Ni_{100-x}W_x$ (x=0~100) underlayer of 40 nm was then deposited at room temperature through co-sputtering of two elemental Ni and W targets. The alloy composition was adjusted through the sputtering power.

(2) Study of $SmCo_5$ thin films grown on $Ni_{100-x}W_x$ (x=0~100) / W underlayer. Two targets of Sm and Co were used for the co-sputtering of Sm-Co thin films. 65 nm thick $SmCo_5$ films were deposited at 530 ^oC on $Ni_{100-x}W_x$ (x = 0 ~ 100) (40 nm) / W (4 nm) underlayers.

(3) Study of Sm-Co thin films grown on a Ni_4W / W underlayer. 65 nm of $SmCo_5$ was deposited at different substrate temperatures ranging from room

temperature to 550 °C. $SmCo_5$ (20-100 nm) / Ni_4W (40 nm) / W (4 nm) and $SmCo_5$ (65 nm) / Ni_4W (0-80 nm) / W (4 nm) films were prepared to study the effect of the thickness of the Sm-Co layer and the Ni_4W underlayer at the temperature of 500 °C (found to be optimal). In the composition study, the composition of the Sm-Co layer ranges from $Sm_{13}Co_{87}$ to $Sm_{33}Co_{67}$.

A 20 nm W cover layer was deposited in each sample to avoid the oxidation of the Sm-Co layer.

5.2 Study of Ni-W alloy underlayers

5.2.1 Crystallographic structure

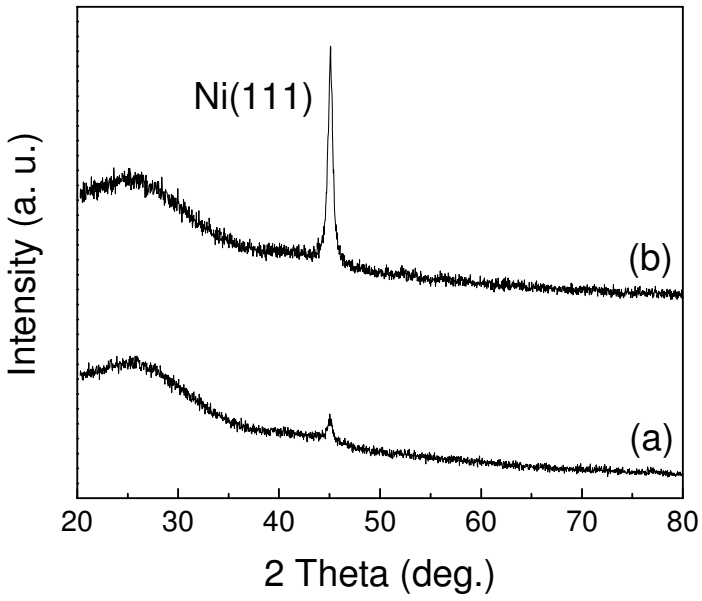

Fig. 5.5. XRD spectra of 40 nm Ni films (a) with a 4 nm W seed layer and (b) without seed layer.

As discussed in Chapter 4, a metal seed layer with a high melting point can improve the crystallinity and surface roughness of the Cu (111) underlayer. From

Fig. 5.5, with a 4 nm W film as the seed layer, the 40 nm Ni film shows an improved crystallinity and texture. On the other hand, without the W seed layer, the Ni layer shows a poor crystallinity as the (111) peak has much lower intensity. Therefore, in this work, the Ni-W underlayers were deposited on W seed layers with a thickness of 4 nm.

XRD spectra of the Ni-W films are shown in Fig. 5.6a. Only the (111) diffraction peak appears in the XRD spectrum of the pure Ni film. However, the texture is poor, as no signal could be obtained in the rocking curve. The intensity of the (111) peak decreases when increasing the W concentration until 8 at.% of W, indicating poor crystallinity in the Ni-W solid solution films. The fcc-(111) peak shifts slightly to a smaller angle when increasing the W concentration. This is due to the lattice expansion because the atomic radius of W (0.137 nm) is larger than that of Ni (0.125 nm). The intensity of the peak at 40~50 degree increases in $Ni_{84}W_{16}$ and reaches its maximum value in $Ni_{80}W_{20}$. The peak intensity decreases again at 22 at. % and disappears at higher W concentrations, indicating the formation of an amorphous-like structure. The peak intensity and its d-spacing are plotted in Fig. 5.6b. My XRD study shows the formation of the specific intermediate phase Ni_4W in the W concentration range of 16-22 at. %. In order to confirm the formation of the Ni_4W phase, a XRD scan from 20° to 120° was conducted for the $Ni_{80}W_{20}$ film. As shown in Fig. 5.7, the Ni_4W (422) peak at 96.0^o is clearly observable which proves the formation of a Ni_4W phase with a (211) texture. A broad rocking curve was observed for $Ni_{80}W_{20}$, as shown in the inset in Fig. 5.6a, indicating a better texture compared with pure Ni.

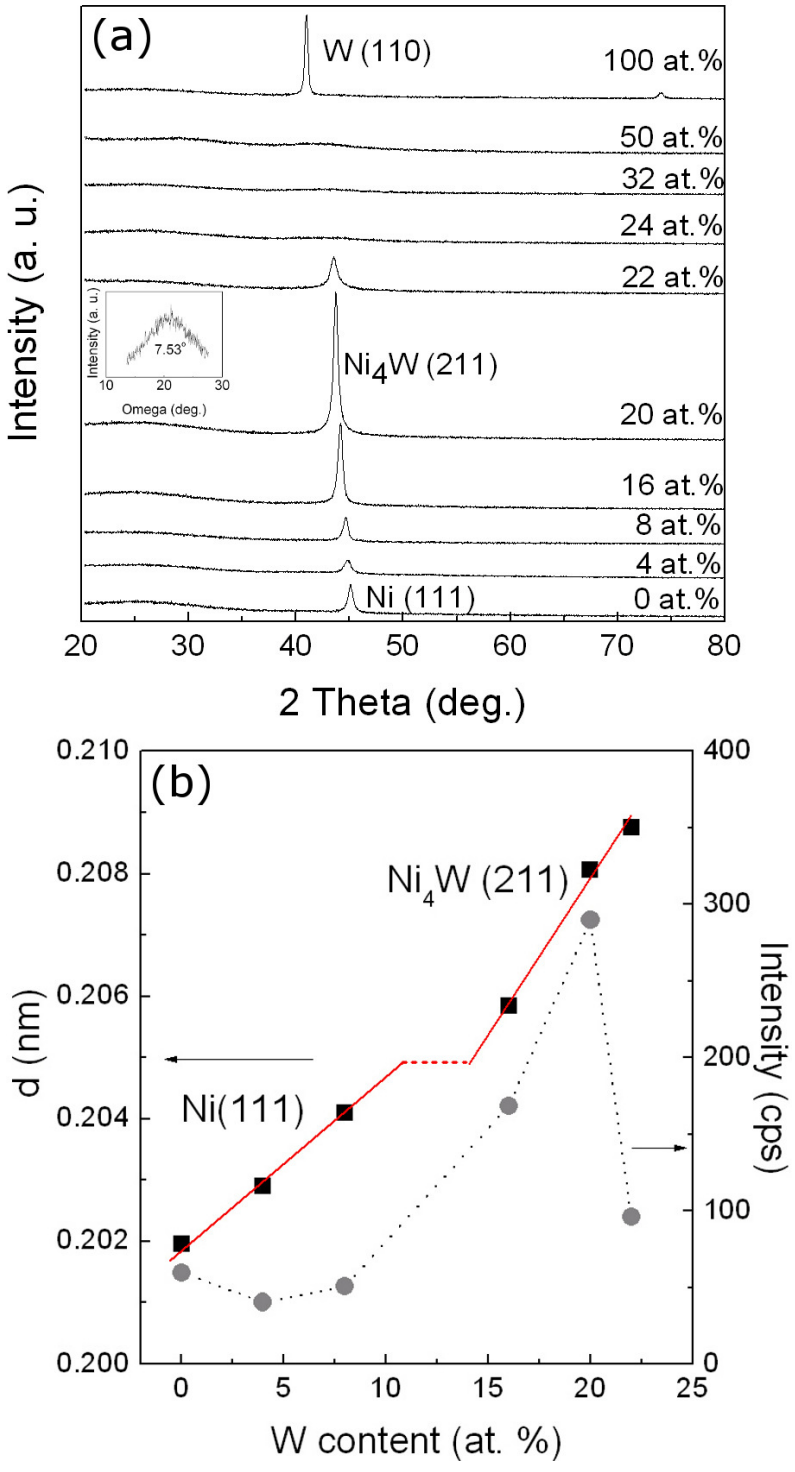

Fig. 5.6. (a) XRD spectra of 40 nm Ni-W layers with a varying W atomic percentage (0 at.% ~ 100 at.%) grown on 4 nm W coated glass substrates. (b) The inter-planar spacing and peak integral intensity of Ni (111) and Ni_4W (211) as a function of W content.

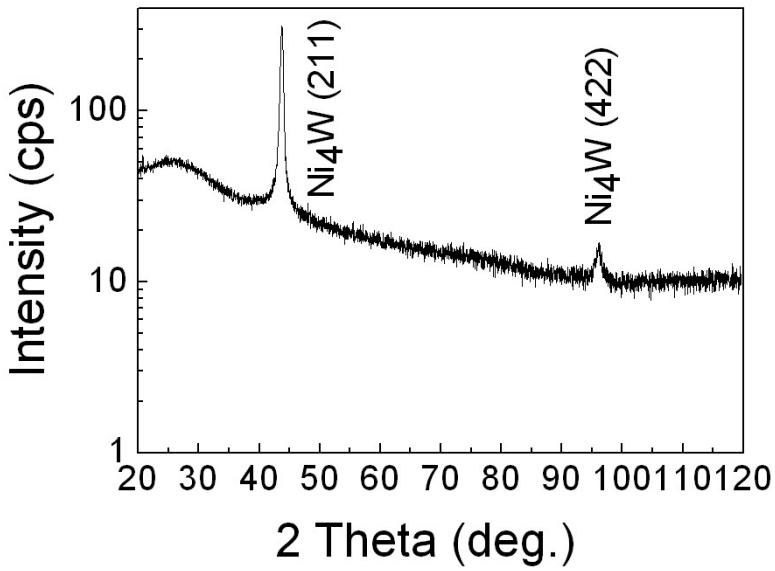

Fig. 5.7. XRD spectrum of the obtained $Ni_{80}W_{20}$ sample within a range from 20° to 120°.

5.2.2 Microstructure

Fig. 5.8a shows the bright field and dark field plane-view TEM images of the Ni and the Ni_4W ($Ni_{80}W_{20}$) thin films and HRTEM images of the $Ni_{68}W_{32}$ and the $Ni_{50}W_{50}$ thin films deposited at room temperature. The microstructure of the pure Ni film is not uniform with a relatively broad grain size distribution of 10-40 nm. The selected area electron diffraction pattern (SAED) inserted in the figure confirms the fcc-Ni phase. The Ni_4W ($Ni_{80}W_{20}$) film has a much smaller grain size of approximately 10 nm. Moreover, the SAED shows a very bright (211) diffraction ring and visible (130), (420) and (422) rings which indicates that the (211) is the preferred orientation in the Ni_4W film. The high-resolution TEM image of the $Ni_{68}W_{32}$ film shows some dark patches. The SAED pattern shows a weak ring of (211)-Ni_4W, indicating the presence of small Ni_4W clusters. The $Ni_{50}W_{50}$ film shows a uniform amorphous structure. The surface morphologies of Ni, Ni_4W and $Ni_{68}W_{32}$

films were studied by AFM, as shown in Fig. 5.8b. It can be seen that the Ni_4W film shows a relatively smooth surface (with a surface roughness R_q =1.07 nm) and the $Ni_{68}W_{32}$ film shows a very smooth surface (R_q = 0.58 nm). On the other hand, the Ni film shows a much rougher surface (R_q =2.07 nm).

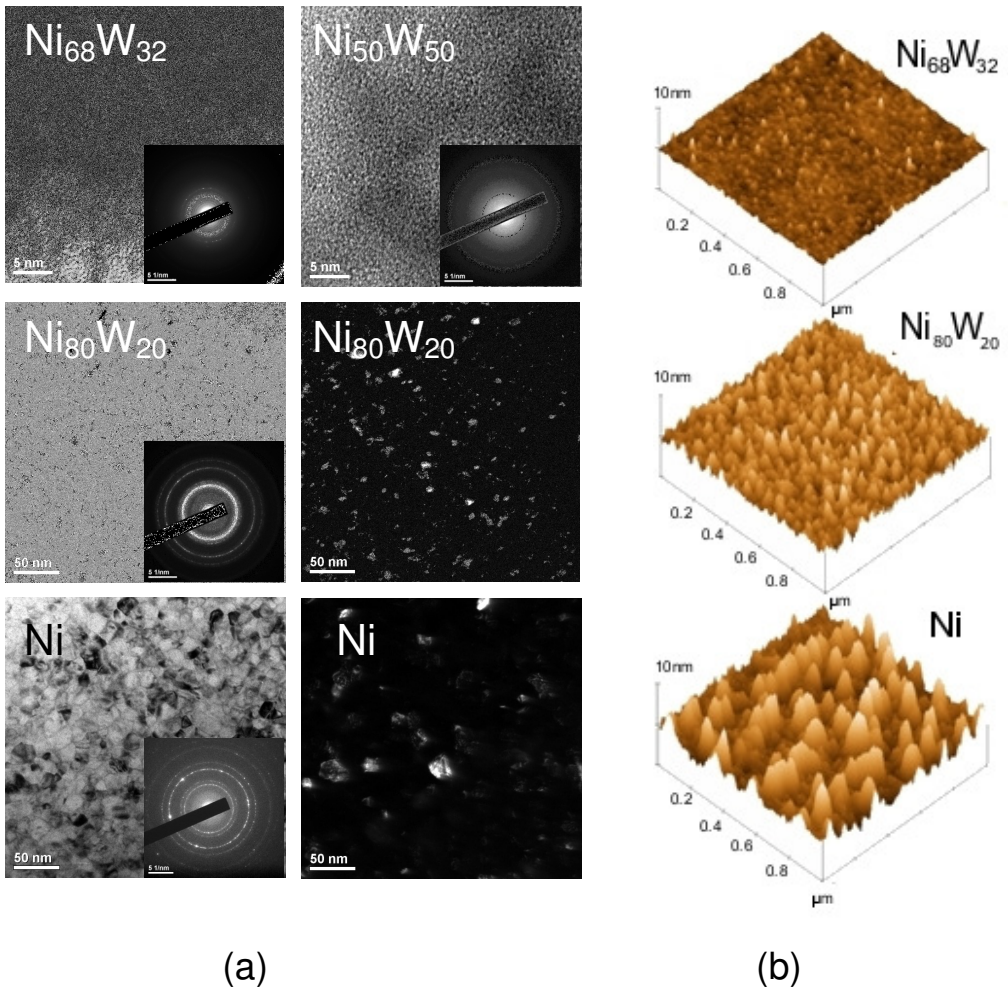

Fig. 5.8. (a) TEM images and diffraction patterns of 40 nm Ni, $Ni_{80}W_{20}$ (Ni_4W), $Ni_{68}W_{32}$ and $Ni_{50}W_{50}$ films grown on 4 nm W coated glass substrates. (b) AFM images of 40 nm Ni, $Ni_{80}W_{20}$, and $Ni_{68}W_{32}$ films grown on 4 nm W coated glass substrates.

5.2.3 Magnetic properties

Fig. 5.9 shows the M-H loops of the Ni–W films at room temperature. The room temperature saturation magnetization (M_s) of Ni-W films decreases with increasing W concentrations and disappears when the W concentration is 8 at.% or higher. The Ni_4W phase shows a paramagnetic behavior at room temperature. Fig. 5.10 shows that the M_s of Ni-W films is inversely proportional to the W content.

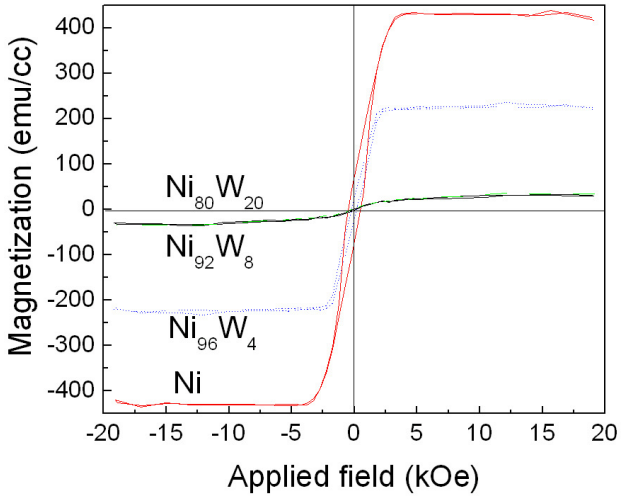

Fig. 5.9. M-H loops of Ni-W alloys with from 0 at.% to 20 at.% of W measured in the direction of perpendicular to the film plane at room temperature by VSM.

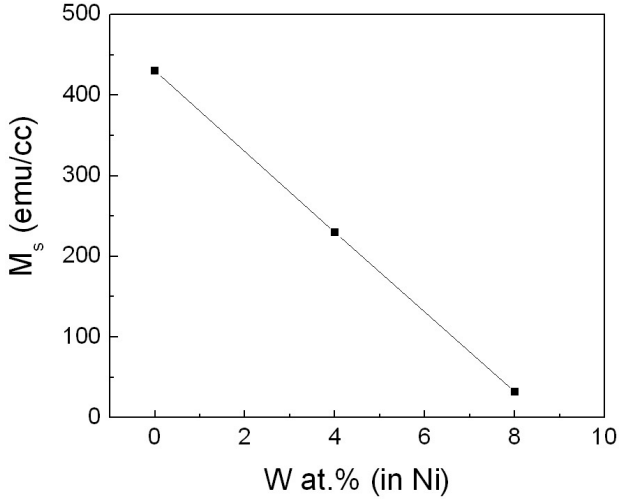

Fig. 5.10. Relation between the W content and the saturation magnetization of Ni-W thin films.

5.3 Fabrication of $SmCo_5$ films on Ni-W alloy underlayers and study of their structure and magnetic properties

5.3.1 Deposition of $SmCo_5$ films on $Ni_{100-x}W_x$ underlayers

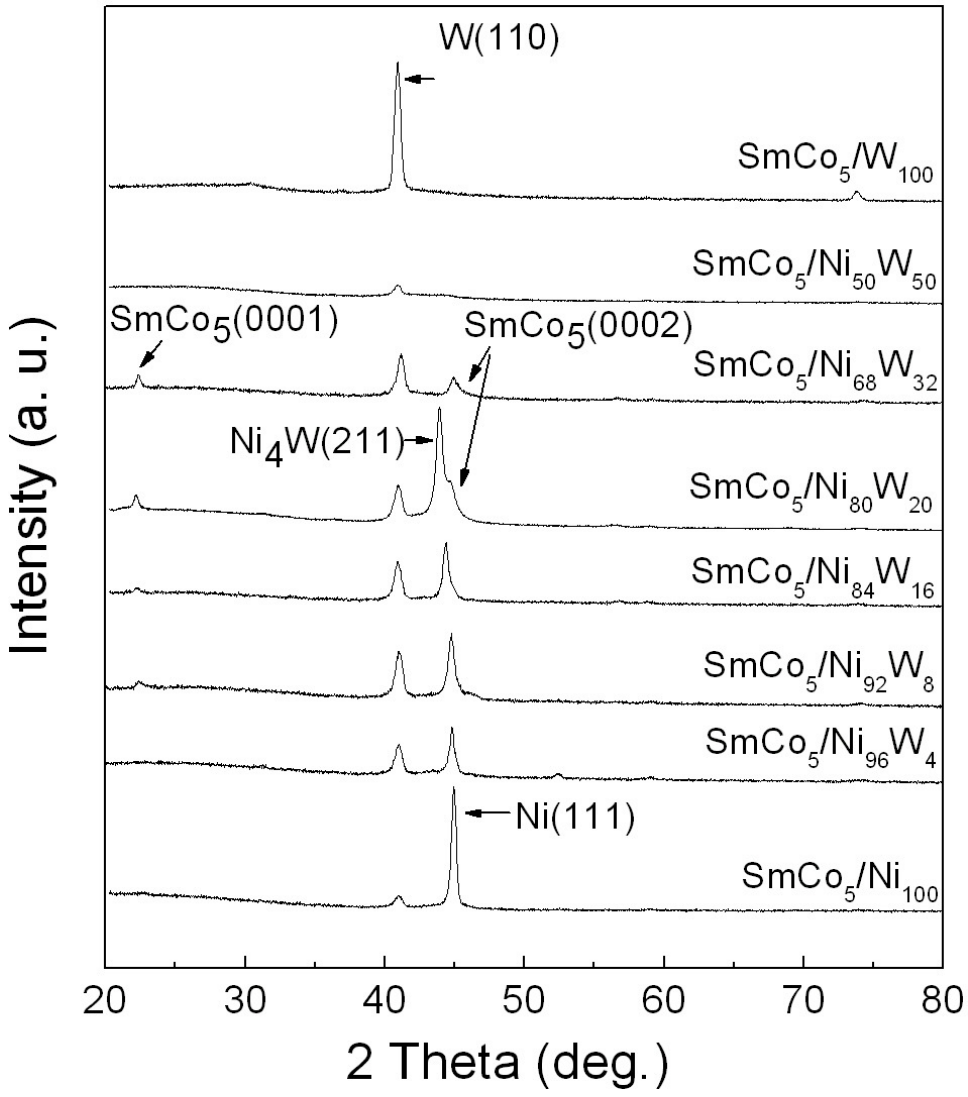

Fig. 5.11. XRD spectra of 65 nm $SmCo_5$ films grown at 530 °C on 40 nm $Ni_{100-x}W_x$ (x = 0 ~100) underlayers.

65 nm-thick $SmCo_5$ films were deposited on $Ni_{100-x}W_x$ (x = 0~100) underlayers with different compositions at the deposition temperature of 530 °C. The detailed studies of the optimization of deposition temperature and thickness will be

discussed in the Section 5.3.2. Fig. 5.11 shows the XRD spectra of $SmCo_5$ thin films. It can be seen that no crystalline peaks for $SmCo_5$ can be found at lower W contents (0 and 4 at. %), indicating an amorphous-like structure. The crystalline peaks of $SmCo_5$ (0001) and (0002) start to appear on the $Ni_{92}W_8$ underlayer, and $SmCo_5$ (0001) and (0002) peaks are clearly visible on the $Ni_{80}W_{20}$ underlayer. It is to note that the W-(110) peak appears in every XRD spectrum because of the W cover layer. Except (0001) and (0002), no other crystalline peaks corresponding to the $SmCo_5$ phase could be observed, indicating a good crystallographic (0001) texture. Surprisingly, the $SmCo_5$ film grown on the $Ni_{68}W_{32}$ underlayer also shows a good crystallinity and a strong (0001) texture. The $Ni_{68}W_{32}$ underlayer exhibits an amorphous-like structure under XRD and shows Ni_4W nanoclusters under TEM with an excellent surface smoothness as shown in Fig. 5.8. The above results suggest that a smooth surface may be favourable to the growth of $SmCo_5$ films with a good crystallinity and texture. On the contrary, the amorphous-like $Ni_{50}W_{50}$ underlayer without nano-clusters results in amorphous-like Sm-Co film as no crystalline peak of $SmCo_5$ can be observed in the XRD spectrum. It implies that the (211) oriented Ni_4W nano-clusters in the $Ni_{68}W_{32}$ underlayer are still needed to induce the growth of a (0001) textured $SmCo_5$ thin film.

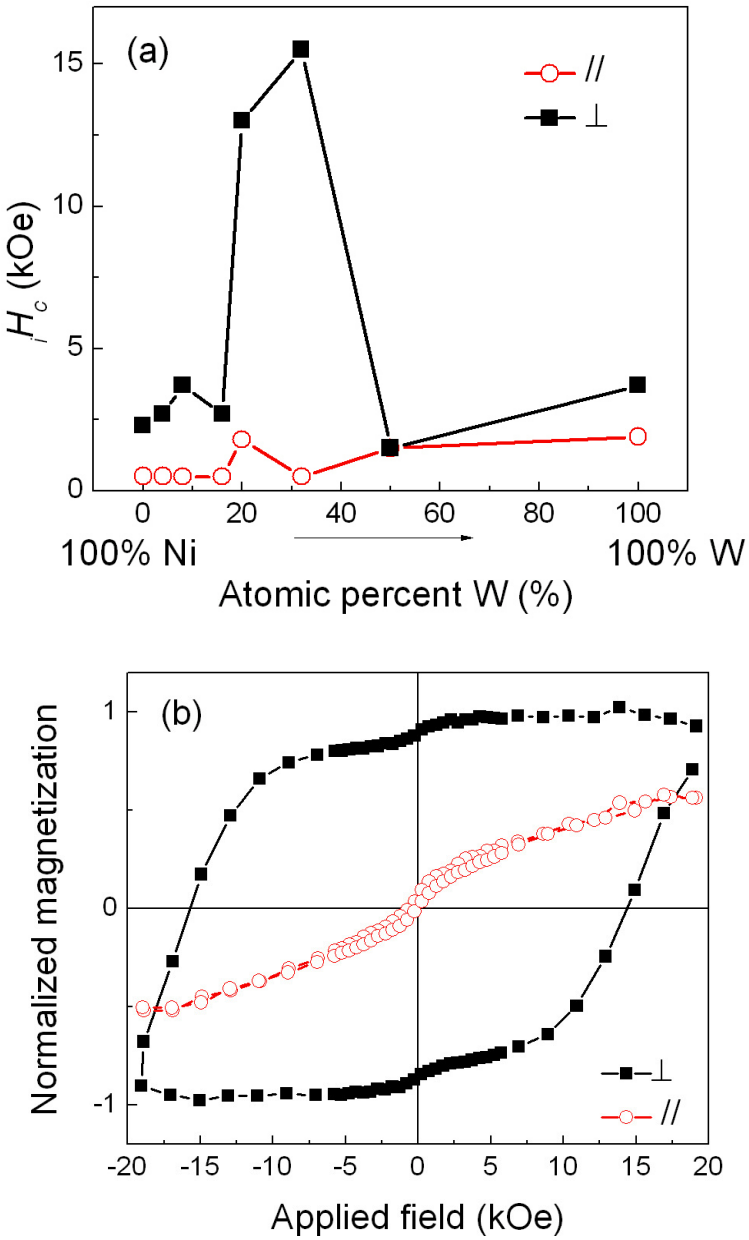

Fig. 5.12. (a) Summary of in-plane and out-of-plane coercivities of 65 nm $SmCo_5$ films grown at 530 °C on 40 nm $Ni_{100-x}W_x$ (x = 0 ~100) underlayers. (b) M-H loops of 65 nm $SmCo_5$ films grown on 40 nm $Ni_{68}W_{32}$ layers on 4 nm W coated glass substrates.

Fig. 5.12a summarizes the in-plane and out-of-plane intrinsic coercivities ($_iH_c$) of $SmCo_5$ films on different $Ni_{100-x}W_x$ (x = 0~100) underlayers. Results indicate that almost all the $SmCo_5$ films exhibit perpendicular anisotropy. Large out-of-plane coercivities and strong perpendicular anisotropy are obtained in the $SmCo_5$ thin films

grown on (211) textured Ni_4W ($Ni_{80}W_{20}$) underlayer and amorphous-like $Ni_{68}W_{32}$ underlayer with Ni_4W clusters, when the (0001)-textured crystalline $SmCo_5$ phase is found in the XRD examination (Fig.). The M-H loops of the $SmCo_5$ film deposited on the $Ni_{68}W_{32}$ underlayer are shown in Fig. 5.12b. The out-of-plane loop has a square shape with an ${}_iH_c$ of 15.5 kOe whereas the in-plane loop shows a very low coercivity. Compared with the previous results for $SmCo_5$ on Cu underlayers [3, 4], $SmCo_5$ thin film grown on a $Ni_{68}W_{32}$ underlayer shows a better squareness and higher perpendicular anisotropy with a nanocrystalline structure as shown in the TEM examination. This work has showed that a (211)-textured Ni_4W underlayer can induce (0001)-textured $SmCo_5$ with a high coercivity and large perpendicular anisotropy. Nanocrystalline Ni_4W with a smooth surface may be more effective in generating (0001)-texture $SmCo_5$ with excellent magnetic properties as observed with the $Ni_{68}W_{32}$ underlayer.

5.3.2 Deposition of $SmCo_5$ films on Ni_4W underlayers

5.3.2.1 Effect of deposition temperature of $SmCo_5$

$SmCo_5$ films with a fixed thickness of 65 nm were used to study the effects of the deposition temperature on the structure and the magnetic properties. Fig. 5.13 shows the XRD spectra of these $SmCo_5$ thin films deposited at elevated temperatures on a 40nm Ni_4W underlayer. It can be seen that no crystalline peaks for $SmCo_5$ can be seen if the deposition temperature is below 500 °C, indicating an amorphous-like structure. The crystalline peaks of $SmCo_5$ (0001) and (0002) start to appear at 500°C. It is to note that except (0001) and (0002), no other crystalline peaks corresponding to the $SmCo_5$ phase could be observed, indicating a good crystallographic (0001) texture. However, when the deposition temperature is further increased to 550°C, the

(0001) peak of $SmCo_5$ disappears and the (0002) peak becomes weaker, indicating a poor crystallinity at higher deposition temperatures.

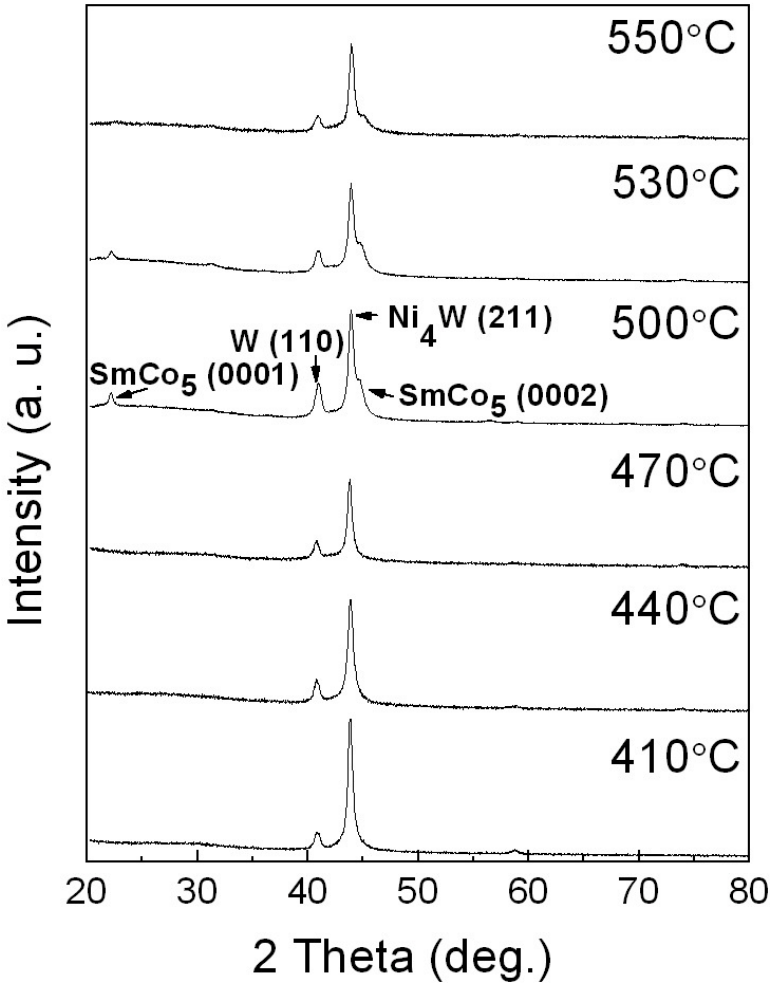

Fig. 5.13. XRD spectra of W 4 nm / Ni_4W 50 nm / SmCo 65 nm (410~550 °C) / W 20 nm (410~550 °C) thin films.

Fig. 5.14a shows the relation between the deposition temperature and the in-plane and out-of-plane ${}_iH_c$ of $SmCo_5$ films. Results indicate that the ${}_iH_c$ of $SmCo_5$ films strongly depends on the deposition temperature. For a deposition temperature ranging between room temperature and 410 °C, the coercivity is practically zero. The

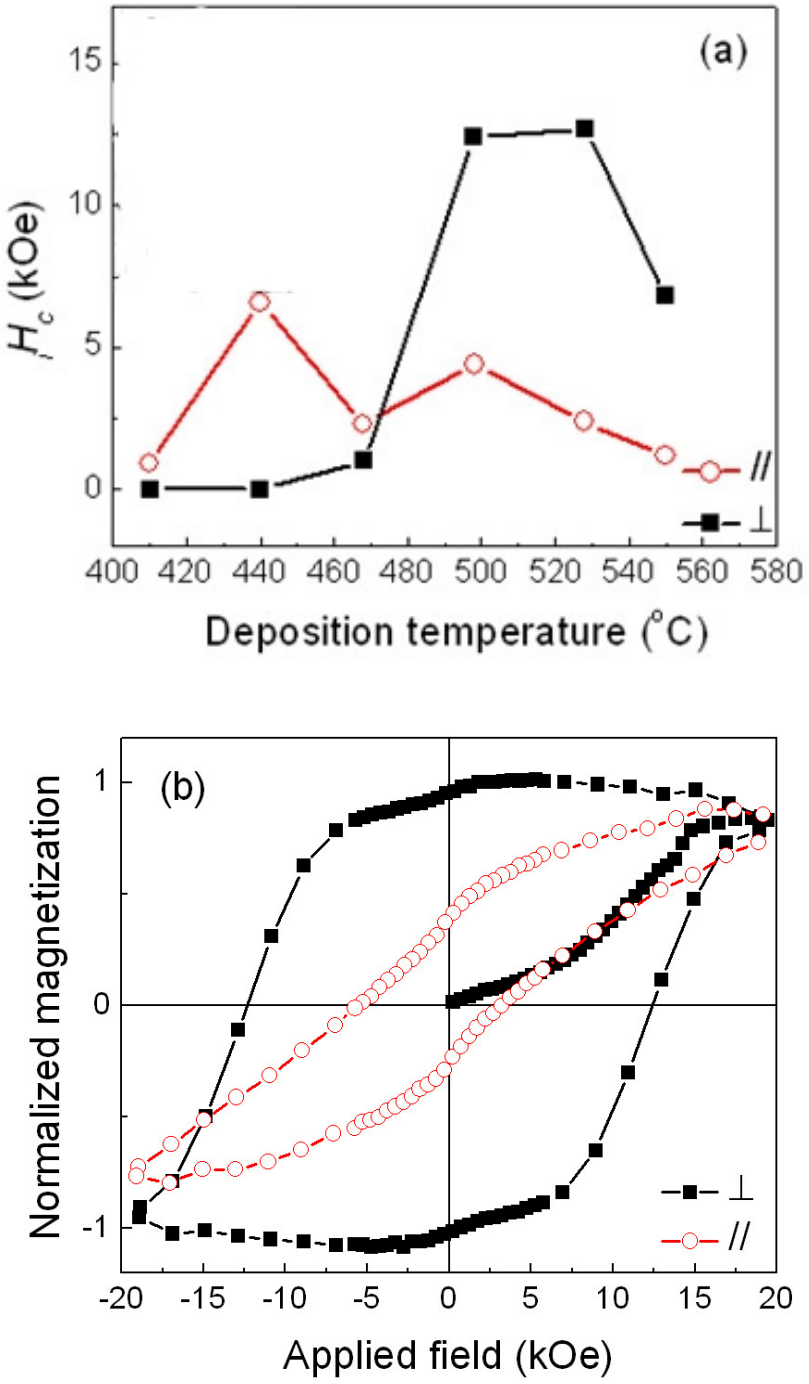

Fig. 5.14. (a) Relation between the deposition temperature and the in-plane and out-of-plane intrinsic coercivities of SmCo in W 4 nm / Ni_4W 40 nm / SmCo 65 nm (410~550 °C) / W 20 nm (410~550 °C) thin films. (b) M-H loops of $SmCo_5$ deposited at 500 °C in perpendicular and longitudinal directions.

film after deposition at 440 °C has an amorphous or similar structure and possesses a relatively high in-plane coercivity which indicates that the amorphous-like $SmCo_5$ shows in-plane anisotropy. High perpendicular anisotropy appears after deposition at 500°C, when the crystalline $SmCo_5$ phase with (0001) texture can be found in the XRD examination (Fig. 5.13). The M-H loops corresponding to the $SmCo_5$ film deposited at 500 ºC are shown in Fig. 5.14b. The coercivity is around 12.7 kOe in the direction perpendicular to the film plane. The initial curve of the sample indicates a pinning-type reversal mechanism. In addition, Fig. 5.15 shows the bright field and dark field cross-section TEM image of the $SmCo_5$ film deposited at 500 °C where it can be seen that the $SmCo_5$ layer has a nanocrystalline structure.

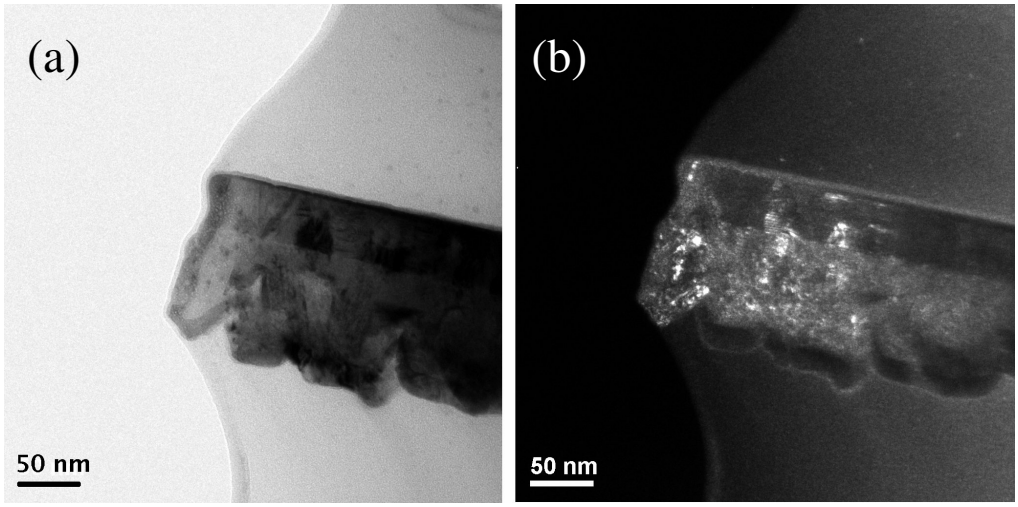

Fig. 5.15 (a) TEM bright field image and (b) dark field image of a cross sectional sample of W 4 nm / Ni_4W 40 nm / $SmCo_5$ 65 nm (500 °C) / W 20 nm (500 °C) thin films.

As shown in Fig. 5.14a, the coercivity of the sample after deposition at 550 °C decreases significantly. The low coercivity is certainly consistent with the poor crystallinity found in the XRD examination, as shown in Fig. 5.13. The poor

crystallinity could be associated with a diffusion of W from the cover layer occurring at high temperature.

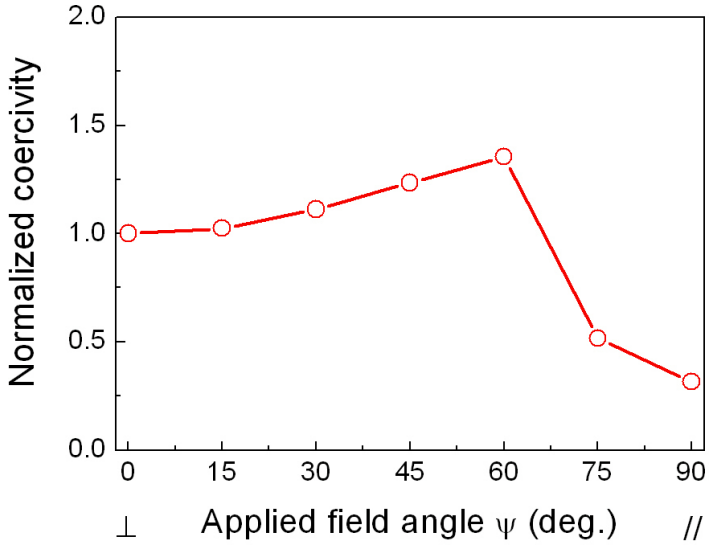

Fig. 5.16. Angular dependence of the normalized coercivity of the $SmCo_5$ film grown on Ni_4W / W underlayer. Zero field refers to out-of-plane direction.

Fig. 5.16 shows the angular dependence of the normalized coercivity of the $SmCo_5$ sample deposited at 500 °C. The curve trend follows the Kondorsky model ($1/\cos\psi$), indicating a domain motion coercivity mechanism. Similar results were reported in Ref. 5 and 6.

5.3.2.2 Effect of thickness of Ni_4W underlayer

From the above discussion, the optimal deposition temperature for the $SmCo_5$ layer is around 500-530 ^oC (Fig. 5.13). Therefore, I have studied the effects of the thickness of the Ni_4W underlayer, the thickness of the $SmCo_5$ magnetic layer and the Sm/Co composition, when all the Sm-Co films were deposited at 500 ^oC. Fig. 5.177 shows the dependence of the out-of-plane coercivity on the thickness of Ni_4W underlayer for a film structure of W (20 nm)/ Sm-Co (65 nm) / Ni_4W (0-80 nm) / W (4 nm). The $SmCo_5$ film exhibits high out-of-plane coercivities around 12 kOe when

grown on a Ni_4W underlayer with a thickness of not less than 13 nm. But without the Ni_4W underlayer, the $SmCo_5$ film only shows a very small coercivity of 0.7 kOe. This indicates that a Ni_4W underlayer is essential for obtaining $SmCo_5$ thin films with high perpendicular coercivity and perpendicular anisotropy. The thickness of the Ni_4W underlayer does not influence the coercivity significantly when it reaches 13 nm and above. Compared with my previous results [7, 8], it is therefore possible to generate a coercivity in $SmCo_5$ as high as when using a 50 nm Cu underlayer with a much thinner 13 nm Ni_4W underlayer. The thinner Ni_4W underlayer is more favorable for practical applications because it reduces the magnetic spacing loss between the soft magnetic underlayer of a double-layered medium and the writing head.

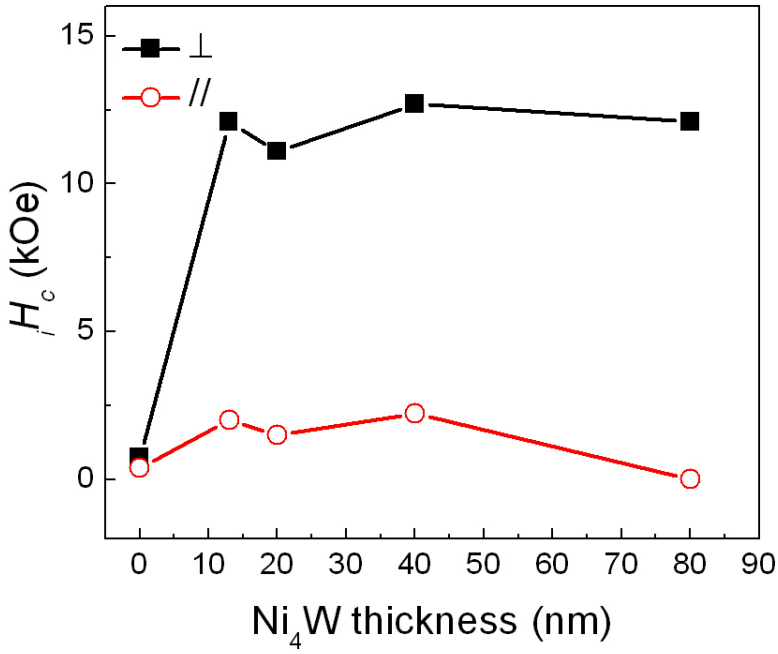

Fig. 5.17. Dependence of the out-of-plane coercivity on the thickness of Ni_4W underlayer for a film structure of W (20 nm) / Sm-Co (65 nm) / Ni_4W (0-80 nm) / W (4 nm).

5.3.2.3 Effect of thickness and composition of $SmCo_5$ layer

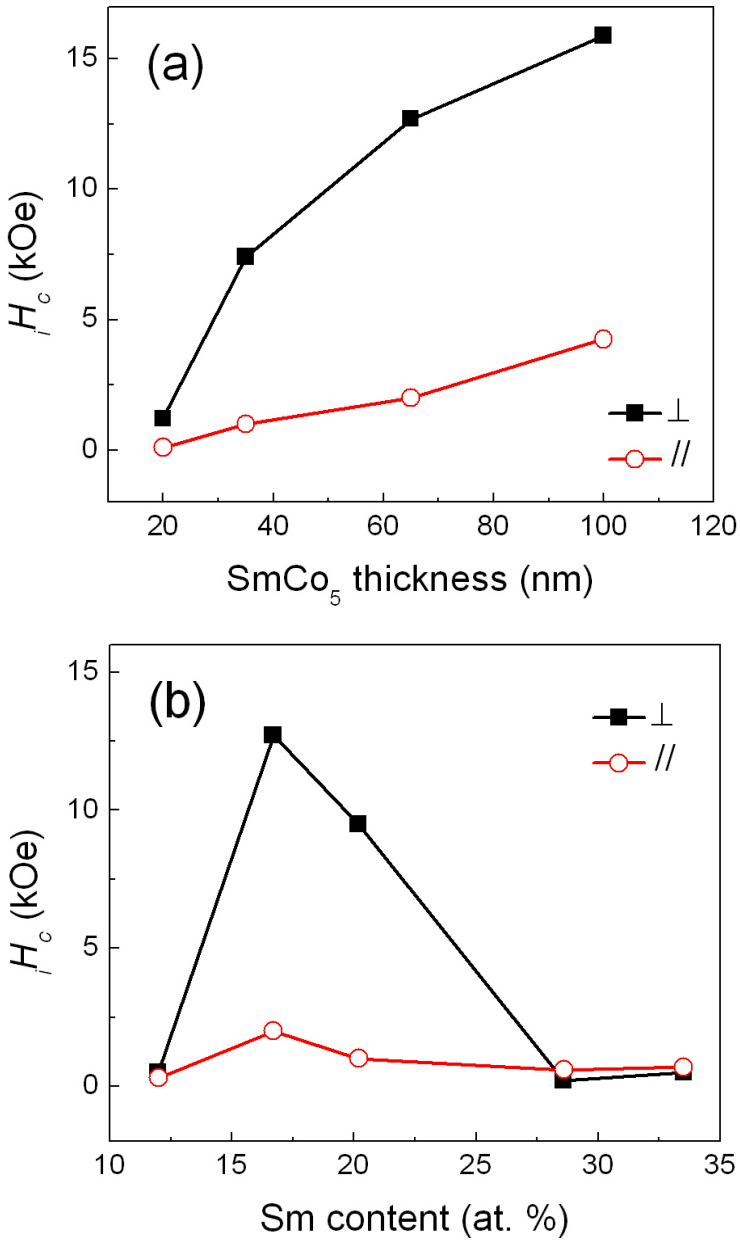

Fig. 5.18. (a) Dependence of the out-of-plane and in-plane coercivity on the thickness of $SmCo_5$ magnetic layer for a film structure of W (20 nm)/ Sm-Co (20-100 nm)/Ni_4W (40 nm)/W (4 nm). (b) Dependence of the out-of-plane and in-plane coercivity on the Sm content for a film structure of W (20 nm)/ Sm-Co (65 nm)/Ni_4W (40 nm)/W (4 nm).

The coercivity of the $SmCo_5$ magnetic layer is found to be dependent on its thickness. From Fig. 5.188a, the coercivity increases continuously with the increase

of the thickness of $SmCo_5$. This is due to the improved crystallinity of the $SmCo_5$ phase in a thicker $SmCo_5$ film. Similar results have been discussed in chapter 3 and chapter 4. In addition, the Sm/Co composition influence the coercivity of Sm-Co thin films significantly. As shown in Fig. 5.188b, the highest out-of-plane coercivity is achieved in the Sm-Co film with the 1/5 atomic ratio of Sm/Co. A deviation of Sm/Co composition from the 1/5 ratio leads to a significant decrease in out-of-plane coercivity.

5.3.3 Deposition of $SmCo_5$ film on Ni / Ni_4W underlayer

As shown in Fig. 5.11, no crystalline $SmCo_5$ can be formed on a pure Ni underlayer with a relatively poor texture and a relatively large roughness. In order to understand if highly textured $SmCo_5$-(0001) can be formed on a well textured Ni-(111) underlayer, 20 nm of Ni was deposited on a Ni_4W underlayer, as shown in Fig. 5.19b. The XRD study shows that well crystallined and highly textured Ni-(111) can be formed after the deposition on highly textured Ni_4W-(211). The rocking curve (shown in the insert in Fig. 5.19a) shows a $\Delta\theta$ value of 2.77°. The subsequently deposited $SmCo_5$ shows clear (0001) and (0002) peaks (Fig. 5.19a), confirming its (0001)-texture. The M-H loops are shown in Fig. 5.19c. An out-of-plane coercivity of 11.5 kOe with a large perpendicular anisotropy is shown in the M-H loops, as the in-plane M-H loop has a very small coercivity. The step at zero field in the out-of-plane M-H loop is attributed to the soft-magnetic Ni phase. This layer structure could be developed to a double-layered perpendicular recording medium where Ni acts as the soft magnetic underlayer (SUL) below the $SmCo_5$ thin film that acts as the magnetic recording layer.

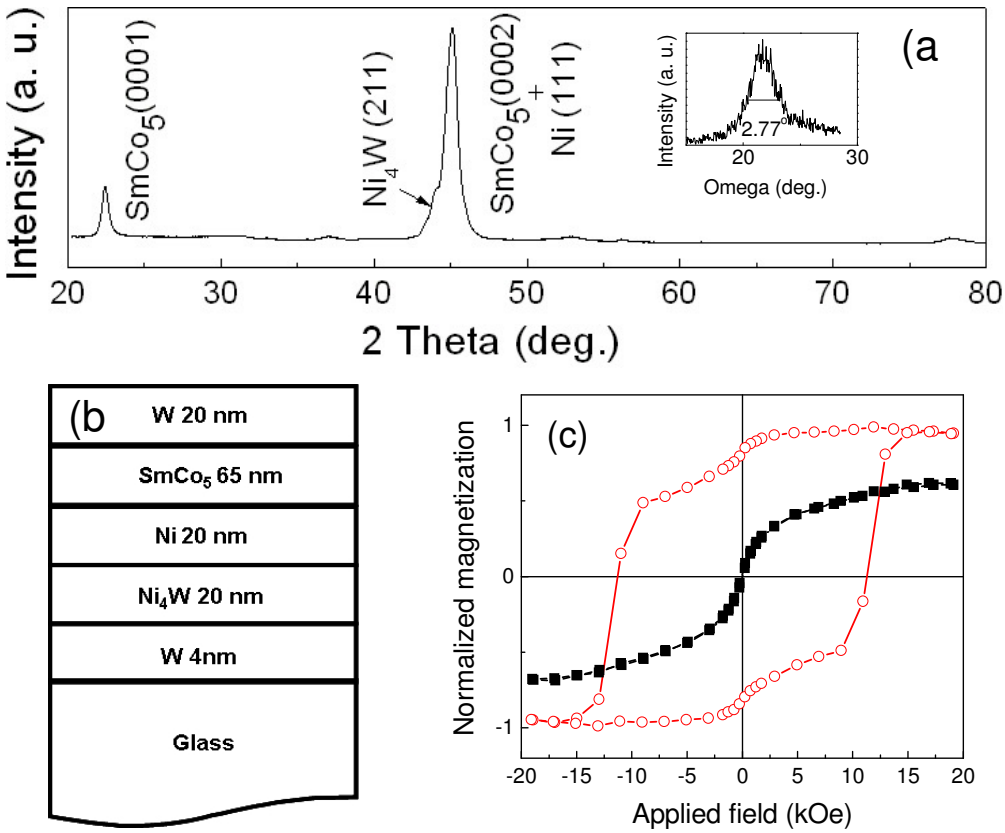

Fig. 5.19. (a) XRD spectrum, (b) illustration of layer structure and (c) M-H loops of 65 nm $SmCo_5$ films grown at 530 °C on Ni (20 nm) / Ni_4W (20 nm) / W (4 nm) layers on glass substrate.

5.4 Summary

In summary, a nanocrystallined and (211)-textured Ni_4W underlayer was successfully deposited on a 4 nm W seed layer at room temperature. The Ni_4W-(211) plane has a hexagonal structure which is similar to that of the $SmCo_5$-(0001) plane. The deposition of the $SmCo_5$ layers on the (211)-Ni_4W underlayer led to a strong (0001) texture with a nano-grained structure after deposition at a temperature in the range of 500-540°C. High coercivity over 10 kOe with a large perpendicular

anisotropy has been achieved on a Ni_4W underlayer on glass substrate, if the thickness of the Ni_4W underlayer is 13 nm or thicker.

Moreover, $SmCo_5$ thin films grown on $Ni_{100-x}W_x$ (x = 0 ~ 100)/W underlayers were studied. (0001) textured $SmCo_5$ thin films were successfully prepared on $Ni_{68}W_{32}$ underlayer with Ni_4W clusters. The maximum out-of-plane ${}_iH_c$ of 15.5 kOe was achieved in $SmCo_5$ thin films grown on $Ni_{68}W_{32}$ underlayer. Highly textured Ni-(111) underlayer can be obtained on highly textured (211)-Ni_4W. The results obtained have shown that the film structure of $SmCo_5$ / Ni / Ni_4W / W is a promising candidate for hard / soft double-layered film for perpendicular recording.

5.5 References

[1]. J. Sayama, K. Mizutani, T. Asahi and T. Osaka, Appl. Phys. Lett. **85**, 5640 (2004).

[2]. I. Kato, S. Takei, X. X. Liu and A. Morisako, IEEE Trans. Magn. **42**, 2366 (2006).

[3]. J. S. Chen, L. N. Zhang, J. F. Hu and J. Ding, J. Appl. Phys. **104,** 093905 (2009).

[4]. L. N. Zhang, J. F. Hu, J. S. Chen and J. Ding, J. Appl. Phys. **105,** 07A743 (2009).

[5]. M. Seifert, V. Neu and L. Schultz, Appl. Phys. Lett. **94**, 022501 (2009).

[6]. "Binary alloy phase diagrams", edited by T. B. Massalski, H. Okamoto, P. R. Subramanian and L. Kacprzak, Materials Park, Ohio, 2nd edition, (1990).

[7]. H. Sakamoto, Y. Nagasu, Y. Ohashi, R. Nakasaki, M. Mimura and A. Nakai, Physica C **463–465**, 600 (2007).

[8]. D. Harker, J. Chem. Phys. **12**, 315 (1944).

[9]. P. A. Beck, Acta Cryst. **B24**, 1477 (1968).

[10]. R. Cury, J.-M. Joubert, S. Tusseau-Nenez, E. Leroy and A. Allavena-Valette, Intermetallics **17**, 174 (2009).

[11]. T. Nasu, M. Sakurai, T. Kamiyama, T. Usuki, O. Uemura and T. Yamasaki, J. Non-Cryst. Solids **312–314,** 319 (2002).

6 Chapter VI Conclusion and future work

6.1 Conclusion

In this thesis, I prepared $SmCo_5$ thin films with the desired magnetic properties using multilayer technology and magnetron sputtering deposition. Both longitudinal anisotropy and perpendicular anisotropy were obtained by choosing suitable underlayers to induce the desired structure. The crystallographic structure, microstructure and magnetic properties of the films were investigated. The results obtained are summarized as the following:

1. $SmCo_5$ thin films have been successfully fabricated with a large longitudinal anisotropy and coercivity up to 26.5 kOe on glass substrates with a Cr underlayer. The satisfactory properties of $SmCo_5$ films can be attributed to the specific texture and smooth surface of the Cr underlayer: when $SmCo_5$ was deposited at 400 °C, a $(11\bar{2}0)$ texture can be induced if the Cr underlayer had a (200) texture and a smooth surface. It was found that a high-quality Cr underlayer can be obtained after deposition at 400 °C. A lower deposition temperature favored the formation of a disordered Cr film or a Cr film with a (110) texture, while a higher deposition temperature caused rough film surface. The Cr underlayer needed a minimum thickness of 50-60 nm in order to have a good crystallinity. High intrinsic coercivity required a minimum thickness of the $SmCo_5$ layer in the order of 50 nm, as a thinner film possessed a poor crystallinity. The resultant films exhibited large in-plane magnetic anisotropy and high in-plane coercivity with a nanocrystalline structure. Under these optimal conditions, a $SmCo_5$ film was deposited on an MgO substrate as well. The crystallographic structure, microstructure and magnetic properties of the $SmCo_5$ thin films with a Cr underlayer grown on MgO (100) and glass substrates were found to be different.

The epitaxial relationship: $SmCo_5$ $(11\bar{2}0)$ <0001> // Cr (200) <110> // MgO (200) <001> was demonstrated between $SmCo_5$, Cr and MgO. This $SmCo_5$ film exhibited in-plane anisotropy, in-the-plane anisotropy and remanence enhancement. On the other hand, polycrystalline $SmCo_5$ film with a preferred $(11\bar{2}0)$ orientation was grown on a Cr underlayer with a (200) texture on an amorphous glass substrate. This $SmCo_5$ film showed even larger in-plane anisotropy and remanence enhancement due to the nanocrystalline structure and strong interaction between grains.

2. Highly (111) textured Cu underlayers were fabricated on glass substrates by introducing Ta seed layers. Highly (000l) textured $SmCo_5$ thin films exhibiting large perpendicular anisotropy and high out-of-plane coercivity were obtained on the Cu / Ta dual underlayers. A Ta seed layer was effective in improving the crystallinity, texture and surface morphology of the Cu underlayer. The improvement strongly depended on the thickness of the Ta seed layer. The optimal Ta seed layer was a thin, continuous and amorphous-like layer with a thickness of 4 nm. The crystallinity, texture, and surface morphology of the Cu underlayer significantly influenced the crystallinity, texture and magnetic properties of the $SmCo_5$ layer. Under the optimal conditions, when the $SmCo_5$ was deposited at 400 ^oC on a Cu (50 nm) / Ta (4 nm) dual underlayer, the $SmCo_5$ magnetic layer possessed a good (000l) texture, a small $\Delta\theta_{50}$ value (3.2^o) and a large out-of-plane coercivity around 20 kOe. When the Ta seed layer was present, well crystallized $SmCo_5$ films with (0001) texture can be obtained at a deposition temperature that is as low as 325 ^oC. Moreover, Cu from the Cu underlayer diffused into the $SmCo_5$ layer which resulted in the improved crystallinity of the film by forming

$Sm(Co,Cu)_5$ phase but rather large grain size of around 50 nm.

3. For the first time, a nanocrystallined and (211)-textured Ni_4W / W dual underlayer was found to be able to induce $SmCo_5$ thin films with perpendicular anisotropy. This is due to the Ni_4W-(211) plane having a hexagonal structure which is similar to that of the $SmCo_5$-(0001) plane. The deposition of the $SmCo_5$ layers on the (211)-Ni_4W / W underlayer led to a strong (0001) texture with a nano-grained structure after deposition at a temperature in the range of 500-540°C. High coercivity over 10 kOe with a large perpendicular anisotropy has been achieved on a Ni_4W underlayer on glass substrate if the thickness of the Ni_4W underlayer is 13 nm or thicker. Moreover, $SmCo_5$ thin films were also prepared on a $Ni_{68}W_{32}$ underlayer with Ni_4W clusters. A maximum out-of-plane ${}_iH_c$ of 15.5 kOe was achieved in $SmCo_5$ thin films grown on $Ni_{68}W_{32}$ underlayer. Highly textured Ni-(111) underlayers can be obtained on highly textured (211)-Ni_4W. The results have shown that the film structure of $SmCo_5$ / Ni / Ni_4W / W is a promising candidate for hard/soft double-layered film for perpendicular recording.

6.2 Future work

In the competitive race towards ever higher magnetic recording densities, $SmCo_5$ is a very promising candidate as shown by the high coercivity and the large anisotropy of the films produced using the methods presented in this thesis. In this respect, the work completed here represents a great step forward towards the applicability of the $SmCo_5$ thin film technology in real-life applications such as magnetic data storage and micro-electronic-mechanical systems (MEMS).

However, many practical problems need to be solved and many technical optimizations need to be completed for $SmCo_5$ thin films to be readily usable in

actual hard disk drives.

First, a major concern is the relatively poor corrosion resistance of $SmCo_5$. Good corrosion resistance is an important factor for practical use as a recording medium. Therefore, strategies to improve the corrosion resistance such as the use of additive elements in the $SmCo_5$ layer or the use of a protective cover layer should be quantitatively investigated.

Second, further experimental work should be done on reducing the thickness and the grain size of the $SmCo_5$ layer. This can be achieved by adding non-magnetic materials such as C in the $SmCo_5$ layer and by controlling the microstructure of the underlayer. Besides, non-magnetic additives in $SmCo_5$ can also decrease the exchange coupling between grains in order to increase the signal-to-noise ratio.

Third, for perpendicular recording, a soft magnetic underlayer (SUL) is needed to increase the writing ability and the read back signal amplitude. The SUL should have a specific texture in order to induce the desired texture in the recording layer. My preliminary results show that $SmCo_5$ / Ni / Ni_4W / W is a promising layer configuration for a hard/soft double-layered film. However, the microstructure of the Ni layer (acting as a SUL) should be further adjusted so that there is no distinct domain wall in the film. This is necessary in order to avoid “spike noise”. Moreover, an appropriate intermediate layer between the SUL and the recording layer needs to be discovered. The intermediate layer should be able to de-couple these two layers and to control the texture and microstructure of the recording layer. In addition, this intermediate layer should be thin enough to avoid spacing loss and should be immiscible with the SUL and the recording layer.

Last, the read-write characteristics for $SmCo_5$ / Ni / Ni_4W thin films as perpendicular recording media should be practically evaluated.

I also believe that $SmCo_5$ films with satisfactory structures and properties such as the one fabricated in this thesis can be applied not only to conventional recording but also to advanced recording technologies such as pattern recording and heat assisted recording.

In addition, $SmCo_5$ with a high coercivity and a large perpendicular anisotropy may be also interested for other applications, such as MEMS and as a magnetic layer in spintronics devices. The future work includes the exploration of $SmCo_5$ thin films for other hard magnetic applications.